

**ANALYSIS AND DESIGN OF PASSIVE UNDERWATER ACOUSTIC  
IDENTIFICATION TAGS**

A Dissertation  
Presented to  
The Academic Faculty

By

Aprameya Satish

In Partial Fulfillment  
of the Requirements for the Degree  
Doctor of Philosophy in the  
School of Mechanical Engineering

Georgia Institute of Technology

December 2020

© Aprameya Satish 2020

# **ANALYSIS AND DESIGN OF PASSIVE UNDERWATER ACOUSTIC IDENTIFICATION TAGS**

Thesis committee:

Dr. Karim Sabra  
School of Mechanical Engineering  
*Georgia Institute of Technology*

Dr. Chengzhi Shi  
School of Mechanical Engineering  
*Georgia Institute of Technology*

Dr. Alper Erturk  
School of Mechanical Engineering  
*Georgia Institute of Technology*

David Trivett  
School of Mechanical Engineering  
*Georgia Institute of Technology*

Dr. Julien Meaud  
School of Mechanical Engineering  
*Georgia Institute of Technology*

Dr. Alessio Medda  
Aerospace, Transportation and Advanced  
Systems  
*Georgia Tech Research Institute*

Date approved: October 21, 2020

For Savanthi

## ACKNOWLEDGMENTS

I would like to first extend my gratitude to my advisor Dr. Karim Sabra, for his time, mentorship, and for being a constant source of inspiration, and motivation over the course of my PhD. Our discussions relating to both my research, and life in general will certainly accompany me in all my future endeavors. I am also grateful to Dr. Sabra and the ONR for supporting this research financially, and making this PhD possible.

I would also like to thank the members of my reading committee, Dr. Alper Erturk, Dr. Julien Meaud, Dr. Chengzhi Shi, David Trivett, and Dr. Alessio Medda for providing valuable feedback and insightful discussions during various stages of my research. I have also found over the course of the PhD that conducting underwater experiments has an added layer of complexity, which I could not have navigated without the guidance of Jim Martin and Dr. Francois Guillot.

I have had the privilege of working alongside some fantastic peers as we collectively moved through graduate school. Being able to discuss interesting research questions, and share our successes and challenges made this a memorable experience. It was also a pleasure mentoring and learning from the exceptional undergraduate research students who assisted me in this research.

There aren't words to express the support and encouragement I received from my grandmother, parents, sister, aunts, uncles, cousins, and friends. This endeavour truly takes a village.

Lastly, I would like to thank my wonderful wife Savanthi, who stood by me the entire way, and remained patient through all the weekends and late nights I spent working, especially during the final stages of this research. We discovered the joy of solving jigsaw puzzles during breaks from work, which I think is a tradition in the making.



## TABLE OF CONTENTS

<b>Acknowledgments</b> . . . . .	iv
<b>List of Tables</b> . . . . .	ix
<b>List of Figures</b> . . . . .	x
<b>List of Acronyms</b> . . . . .	xv
<b>Summary</b> . . . . .	xvii
<b>Chapter 1: Introduction</b> . . . . .	1
1.1 SAW RFID Tags and the AID tag analog . . . . .	5
1.2 Advantages of the proposed AID tag design . . . . .	8
1.3 Contributions to the Literature . . . . .	10
1.4 Thesis overview . . . . .	12
<b>Chapter 2: Passive AID tags with horizontal stratification</b> . . . . .	13
2.1 Introduction . . . . .	13
2.2 Analytic simulation of horizontally stratified AID tags . . . . .	13
2.2.1 Global Matrix formulation . . . . .	14
2.2.2 Modelling Material Damping . . . . .	22
2.2.3 Global matrix method validation . . . . .	25

2.3	Modelling a library of unique acoustic signatures . . . . .	30
2.4	Experimental testing of horizontally stratified AID tags . . . . .	34
2.4.1	Sub-scale experimental setup . . . . .	34
2.4.2	Material selection . . . . .	36
2.4.3	Material calibration . . . . .	38
2.4.4	Horizontally stratified AID tag fabrication . . . . .	41
2.4.5	AID tag response measurements . . . . .	42
2.5	Chapter Summary . . . . .	45
<b>Chapter 3: Passive AID tags with omnidirectional backscatter . . . . .</b>		<b>46</b>
3.1	Introduction . . . . .	46
3.2	Scattering from an elastic spherical shell . . . . .	47
3.2.1	Analytical model . . . . .	49
3.3	Modelling high frequency scattering from spherically layered AID tags . . .	54
3.3.1	Setting up the AID tag simulation environment in k-Wave . . . . .	55
3.3.2	k-Wave simulation results and the flat plate approximation . . . . .	60
3.4	Experimental testing of hemispherically stratified AID Tags . . . . .	66
3.4.1	Experiment Setup and shell fabrication . . . . .	66
3.4.2	Hemispherical AID tag response measurements . . . . .	69
3.5	Chapter Summary . . . . .	74
<b>Chapter 4: Tag Design Optimization . . . . .</b>		<b>75</b>
4.1	Tag Design Criteria . . . . .	75
4.2	Energy based layering strategy . . . . .	75

4.3	Optimal elastic layer thickness . . . . .	80
4.4	Effect of source bandwidth on AID tag detectability . . . . .	83
4.5	Chapter Summary . . . . .	88
<b>Chapter 5: AID tag detection . . . . .</b>		<b>90</b>
5.1	Match-filtering performance of AID tags . . . . .	90
5.2	Tag detection near an interferer . . . . .	91
5.3	Template correlations . . . . .	99
5.4	A case study of two AID tags in proximity to each other . . . . .	101
5.5	Simulation of an AID tag near a hard shale sediment . . . . .	106
5.6	AID tag detection range . . . . .	111
5.6.1	Receiver based parameters . . . . .	112
5.6.2	AID tag based parameters . . . . .	112
5.7	Chapter Summary . . . . .	114
<b>Chapter 6: AID tag experiments in the SONAR regime . . . . .</b>		<b>115</b>
6.1	Calibration of the Starfish 452F SONAR . . . . .	116
6.2	Tag Fabrication . . . . .	120
6.3	AID tag response measurements . . . . .	122
6.4	Cross trial performance of AID tag templates and observations . . . . .	128
6.5	Chapter Summary . . . . .	132
<b>Chapter 7: Future work and conclusions . . . . .</b>		<b>133</b>
7.1	Summary . . . . .	133

7.2 Contributions to the Literature . . . . .	134
7.3 Future Work . . . . .	135
<b>Appendices . . . . .</b>	<b>137</b>
Appendix A: Analytical formulation for the scattered acoustic field from a spherical shell . . . . .	138
Appendix B: Table of material properties . . . . .	148
<b>References . . . . .</b>	<b>150</b>

## LIST OF TABLES

3.1	Layer thicknesses for the four water-layer AID tag used in k-Wave and global matrix simulations. Here, layer 1 represents the top water halfspace, and layer 11 represents the bottom halfspace. . . . .	57
5.1	Match filtered results obtained using a 1-1-0 AID tag template thresholded to a 20% saturation level to detect a 1-1-0 AID tag in proximity of a 0-1-0 tag under varying conditions of signal overlap and noise. . . . .	102
5.2	Simulation parameters used to compute the range at which a four water-layer AID tag can be detected. . . . .	114
6.1	SIR gains for an experimentally collected two-layer AID tag template iterated through thresholding values and the use of the flange reflection. The OSIR of the data before match filtering is -11.77 dB (see Figure 6.10a) . . .	130
B.1	Acoustic properties of common fluids, plastics, and metals . . . . .	149

## LIST OF FIGURES

1.1	Examples of AUV missions requiring high spatial precision . . . . .	1
1.2	Examples of AUV localization using active acoustic transponders . . . . .	2
1.3	Schematic of AUV trajectory and measurements for target localization using monostatic sensing . . . . .	4
1.4	Schematic of an AUV equipped with rotary SONAR detecting deployed AID tags . . . . .	5
1.5	Schematic of SAW RFID tags in operation, and its acoustic barcode analog	6
1.6	An example of an AID tag signature that may be generated using alternating acrylic and water layers. The full simulation details for simulating this signature are provided in section 3.3 and Table 3.1. . . . .	7
1.7	Optical navigation markers used by AUVs . . . . .	9
1.8	Example of positioning error accumulation from sensor drift. . . . .	10
2.1	Schematic of an Acoustic IDentification (AID) tag . . . . .	14
2.2	Notation used for coordinate system, layers, interfaces, and propagating waves in the Global Matrix formulation [37] . . . . .	15
2.3	Schematic of the simulation of an AID tag response for a specified input $x(t)$	22
2.4	Verification of the Global matrix method solution using standard reflection coefficient for aluminum plate. Left panel indicates the full spatio-temporal evolution of an incident Gaussian pulse on the aluminum plate from a top water layer. . . . .	28

2.5	Verification of the Global matrix method solution using standard reflection coefficient for acrylic plate. Left panel indicates the full spatio-temporal evolution of an incident Gaussian pulse on the acrylic plate from a top water layer. . . . .	29
2.6	Simulation of the temporal signature of an AID tag . . . . .	30
2.7	Example of AID tag signature libraries generated using permutations of three and four acoustically different materials. . . . .	31
2.8	(a) Signature obtained from a HDPE-acrylic-PVC-polycarbonate tag (b) Signature obtained from a HDPE-PVC-acrylic-polycarbonate (c) Output cross-correlation of the signatures (a) and (b). (d) Correlation map for an AID tag designed with three layers as in Figure 2.7a. (e) Correlation map for an AID tag designed with four layers as in Figure 2.7b. . . . .	33
2.9	Ultrasonic probe spectrum and transmit pulse shape. . . . .	35
2.10	Experimental setup of ultrasonic probe. . . . .	36
2.11	Material impedances in Mrayl for different viscoelastic materials and common metals. . . . .	37
2.12	Material characterization from backwall scattering experiments for different viscoelastic materials. . . . .	40
2.13	Fabricated two and four layer, horizontally stratified AID tags. . . . .	42
2.14	Comparison of experimentally obtained acoustic responses for two and four layer AID tags with their corresponding simulated signatures. . . . .	44
3.1	Schematics demonstrating the limitation of the horizontally stratified AID tag and the omnidirectional response of spherically stratified AID tags. . . .	47
3.2	Schematic to demonstrate the physics of scattering from layered spherical shells . . . . .	48
3.3	Backscatter from an air filled steel shell for $ka \sim 50$ . . . . .	53
3.4	Backscatter from an air filled steel shell for $ka \sim 2000$ . . . . .	54
3.5	(a) Wideband 500 kHz Gaussian pulse used as source signal for k-Wave simulation. (b) Magnitude spectrum of (a) . . . . .	56

3.6	Density maps used in k-Wave simulations of spherically and hemispherically stratified AID tags. . . . .	58
3.7	Time-histories recorded along the sensor lines for the spherically and hemispherically stratified AID tag simulations using k-Wave. . . . .	61
3.8	Time-histories recorded at the 100th, 200th and 300th sensors of the spherically and hemispherically stratified AID tag simulations using k-Wave. . . . .	62
3.9	The backscattered response from a flat-plate AID tag simulated using the Global Matrix Method, using the same layer materials and thicknesses as in the spherical or hemispherical AID tag k-Wave simulation. . . . .	63
3.10	k-Wave obtained scattered field responses compared to equivalent global matrix solution for (a) Spherically stratified AID tag (b) Hemispherically stratified AID tag with source incident from $\theta = 0^\circ$ (c) Hemispherically stratified AID tag with source at $\theta \neq 0$ . . . . .	65
3.11	Process of additively manufacturing hemispherical AID tags using stereolithography. . . . .	67
3.12	(a) Sideview of the "Tough" hemispherical shell placed near the ultrasound probe. (b) Top view of the same setup. The spacing between each grid point is 1in. . . . .	68
3.13	(a) Acoustic property estimation from the backwall scattering from the Clear resin shell (b) Acoustic property estimation from the backwall scattering from the Tough resin shell . . . . .	69
3.14	(a) Schematic of the experimental set-up, testing the assembled two-shell AID tag. Shell I is printed out of Clear resin, while shell II is printed out of Tough resin. The inter-shell space is filled with water acting as an acoustic couplant. The entire setup is immersed in a water bath. The convention for measured azimuthal angle is also marked. (b) Close up of the AID tag being tested. . . . .	70
3.15	The full scattered response from the two-shell hemispherical AID tag tested using the ultrasound setup. The first red box indicates the specular component of the scattered field, while the second red box demarcates the late structural arrivals from possible guided waves and the aluminum backing plate. . . . .	71
3.16	Backscattered responses collected over varying azimuthal incidence angles from $\theta = 0^\circ$ to $\theta = 70^\circ$ as marked. . . . .	72



3.17	Comparison of the simulated and experimental waveforms for the additively manufactured two-shell hemispherical AID tag. . . . .	73
4.1	Spatio-temporal scattering histories computed using the Global Matrix method for a 2 mm aluminium and acrylic plate immersed in water . . . . .	77
4.2	Spatio-temporal scattering histories for an AID tag with alternating acrylic-water layers, and an AID tag with alternating acrylic-PVC layers. The layer energy densities for both these tags is also shown. . . . .	79
4.3	Optimal shell thickness specification based on the impedance translation theorem. . . . .	81
4.4	AID tag signatures simulated for varying source fractional bandwidths. . . .	85
4.5	Reflected energy for AID tags with varying fluid layers, with and without a rigid backing plate. . . . .	89
5.1	Detection of a simulated 4-layer tag signature when in the presence of a strong interfering signal. . . . .	93
5.2	MFSIRs of tags near a strong interferer as a function of the number of fluid layer, and template saturation. . . . .	96
5.3	MFSIRs for AID tags with different numbers of fluid layers, and template saturation, computed for varying source bandwidths. . . . .	98
5.4	Correlation maps for AID tag signatures generated by including or removing the intermediate acrylic layers in a four water-layer tag. . . . .	100
5.5	Detection of a 1-1-0 AID tag that is in the proximity of a 0-1-0 tag such that both signatures are well separated. . . . .	103
5.6	Detection of a 1-1-0 AID tag that is in the proximity of a 0-1-0 tag such that both signatures overlap. . . . .	104
5.7	Detection of a 1-1-0 AID tag that is in the proximity of a 0-1-0 tag such that both signatures overlap, and are embedded in additive white noise. . . .	105
5.8	k-Wave simulation of a four water-layer AID tag near a rough shale sediment.	107
5.9	Time histories recorded at the virtual sensor locations of the k-Wave simulation of the four water-layer AID tag near a rough shale sediment. . . . .	108

5.10	Comparison of the monostatic response of the k-Wave scattered field of an AID tag near a rough interface to an AID tag template computed using the Global Matrix method. . . . .	110
6.1	The data collection pipeline used during experimentation. . . . .	116
6.2	Backwall scattering spectrogram obtained using the Starfish 452F SONAR in the acoustic water tank facility. . . . .	118
6.3	Extraction of the SONAR Tx signal from backwall scattering measurements.	119
6.4	AID tag design specifications for SONAR. . . . .	121
6.5	Schematic of experimental setup. The tag is placed in the within the beamwidth (shaded area in top view) of the SONAR. Two types of signals (marked by 1, and 2 in figure) are reflected by the tag and correspond to the layer signature of the tag and the diffracted rays from the flange, respectively. . . .	123
6.6	Raw data received by the SONAR, prior to match filtering, for the two water layer tag shown in Figure 6.4. . . . .	124
6.7	Detection of an AID tag by match-filtering pulse compressed SONAR data with an AID tag template extracted from the same measurement. . . . .	126
6.8	The AID tag signature structure of the two water layer tag, where the returns from the shell layers and backing plate comprising the tag are marked.	127
6.9	a)AID tag consisting of a single 13in Diameter shell b) AID tag consisting of a 13in and 8in Diameter shell c) AID tag consisting of a 13in and 10in Diameter shell d) AID tag consisting of a 13in, 10in and 8in Diameter shell.	128
6.10	Cross-experimental AID tag detection performance. . . . .	131

## LIST OF ACRONYMS

<b>AID</b>	Acoustic IDentification
<b>AUV</b>	Autonomous Underwater Vehicle
<b>BSX</b>	backscattering cross-section
<b>CAD</b>	Computer Aided Design
<b>CFL</b>	Courant-Friedrichs-Lewy
<b>GMM</b>	Global Matrix Method
<b>HDPE</b>	High Density Polyethylene
<b>IDT</b>	Interdigital Transducer
<b>IMU</b>	Inertial Measurement Unit
<b>LFM</b>	Linear Frequency Modulated
<b>MF</b>	Match Filtering
<b>MFE</b>	Mid-Frequency Enhancement
<b>MFSIR</b>	Match Filtered Signal-to-Interference Ratio
<b>OSIR</b>	Original Signal-to-Interference Ratio
<b>PETG</b>	Polyethylene Terephthalate Glycol
<b>PML</b>	Perfectly Matched Layer
<b>PSTD</b>	Pseudo Spectral Time Domain
<b>PVC</b>	Polyvinyl Chloride
<b>RF</b>	Radio Frequency
<b>RFID</b>	Radio Frequency Identification
<b>ROV</b>	Remote Operated Vehicle
<b>SAW</b>	Surface Acoustic Wave

**SIR** Signal-to-Interference Ratio

**SLA** Stereolithography

**SNR** Signal-to-Noise Ratio

**SONAR** SOund NAvigation and Ranging

## SUMMARY

The development of predeployed underwater infrastructures to aid in Autonomous Underwater Vehicle (AUV) navigation is of keen interest, with the increased use of AUVs for undersea operations. This work presents a class of passive underwater acoustic markers, termed Acoustic IDentification (AID) tags, which are inexpensive to construct, simple to deploy, and reflect unique, engineered acoustic signatures that can be detected by an AUV instrumented with high-frequency Sound Navigation and Ranging (SONAR) systems. An AID tag is built of layers of materials with different acoustic properties and thicknesses such that a portion of the acoustic energy from an incident pulse from an AUV, for example, is reflected from each interface between two adjacent layers. In this manner, unique acoustic signatures can be generated, similar to an optical barcode. AID tags can be used therefore as geospatial markers to highlight checkpoints in AUV trajectories, or to mark areas of interest underwater. Numerical simulations of the acoustic signatures of two AID tag design iterations i.e. a horizontally stratified AID tag, and a hemispherically stratified AID tag, were experimentally validated using a sub-scale ultrasound setup. Furthermore, an energy based layer optimization strategy was proposed to maximize the strength of reflected AID tag signatures for different source frequency ranges. Subsequently, the detectability of AID tags in the proximity of strong interference such as a hard seabed or another AID tag was quantified, and the detection range of an AID tag was computed based on the standard SONAR equation. Finally, experimental results of hemispherical AID tags interrogated by high-frequency SONAR were presented to demonstrate AID tag performance in realistic deployment scenarios.

## CHAPTER 1

### INTRODUCTION

The increased use of Autonomous Underwater Vehicles (AUVs) for bathymetry mapping, marine life monitoring, mineral exploration, marine geosciences, mine countermeasures, and a myriad of other applications [1, 2, 3, 4] has created significant interest in the design of effective navigation systems and predeployed underwater infrastructure to facilitate efficient mission planning and execution [5]. Typically during operation, AUVs require precise spatial positioning information to ensure reliable navigation and for operations such as docking (more broadly, homing in on a target), tracking, and hovering near targets.

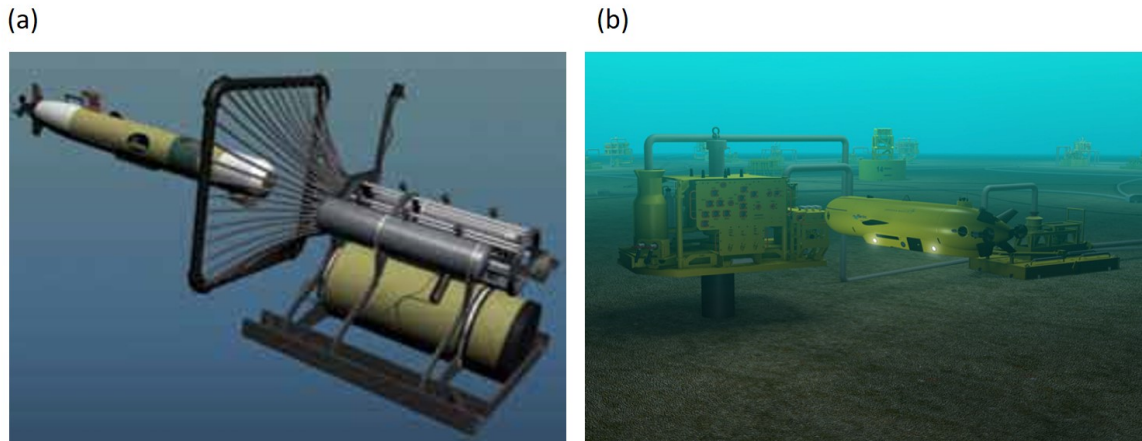


Figure 1.1: (a) Autonomous docking of the REMUS [6] (b) Lockheed Martin's Marlin AUV near an underwater high bandwidth wireless communications node [7].

AUV navigation however remains challenging due to the limited human control available after deployment, and relies purely on the instrumentation onboard, or predeployed in the operating environment. Effective solutions to the AUV navigation problem afford significant gains in underwater mission capabilities by providing improved range, reachability and operation in challenging underwater environments. In comparison, traditional systems such as Remote Operated Vehicles (ROVs) are tethered to a ship for power and communi-

cations [8]. Furthermore, relative to ROVs for example, an AUV requires minimal post-deployment human intervention as its objectives and trajectories can be pre-programmed to its onboard computer. To this end, sensors onboard an AUV, and man-made underwater markers can be used to assist in its autonomy. Cameras, Inertial Measurement Units (IMUs), hydrophones etc. mounted on an AUV can be used to provide bearing information and vision capabilities, while acoustic transponders (or beacons), acoustic reflectors, and fiduciary markers with classifiable optical features can be used as detectable positioning references or to indicate coordinates of interest. Several methods have been proposed to make use of the various instrumentation available on an AUV to assist with navigation. For example, dead-reckoning [9] using IMU feedback is a commonly used navigation technique on AUV missions where the trajectory of an AUV is adjusted based on current velocity (and acceleration) measurements and the previously predicted AUV position. Other techniques use AUV instrumentation in tandem with detectable, pre-deployed, man-made markers or instrumentation (such as geolocated acoustic transponders as in Figure 1.2(a,b)) [10, 11, 5] or optical markers [12, 13] to aid in AUV navigation.

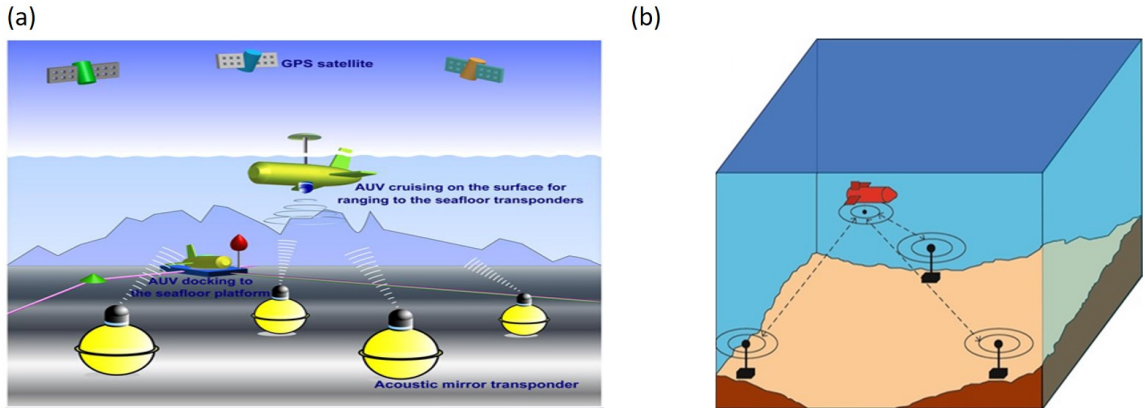


Figure 1.2: (a) AUV localization using a series of acoustic transponders placed on the seabed in tandem with GPS information [10] (b) AUV triangulation using long baseline system [14] using a distributed array of acoustic transponders placed at known spatial locations [5].

While the methods mentioned above are popular, they have certain limitations. For example, IMU based navigation can accumulate significant positioning error from sensor

measurement uncertainties, acoustic transponders are expensive, non-covert and may require complex calibration at setup, and the sensing of optical markers is limited only to short ranges in clear water due to the poor propagation of light in water. It is therefore of interest to develop a navigation system or aid with three key criteria in mind - detectability in varying underwater environments, ease of maintenance and deployment, and uniqueness of detectability. This aid should be able to operate independently or in tandem with an IMU, to assist in AUV navigation and in marking underwater targets.

This dissertation develops the design of one such system, wherein AUVs instrumented with high-frequency ( $>100$  kHz) SOund NAvigation and Ranging (SONAR) can gather positional information or locate marked underwater features by detecting the backscattered acoustic signatures from engineered Acoustic IDentification (AID) tags placed at known locations. The term AID tag refers to the fact that the designed marker can be recognized using acoustic detection methods such as SONAR. In specific, the backscattered acoustic signatures of the AID tags so designed are purely a function of the materials and geometry of the AID tag itself, thereby being a "passive" navigational marker where no additional circuitry or active electronic components are used, as opposed to a transponder for example.

To further motivate the use of such a passive AID tag, two possible applications of an AID tag are presented - the first discussing AID tag localization in the context of target homing, and the second regarding the use of an AID tag as a navigational marker or survey point along a path or marked underwater boundary.

Target localization strategies as in [15, 16] may be used to home in on an AID tag upon detection of its signature, which is useful for docking and hovering near a fixed point of interest as previously mentioned. In brief, it is shown in [15] that an AUV can localize an acoustic target (here, an AID tag) using a least-squares or maximum likelihood estimate of the target position, from measurements of the target from different AUV positions. The target position estimate in this technique is dependent on the measurement noise, and therefore, strong or unique acoustic targets such as an AID tag would assist in more accurate



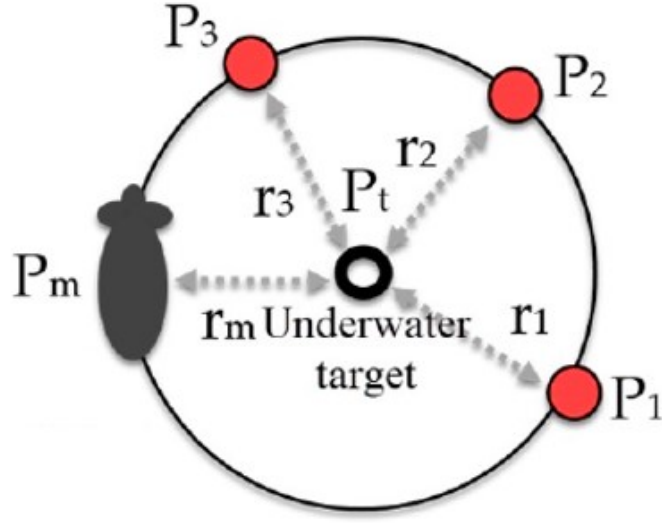


Figure 1.3: Schematic of target localization from an AUV as in [15, 16]. An AUV equipped with sidescan SONAR at position  $P_m$  homes in on an AID tag target a radius of  $r_m$  from the vessel.

homing. Furthermore, the capability of designing unique acoustic signatures for different AID tags can serve as a method of target identification.

The second example of AID tags serving as boundary or path markers is shown in Figure 1.4a. Here, four AID tags with unique acoustic signatures, marked A through D in Figure 1.4a are placed to form a boundary or path in a region of interest. An AUV equipped with a scanning SONAR in the proximity of these tags can sense the unique signatures (marked as signals A through D) and either home in on a specific tag as discussed previously, or use each tag location as a checkpoint to visit in the trajectory of the AUV. For reference, a scanning SONAR may produce an image as shown in Figure 1.4b, where the AUV is situated in the center and the bright regions show reflected signals detected by the imaging SONAR. As a motivating example, if AID tags were placed in the field of view of the AUV as in Figure 1.4a, then the SONAR image shown in Figure 1.4b would contain AID tag signature returns from the marked red locations, that the AUV could detect.

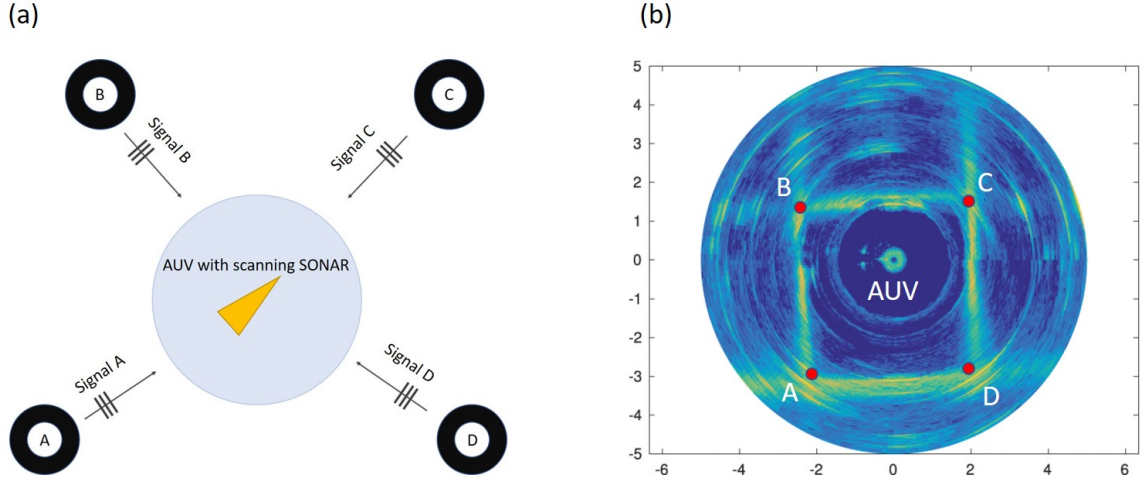


Figure 1.4: a) An AUV equipped with scanning SONAR, flying within the area enclosed by four AID tags, marked A through D. The field of view of the AUV is indicated as the light blue circle around the AUV. Each AID tag has the capability of reflecting a unique signature, marked signals A through D upon interrogation by the scanning SONAR. b) An example image from a scanning SONAR taken from [17]. As a demonstration, the red markers labelled A through D could potentially indicate the returns from four AID tags positioned as shown in (a). The different acoustic signatures can be detected through custom algorithms, and direct an AUV to the individual markers based on the required task.

### 1.1 SAW RFID Tags and the AID tag analog

The design of AID tags in this work takes inspiration from Surface Acoustic Wave (SAW) Radio Frequency Identification (RFID) tags commonly used in communications applications [18]. These SAW RFID tags (see Figure 1.5a) comprise of an electroacoustic transduction antenna and a material substrate whose surface is lined with a series of acoustic reflectors spaced in a manner akin to an optical barcode, where the reflector location corresponds to a binary 1, for example. The antenna is used to receive an encoded input waveform (e.g. pulse or a pulse train) from a Radio Frequency (RF) emitter and converts the electromagnetic signal to an acoustic surface wave which propagates along the substrate. This conversion is achieved through an Interdigital Transducer (IDT), using the piezoelectric effect [19], that generates guided surface acoustic waves from the input signal [18, 20]. The generated surface waves propagate over the substrate, a portion of the energy incident at each reflector reflecting back towards the antenna, and a portion transmitting to the next

reflector. In this manner, the SAW RFID tag generates a surface wave reflected response which is a function of the reflector and substrate properties. It is to be noted that in order to ensure that the surface wave energy reaches the end of the tag, the reflectivity of each reflector is marginally increased, with the final reflector in the sequence having the highest reflectivity. The series of reflected surface waves is reconverted to an RF signal and transmitted from the antenna for detection. Different encoding techniques can be formulated to maximize the uniqueness or orthogonality between various tag signatures [21, 22, 23].

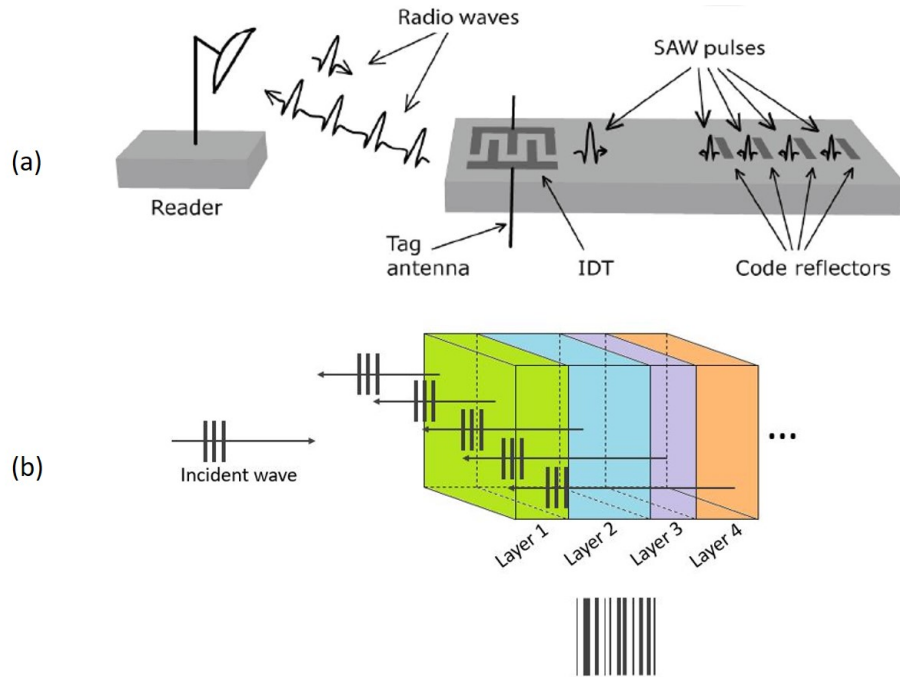


Figure 1.5: (a) Schematic of a SAW RFID tag in operation. The reader transmits a radiowave which is captured by a tag antenna. Surface waves are generated on the material substrate through the piezoelectric effect by means of an IDT, and the signal reflected by the code reflectors are re-transmitted to the reader [18]. (b) Schematic of a stratified AID tag - the acoustic analog to the SAW RFID tag, wherein an incident plane wave is reflected from each interface of the AID tag to make the acoustic signature. The incident wave could be generated by an interrogating SONAR mounted on an AUV platform. Both (a) and (b) are similar to an optical barcode.

An AID tag (see Figure 1.5b) is designed to operate in a similar fashion, except now in the high-frequency SONAR ( $> 100$  kHz) regime - which is hardware commonly found on board the AUV payload (e.g. such as the REMUS [24]). Here, instead of reflectors on

a substrate, plates or shells with varying acoustic properties and nominal dimensions are layered on top of each other to create the equivalent reflector sequence where the impedance mismatch at the interface between any two layers partitions the incident plane wave energy into a reflected wave and transmitted wave. The reflected response from the AID tag is thus engineered to be detectable for an incident acoustic pulse (or pulse train) as is typically transmitted from SONAR systems mounted on AUVs.

An example of a simulated AID tag signature (or template) obtained using alternating acrylic and water layers is shown below in Figure 1.6 for reference. Here, a wideband Gaussian pulse centered at 500 kHz is used as the source signal. The reflected pulse train structure is due to the interfacial reflections between the acrylic and water layers, the full simulation details of which are provided in section 3.3.

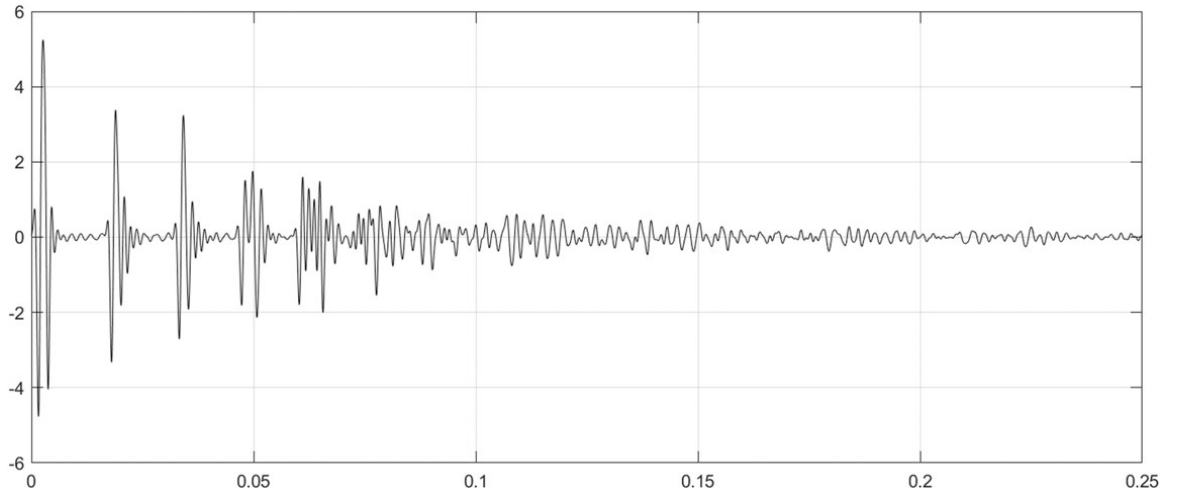


Figure 1.6: An example of an AID tag signature that may be generated using alternating acrylic and water layers. The full simulation details for simulating this signature are provided in section 3.3 and Table 3.1.

Detection methods such as match-filtering [25] of a known template signal of the AID tag (e.g. Figure 1.6), with the SONAR datastream, can be used to identify a deployed tag based on the uniqueness of its reflected waveform with minimal computational and hardware expense. Furthermore, if the AID tag is placed in a known location underwater, the detection of the AID tag signature by the AUV can provide bearing information to the

AUV, or indicate the presence of an object or area of interest as discussed earlier.

Beyond applications for AUV navigation and signaling, other potential applications of AID tags can include mine and asset location, underwater 'safe passage' marking, hydrographic and oceanographic surveys, as well as marking cables or the locations of flexible risers. The advantages of an AID tag system are demonstrated by comparing the proposed AID tag design and deployment with existing navigation techniques, from the context of the design criteria mentioned earlier.

## **1.2 Advantages of the proposed AID tag design**

Optical methods where cameras instrumented on an AUV can identify man-made fiducial markers [12, 13, 26], as in Figure 1.7(a,b), can be used in marking AUV paths and features underwater. However, due to the high attenuation of electromagnetic waves in water [27], which may be further exacerbated in turbid or murky water, cameras have a limited range of view. This issue extends to radio and GPS communications as well, where it is not possible for an AUV to communicate with the host ship unless it surfaces to allow for radio wave transmission in air [10, 11], which may reduce the operating range of the AUV. The use of acoustic waves for underwater navigation and sensing as in SONAR systems is therefore the predominantly used method, with SONARs capable of operating over much larger ranges [28], even in murky water. The proposed AID tags have therefore been designed to operate in tandem with high-frequency SONAR.

This thesis develops a framework for engineering unique acoustic backscattering signatures from the AID tags by varying the tag's geometric and acoustic parameters in order for the AID tag to serve as a navigational marker. Other passive acoustic reflectors have been designed in the past which focus on designs to increase acoustic target strength by means of using either highly reflective fluid filled metallic spheres [29, 30], or by exploiting guided wave returns from spherical shells [31, 32]. Previous work at the Georgia Institute of Technology on passive acoustic markers exploited Bragg scattering physics [33]

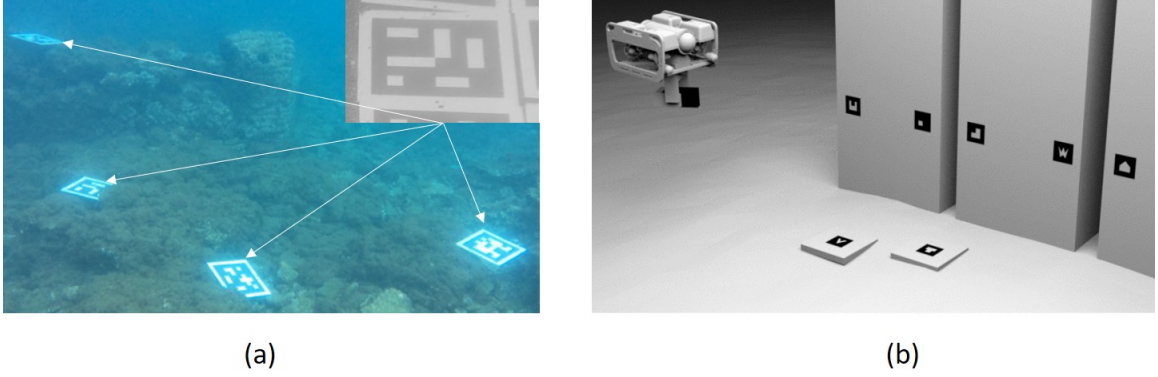


Figure 1.7: (a) An optical fiducial marker [12] with square signatures. (b) A fiducial marker system made of engraved or cut metallic plates, sensed by cameras onboard an AUV [13].

to provide source azimuth and elevation estimates based on the diffracted returns from a periodic metallic grating. In addition to AID tags boosting target strength as in the acoustic reflector examples, the unique capability of designing a backscattered acoustic signature allows for the generation of different AID tag signatures. This in turn enables the deployment of several acoustic tags to convey different instructions or mark multiple locations to the interrogating vessel as shown in Figure 1.4a.

Finally, as AID tags are designed to passively reflect an acoustic signature shaped only by the constituent layers' acoustic properties and geometry and do not contain any circuitry or active components, they are inexpensive to manufacture, and require minimal effort to deploy and use. Furthermore, they respond only when interrogated. In contrast, typical navigation systems, such as an array of active acoustic transponders, send timed acoustic pulses to aid in AUV localization (e.g. short or long baseline systems [14, 34]). They rely on constant signal broadcasting by the transponders and can be expensive to maintain and calibrate in addition to being non-covert.

As mentioned earlier, dead-reckoning is a commonly used navigation method as well, but comes with its own set of challenges. While dead-reckoning might be suitable for small duration missions where AUV position precision is not required, it is not suited for tasks with extended mission times or tasks requiring precise spatial positioning and bearing

estimation such as AUV docking (Figure 1.1a) and optical data transfer (Figure 1.1b). This is attributed to the accumulation of positioning error (Figure 1.8), which arises from sensor drift and measurement errors that accumulate over time [9, 35].

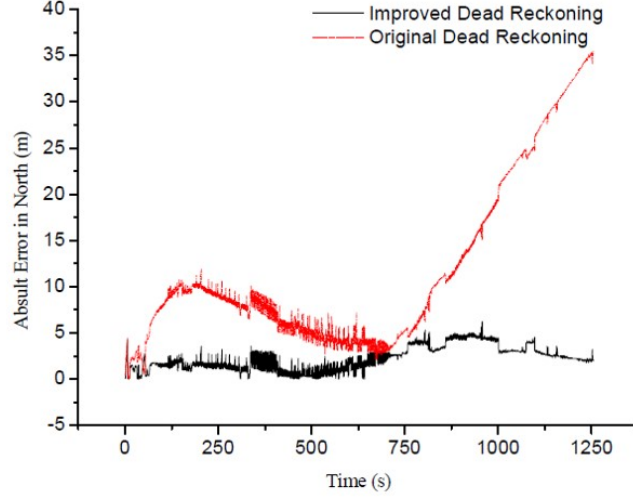


Figure 1.8: Evaluation of sensor drift by Yan et al [36], where typical single direction sensor drift as a function of time is shown in red, and a possible drift correction by the authors shown in black.

While there exist methods to correct for sensor drift [36], they involve complex and regular recalibration which still may be prone to error. Installing an AID tag near the data-transfer station (Figure 1.1b) to indicate its location, for example, can provide an additional reference to augment inertial navigation, thus overcoming the issue of attempting to fly an AUV "blind" to the goal.

### 1.3 Contributions to the Literature

The passive AID tags envisioned and designed in this work add to the existing deployable underwater acoustic infrastructure that aid in AUV navigation and sensing. Furthermore, AID tag design was motivated by the three criteria mentioned earlier i.e. an AID tag must be robustly detectable in different underwater environments, it must be low maintenance and easy to deploy, and the backscattering signature of the AID tag must be unique so the AID

tag can serve as an identification marker. Keeping this in mind, the specific contributions to literature are listed below:

1. The acoustic signatures of AID tags made of horizontally stratified layers of acoustically dissimilar layers were simulated and experimentally verified using a subscale ultrasound setup. Furthermore, tag signature uniqueness is demonstrated using a set of simulated AID tag signatures which are obtained by using different layer combinations.
2. The compressional acoustic velocity and attenuation of common viscoelastic materials were experimentally obtained and reported.
3. In the high-frequency regime (i.e. small incidence wavelength compared to the characteristic dimension of the AID tag), specular scattering from AID tags with multiple spherically and hemispherically stratified layers were shown through numerical simulations to be equivalent to the response from a horizontally stratified AID tag. The simulations also indicated the azimuthal invariance of the backscattered response. Furthermore, the backscattered response of an AID tag assembled using two Stereolithography (SLA) manufactured, concentrically placed, calibrated hemispherical shells, was experimentally obtained using a sub-scale ultrasound setup and validated to be azimuthally invariant, and consistent with numerical simulations.
4. An energy based AID tag design optimization scheme was introduced, and an optimal AID tag layering scheme has been specified.
5. A detectability analysis of AID tag signatures in the presence of interference was conducted, and tag template thresholding strategies to boost the signal-to-interference ratio of the AID tag have been recommended. Additionally, a back-of-the-envelope detectability range has been provided using the active SONAR equation.
6. AID tags designed for high frequency SONAR were experimentally tested and it was



shown that tag signatures could be detected in highly reverberant conditions using extracted AID tag templates. Furthermore, AID tag manufacturing guidelines and SONAR calibration methods are provided and demonstrate the deployability of an AID tag in underwater environments.

## **1.4 Thesis overview**

The organization of the thesis is as follows: Chapter 2 introduces the concept of an AID tag, discusses the numerical modelling of a horizontally stratified AID tag signature, reports experimentally obtained acoustic parameters of materials used in AID tag construction, presents preliminary ultrasound based experimental results of the acoustic signatures obtained from different horizontally stratified AID tags, and validates the experimental results with the numerical model. Chapter 3 extends the AID tag design to tags with spherically stratified shells such that the backscatter from the tag is omnidirectional, and discusses high frequency scattering from the stratified shells through simulation and experiment. Chapter 4 presents an energy based tag design optimization framework for optimal tag signal generation, and presents effective tag layering strategies. Chapter 5 discusses signal processing strategies for AID tag detection near interfering signals and hard interfaces. Chapter 6 discusses experimental results for an AID tag tested in the SONAR regime in a reverberant environment.

## **CHAPTER 2**

### **PASSIVE AID TAGS WITH HORIZONTAL STRATIFICATION**

#### **2.1 Introduction**

Taking inspiration from optical barcodes and SAW RFID tags [18] that are used for object classification tasks, a simple design for an AID tag would comprise of a layering strategy where the geometry and material properties of the layers determine the AID tag's acoustic signature similar to the reflectors of varying thickness and reflectivity used in SAW tags. Specifically, an AID tag can be built of horizontally stratified plates with varying bulk acoustic properties and thicknesses, where the combined layering strategy has an acoustic response that can be distinguished from the tag's surroundings, or other tags. In order to explore this design space, numerical models simulating the acoustic response from stratified media can be used to quickly compute various tag responses. This chapter then proceeds to demonstrate tag signature decorrelation for example tag signatures, and documents preliminary experimental results for horizontally stratified AID tags tested using an ultrasound probe as a proof of concept.

#### **2.2 Analytic simulation of horizontally stratified AID tags**

The Acoustic IDentification (AID) tags in this work are designed by layering elastic, viscoelastic or fluid materials with different bulk acoustic properties and thicknesses. The combination of layers has a frequency response which shapes the reflected response of any bandlimited acoustic source incident on the tag. Since the frequency response of an AID tag is dependent on the material and thickness of each layer and the layering order, unique acoustic signatures can be designed by varying these parameters.

The simplest AID tag geometry to examine is the case of horizontally (or vertically)

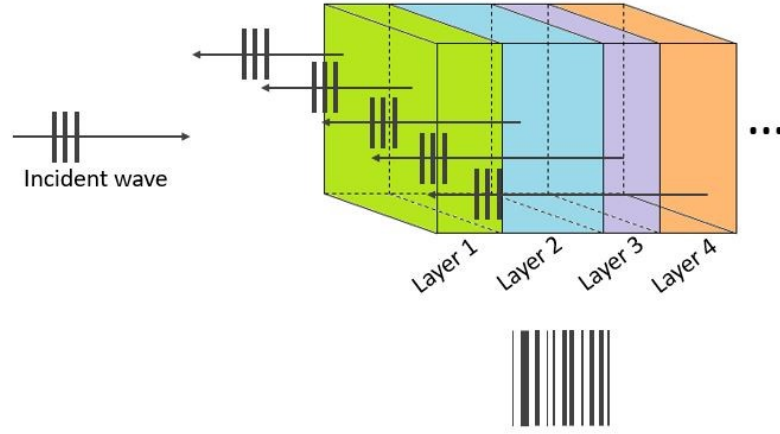


Figure 2.1: A schematic of the structure of an Acoustic IDentification (AID) tag comprising of a number of acoustically dissimilar materials. An incident plane wave reflects from the multiple layer interfaces of the tag to generate a predictable acoustic signature, akin to an optical barcode (shown at bottom).

stratified media, where the layers of the tag are parallel to each other. The frequency response for the case of a horizontally stratified AID tag can be computed analytically by means of the Global Matrix Method [37, 38, 39] which models each layer of the acoustic tag as a 1D (thickness dependent) finite element of an elastic or viscoelastic material, while imposing stress and displacement continuity at the interfaces between the layers (see Figure 2.2). Furthermore, fluid layers can be simulated using the same formulation by setting their shear velocity to a small fraction of the bulk compressive velocity in the medium. In actual implementation, the shear velocity is set to the limit of machine precision. In addition to specifying the layers' compressional and shear velocities, material damping parameters must also be specified for the materials in the tag.

### 2.2.1 Global Matrix formulation

While the full formulation for the numerical solution for the frequency response of a set of horizontally stratified materials is well documented separately in Schmidt and Lowe [37, 38], the main aspects of the derivation are given in brief here, starting with the solution for the displacement field in an infinitely long plate with plane strain assumptions. The elastic

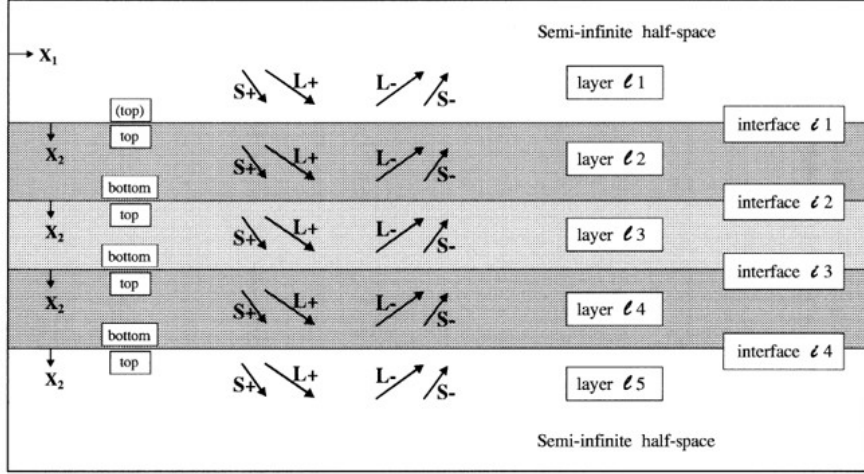


Figure 2.2: Notation used for coordinate system, layers, interfaces, and propagating waves in the Global Matrix formulation [37]

wave equation in terms of the displacement field  $\vec{u}$  in a medium is given by

$$\rho \frac{\partial^2 \vec{u}}{\partial t^2} = (\lambda + 2\mu) \nabla (\nabla \cdot \vec{u}) - \mu \nabla \times \nabla \times \vec{u} \quad (2.1)$$

where  $\vec{u} := \vec{u}(x_1, x_2, x_3, t)$  represents the three-dimensional time varying plate displacement field,  $\rho$  is the density of the plate, and  $\lambda$  and  $\mu$  are Lamé's parameters for the medium. The spatial gradient is specified as  $\nabla := \frac{\partial}{\partial x_1} \cdot \hat{x}_1 + \frac{\partial}{\partial x_2} \cdot \hat{x}_2 + \frac{\partial}{\partial x_3} \cdot \hat{x}_3$ , where hatted quantities denote unit vectors in the specified direction. While Equation 2.1 is specific to wave propagation in elastic solids, the pressure field in a fluid can be computed from the displacement field using the linear Euler equation. The solution of Equation 2.1 is carried out more straightforwardly using the Helmholtz method in which the displacement field is decomposed into a scalar and vector potential solution [40, 41] with harmonic time dependence  $e^{-i\omega t}$  i.e.

$$\vec{u} = \underbrace{\nabla \phi}_{\vec{u}_L} + \underbrace{\nabla \times \vec{\psi}}_{\vec{u}_S} \quad (2.2)$$

Here,  $\phi$  and  $\vec{\psi}$  are the scalar and vector displacement potentials,  $\vec{u}_L$  the longitudinal displacement field, and  $\vec{u}_S$  the shear displacement field. Substituting Equation 2.2 in Equ-

tion 2.1 and simplifying shows that both displacement potentials satisfy the homogeneous wave equations

$$\nabla^2 \phi - \frac{1}{c_L^2} \frac{\partial^2 \phi}{\partial t^2} = 0 \quad (2.3)$$

$$\nabla \times \nabla \times \vec{\psi} + \frac{1}{c_S^2} \frac{\partial^2 \vec{\psi}}{\partial t^2} = 0 \quad (2.4)$$

Where  $c_{L,S}$  are the bulk longitudinal and shear acoustic velocities in the plate medium, given by

$$c_{L,S} = \sqrt{\frac{\lambda + 2\mu}{\rho}}, \sqrt{\frac{\mu}{\rho}} \quad (2.5)$$

and under the assumption of linear frequency dependence of acoustic attenuation, material damping can be handled by specifying complex, frequency dependent  $c_{L,S}$  as

$$c_{L,S} = \frac{c}{1 + i\kappa/2\pi} \quad (2.6)$$

where  $\kappa$  is the frequency dependent attenuation in Nepers per wavelength [37], typically obtained through experiment, and  $c$  is the measured phase velocity. Since both the scalar and vector displacement potentials satisfy the homogeneous wave equation as in Equation 2.3 and Equation 2.4, monochromatic plane wave solutions may be specified to both  $\phi$  and  $\vec{\psi}$  as

$$\phi = A_L e^{i(\vec{k}_L \cdot \vec{x} - \omega t)} \quad (2.7)$$

$$|\vec{\psi}| = A_S e^{i(\vec{k}_S \cdot \vec{x} - \omega t)} \quad (2.8)$$

where

$$\vec{k}_i = k_{i,1}\hat{x}_1 + k_{i,2}\hat{x}_2 + k_{i,3}\hat{x}_3 \quad (2.9)$$

is the wavenumber in an arbitrary direction of propagation where  $i = L, S$  for longitudinal and shear waves respectively, and  $\vec{x} = x_1\hat{x}_1 + x_2\hat{x}_2 + x_3\hat{x}_3$  a field point in three-dimensions.  $\hat{x}_3$  is a unit vector pointed out of the plane of the paper, while  $\hat{x}_1$  and  $\hat{x}_2$  form a right-handed coordinate system as shown in Figure 2.2. The values of the complex longitudinal and shear wave amplitudes  $A_{L,S}$  are to be determined based on the boundary conditions of the problem.

From the plane strain assumption made in this analysis, the solution domain can be reduced to only the length and thickness of the plate and spatial derivatives in  $\hat{x}_3$  may be neglected.

The longitudinal and shear displacements within the infinite plate are finally found as

$$\vec{u}_L = \nabla\phi = \begin{bmatrix} k_{L,1} \\ k_{L,2} \\ 0 \end{bmatrix} \phi \quad (2.10)$$

and

$$\vec{u}_S = \nabla \times \vec{\psi} = \begin{bmatrix} \frac{\partial}{\partial x_1} \\ \frac{\partial}{\partial x_2} \\ 0 \end{bmatrix} \times \begin{bmatrix} 0 \\ 0 \\ \psi_3 \end{bmatrix} = \begin{bmatrix} k_{S,2} \\ -k_{S,1} \\ 0 \end{bmatrix} |\vec{\psi}| \quad (2.11)$$

Here, the vector potential  $\vec{\psi} = \psi_3\hat{x}_3$  points in the  $\hat{x}_3$  direction, restricting shear motion purely to the  $x_1 - x_2$  plane. The displacement solutions in Equation 2.10, and Equation 2.11 may be superimposed within the layer domain to describe more complex dynamics which may arise depending on the boundary conditions enforced at the top and bottom interfaces of each layer. It is also evident from the plane wave solution that the wave propagation along the depth of the plate can be described from the contributions of four vertical components - two oppositely travelling shear waves, and two oppositely travelling longitudinal waves. When the plate is placed adjacent to another plate or fluid, the interface between

the two materials sees the interaction of the four waves from the plate, and four similar waves from the adjacent material. Therefore, any material interface is modelled to handle the interaction of 8 waves - a pair of incident and reflecting longitudinal (L), and shear (S) waves contributed from the top and bottom layers of the interface respectively (Figure 2.2). Waves travelling top-down are annotated with a (+), and waves travelling bottom-up are denoted using a (-). Therefore, a downward travelling longitudinal wave is represented as (L+) for example.

Snell's law is enforced on the interface to handle the horizontal wavenumber invariance in  $x_1$  i.e. the projection of the longitudinal and shear wave numbers onto the interface is invariant to allow for wave superposition along the interface. Mathematically,

$$k_{L,1} = k_{S,1} = k_1 = \frac{\omega}{c_L} \sin \theta_L = \frac{\omega}{c_S} \sin \theta_S \quad (2.12)$$

Where  $\theta_{L,S}$  are the angles of incidence with respect to the normal to the plate in the  $\hat{x}_2$  direction, and  $k_1$  is the horizontal wave number at the interface of the plates. Since the horizontal wave number is invariant over all plates in a stratified system, the term  $e^{i(k_1 x_1 - \omega t)}$  is invariant in all further displacement and stress computations. The invariance along  $\hat{x}_1$  reduces the formulation of the layered system to be only depth dependent.

Additionally, the longitudinal and shear wave numbers in the  $\pm \hat{x}_2$  direction can now be written in terms of the horizontal wave number and the definitions provided in Equation 2.5 for the acoustic velocities in the layer as

$$k_{(L\pm, S\pm),2} = \pm \sqrt{\frac{\omega^2}{c_{(L,S)}^2} - k_1^2} \quad (2.13)$$

which governs the propagation characteristics of the upward and downward travelling waves in the plate system.

To model the interfacial interactions of the waves in the layered system, displacement and stress continuity is enforced at every interface in the plate system. Here, the displace-

ment boundary conditions are the same field equations Equation 2.10, and Equation 2.11 evaluated at the depth of the interface. Stress continuity is written in terms of the displacement fields by means of standard constitutive relations

$$\sigma_{11} = \lambda \nabla \cdot \vec{u} + 2\mu \frac{\partial u_1}{\partial x_1} \quad (2.14)$$

$$\sigma_{22} = \lambda \nabla \cdot \vec{u} + 2\mu \frac{\partial u_2}{\partial x_2} \quad (2.15)$$

$$\sigma_{33} = \lambda \nabla \cdot \vec{u} + 2\mu \frac{\partial u_3}{\partial x_3} \quad (2.16)$$

$$\sigma_{12} = \mu \left( \frac{\partial u_1}{\partial x_2} + \frac{\partial u_2}{\partial x_1} \right) \quad (2.17)$$

$$\sigma_{23} = \mu \left( \frac{\partial u_2}{\partial x_3} + \frac{\partial u_3}{\partial x_2} \right) \quad (2.18)$$

$$\sigma_{31} = \mu \left( \frac{\partial u_3}{\partial x_1} + \frac{\partial u_1}{\partial x_3} \right) \quad (2.19)$$

where  $\sigma_{ii}$  indicate normal stress components in the direction of  $\hat{x}_i$  and  $\sigma_{ij}$  are the shear stress components. Substitution of Equation 2.10, and Equation 2.11 in Equation 2.14 provides expressions containing the displacement wave amplitudes which are to be solved for over the domain. Additionally, only field quantities bound to the  $x_1 - x_2$  plane are of interest in this analysis, and therefore the displacement and stress vectors in a layer can be represented in matrix form as

$$\begin{bmatrix} u_1 \\ u_2 \\ \sigma_{11} \\ \sigma_{12} \end{bmatrix} = \mathbf{C}_l(x_2) \cdot \begin{bmatrix} A_{(L+)} \\ A_{(L-)} \\ A_{(S+)} \\ A_{(S-)} \end{bmatrix} \quad (2.20)$$

where  $\mathbf{C}_l(x_2)$  is the depth dependent coefficient matrix for layer  $l$ , mapping the displacement and stress fields of layer  $l$  to the previously defined wave amplitudes. For known displacement and stress field quantities, the wave amplitudes can be solved for through the



inverse problem of Equation 2.20. The specific terms of the depth dependent coefficient matrix  $\mathbf{C}_l(x_2)$  can be found in [37, 38, 42], and are excluded here.

In a layered system, the contributions of the multiple layers to the reflected acoustic response can be modelled by recursively solving the layer matrix equation (Equation 2.20) at each interface, using the computed field quantities at each layer as the input for the subsequent layer. This form of solution is well known in seismic, and ultrasound literature as the Transfer Matrix or Propagator Matrix method [37, 43, 44]. While effective, the Transfer Matrix method can sometimes be numerically unstable particularly in handling large frequency-thickness ( $fd$ ) products [39].

The Global Matrix method proposed by [38, 39, 42] overcomes this issue by assembling the multiple layer matrices of the stratification into a single "Global" matrix. An  $n$  layer stratification contains  $4(n - 1)$  equations corresponding to the interfacial continuity of the stress and displacement fields. Furthermore, this method is careful to select the spatial origin of the bulk waves in each layer based on the direction of propagation, i.e. upward travelling waves in a layer have their origin at the bottom interface of the layer, while the origin of the downward travelling waves is specified as the top interface. This precaution ensures numerical stability for all  $fd$  products and specifically handles evanescent wave propagation in the layered system. The layer matrices  $C_l$  for layer  $l$  are rewritten in [37] in terms of the modified spatial origins as  $D_{lt}$  and  $D_{bt}$  corresponding to coefficient matrices whose origins are the top and bottom of the layer respectively. For a system of 5 layers for example, the structure of the assembled Global matrix is shown in Equation 2.21 in terms of  $D_{lt}$  and  $D_{lb}$ , where the wave amplitudes in each layer are denoted by  $\{A_l\}$ . After assembly, the entire system can be inverted to solve for displacement amplitudes in a manner similar

to Equation 2.20.

$$\underbrace{\begin{bmatrix} [D_{1b}] & [-D_{2t}] & & & \\ & [D_{2b}] & [-D_{3t}] & & \\ & & [D_{3b}] & [-D_{4t}] & \\ & & & [D_{4b}] & [-D_{5t}] \end{bmatrix}}_{\text{Global Matrix}} \cdot \begin{bmatrix} \{A_1\} \\ \{A_2\} \\ \{A_3\} \\ \{A_4\} \\ \{A_5\} \end{bmatrix} = \{0\} \quad (2.21)$$

To simulate an acoustic tag's reflected frequency response, the material properties and thicknesses of the layers of the tag are used to construct the Global matrix [45]. The top-most and bottom-most layers are specified to be fluid half-spaces in which the tag is submerged, typically water in the current application. A longitudinal plane wave with unit displacement amplitude travelling from the top half-space is set to be the forcing term in the Global matrix, and the frequency dependent reflection coefficient from the tag is found as the complex amplitude ( $A_{(L-)}$ ) of the wave reflected back into the top halfspace. While the Global matrix solution can handle sources incident onto the layered system from any angle  $\theta$  made to the normal to the layers, normal incidence ( $\theta = 0^\circ$ ) is used in all further simulations to obtain the specular reflection sensed by a monostatic transmit/receive setup which is representative of an AUV's SONAR system. The process thus far has described the computation of the frequency response to a monochromatic plane wave, but is readily extended over a frequency sweep to obtain the full frequency dependent reflection coefficient  $R(\omega)$  of the stratification.

Once the reflection coefficient  $R(\omega)$  of the tag is computed, the reflected response of any bandlimited interrogation signal  $x(t)$  such as a Gaussian pulse or a Linear Frequency Modulated (LFM) pulse more typical to SONAR operations can be computed as

$$y(t) = \mathcal{F}^{-1} [X(\omega) \cdot R(\omega)] \quad (2.22)$$

where  $X(\omega)$  is the Fourier transform of the interrogating signal  $x(t)$ , and  $y(t)$  is the time-

domain reflected response of a tag with reflection coefficient  $R(\omega)$ . For clarity, a schematic of the signal processing is shown in Figure 2.3.

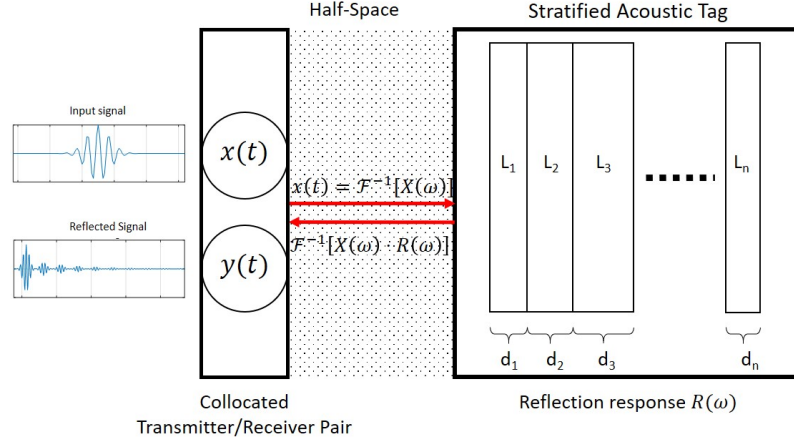


Figure 2.3: Schematic of the simulation of an AID tag response. An input signal  $x(t)$  is incident on an AID tag with reflection coefficient  $R(\omega)$ . The signal collected at the receiver is  $y(t)$ .

### 2.2.2 Modelling Material Damping

In addition to specifying the bulk acoustic properties of the materials of an AID tag, the acoustic attenuation of the material must also be considered in the simulation. Typically, the damping of a material is described in terms of complex Lamé parameters in viscoelastic media which describe the attenuation as a function of material structure, temperature etc. However, these numbers are typically unavailable from the manufacturer, and damping is specified from the amplitude decay measured in backwall scattering measurements of a material sample. From these measurements, it is straightforward to include material damping by specifying complex acoustic velocities computed from the measured absorption.

For example, consider the plane wave solution to the longitudinal (or shear) displacement potential as in Equation 2.7 or Equation 2.8. Here, the wavenumber vector  $\vec{k}$  purely contributes to the longitudinal wave propagation only. If a complex wave number vector  $\vec{k} = \vec{k}_{Re} + i\vec{k}_{Im}$  is instead specified, the displacement potential can be rewritten in terms of

a propagating and attenuating component as

$$\phi, |\vec{\psi}| = A_{(L,S)} e^{i(\vec{k}_{Re} \cdot \vec{x} - \omega t)} \cdot e^{-\vec{k}_{Im} \cdot \vec{x}} \quad (2.23)$$

The complex longitudinal or shear velocity of the plane wave in Equation 2.23 can be expressed in terms of the complex wave  $\vec{k}$  number as

$$c_L, c_S = \frac{\omega}{|\vec{k}_{Re}| + i|\vec{k}_{Im}|} \quad (2.24)$$

which can be further simplified as

$$c_L, c_S = \frac{\omega/|\vec{k}_{Re}|}{1 + i|\vec{k}_{Im}|/|\vec{k}_{Re}|} = \frac{c}{1 + i|\vec{k}_{Im}| \cdot \lambda/2\pi} = \frac{c}{1 + i\kappa/2\pi}$$

where  $c$  is the acoustic velocity in measured in the direction of  $\vec{k}_{Re}$ . Additionally, the magnitude of the imaginary part of the wave number  $\vec{k}_{Im}$  prescribes the rate of decay of the propagating wave per unit length, and therefore the product  $\vec{k}_{Im} \cdot \lambda = \kappa$  indicates that the propagating wave attenuates by  $e^{-\kappa}$  after propagating 1 wavelength. The unit of  $\kappa$  is Nepers/wavelength [Np/ $\lambda$ ]. This method of specifying material damping assumes a linear frequency dependence of acoustic absorption which is well suited for viscoelastic materials [46]. While this is certainly not the general case of damping, and fluid and metal absorption exhibits quadratic frequency dependence [47, 48], AID tags are designed for bandlimited sources over which it is possible to approximate a locally linear frequency dependence on damping.

Material damping is often specified in different units depending on the field of application, ranging from dB/km in long range underwater acoustic propagation, to dB/(cm MHz $^\eta$ ) in ultrasonic experiments, where absorption follows a frequency dependent power law with  $\eta \in [0, 2]$ . Another commonly used unit as mentioned earlier is the Neper [Np], which is defined from the rate of exponential decay of a signal propagating in the attenuating medium. Establishing a clear relationship between the two units is useful in specifying the

accurate material damping parameter for every layer.

Units of dB/length can straightforwardly converted to Np/length from a relationship derived from first principles. If a signal with original amplitude  $A_0$  decays exponentially to an amplitude of  $A_1$  over a length  $z$ ,  $A_1$  may be written as

$$A_1 = A_0 e^{-\alpha(\omega) \cdot z} \quad (2.25)$$

from which the absorption  $\alpha(\omega)$  - temporarily assuming no frequency dependence - can be evaluated by taking the natural logarithm on both sides of Equation 2.25 as

$$\alpha = \frac{1}{z} \ln \frac{A_0}{A_1} \quad (2.26)$$

providing the absorption coefficient in Np/length. If  $A_0/A_1 = e$  over unit length, the attenuation is 1 Np. Therefore, to convert 1 Np/length to dB/length, the base 10 logarithm is applied to the amplitude ratio as

$$20 \cdot \log_{10} \frac{A_0}{A_1} = 20 \cdot \log_{10} e = 8.6859 \text{ dB/length} \quad (2.27)$$

and the conversion from dB/length to Np/length is

$$\text{Np/length} = 0.1151 \cdot \text{dB/length} \quad (2.28)$$

In the case of linear frequency dependence of attenuation, i.e.

$$\alpha(\omega) = \alpha_0 \cdot \omega \quad (2.29)$$

the attenuation coefficient (here  $\alpha_0$ ) may be expressed in terms of the previously mentioned Np/ $\lambda$  units from

$$\alpha_0 = \frac{1}{z \cdot \omega} \ln \frac{A_0}{A_1}$$

which, upon expressing angular frequency  $\omega$  in terms of wavelength  $\lambda$  reduces to

$$\alpha_0 = \frac{1}{z} \ln \frac{A_0}{A_1} \cdot \frac{\lambda}{2\pi c_L} = \kappa \cdot \frac{1}{2\pi c_L} \quad (2.30)$$

relating the standard frequency dependent absorption to the invariant attenuation coefficient  $\kappa$  scaled by a constant. These equations allow for the specification and easy conversion of any acoustic absorption values present in literature and experiments to a common unit. The rest of this work follows absorption units of  $\text{Np}/\lambda$ .

### 2.2.3 Global matrix method validation

In order to validate the performance of the Global matrix method in simulating layered tag systems, a simple case study of a single plate placed between two water half-spaces may be conducted. After solving for the frequency dependent wave amplitudes using Equation 2.21, the full spatio-temporal normal stress field (acoustic pressure in fluids) can be computed in the top and bottom half-spaces, as well as over the depth of the plate. Assuming no material damping is applied to the layers, the energy reflected and transmitted through the system is purely due to impedance mismatch between adjacent layers. Therefore for a wideband pulse incident onto the plate from the top half-space, the reflection and transmission coefficients as evaluated from the pulse decay measurements from the Global matrix simulation can be compared to the standard analytical formulation for pressure reflection and transmission coefficients [49] i.e.

$$R = \frac{(Z_1/Z_2) - 1}{(Z_1/Z_2) + 1} \quad (2.31)$$

$$T = \frac{2(Z_1/Z_2)}{(Z_1/Z_2) + 1} \quad (2.32)$$

where  $Z_1$  and  $Z_2$  are the characteristic acoustic impedances of the top and bottom material being compared.

For example, Figure 2.4 shows the spatio-temporal propagation of an incident 6 MHz Gaussian pulse through a 6 mm thick aluminum plate in the left panel. The incident pressure interacts with the water-aluminum interface at 0 mm depth, and aluminum-water interface at 6 mm depth (both marked by horizontal black lines), and reflects and transmits acoustic pressure across these boundaries. The temporal evolution of the incident pressure is tracked along the X-axis, and time histories at any depth can therefore be extracted from the corresponding row of the spatio-temporal matrix. In order to compute the pressure reflection and transmission coefficients at the top and bottom interfaces, time-histories from the top water layer, the aluminum layer, and bottom water layer at arbitrary depth points within the layers are extracted (marked in red). Pressure ratios are taken as indicated by the matching colored boxes in the center panel between successive pulse returns to obtain the measured reflection and transmission coefficients at each interface.

For the case of aluminum-water interfaces, the ratio of aluminum to water impedances  $Z_{Al}/Z_{water} = 11.34$ , which when substituted in Equation 2.31 provides the computed reflection and transmission coefficients. The computed and measured reflection and transmission coefficients match closely with each other, and more specifically, the reflection coefficient in the top water layer where the AID tag signature is to be detected is less than 2.5% off from the theoretical value, thus validating the Global matrix implementation.

Repeating the validation technique for a viscoelastic material - here a 6 mm acrylic plate with  $Z_{acrylic}/Z_{water} = 1.842$  - with the same incident Gaussian pulse, the pressure

reflection coefficient into the top water layer is around 1% off from the theoretical value. Thus, the Global matrix method can be readily used to simulate more complex layered systems.



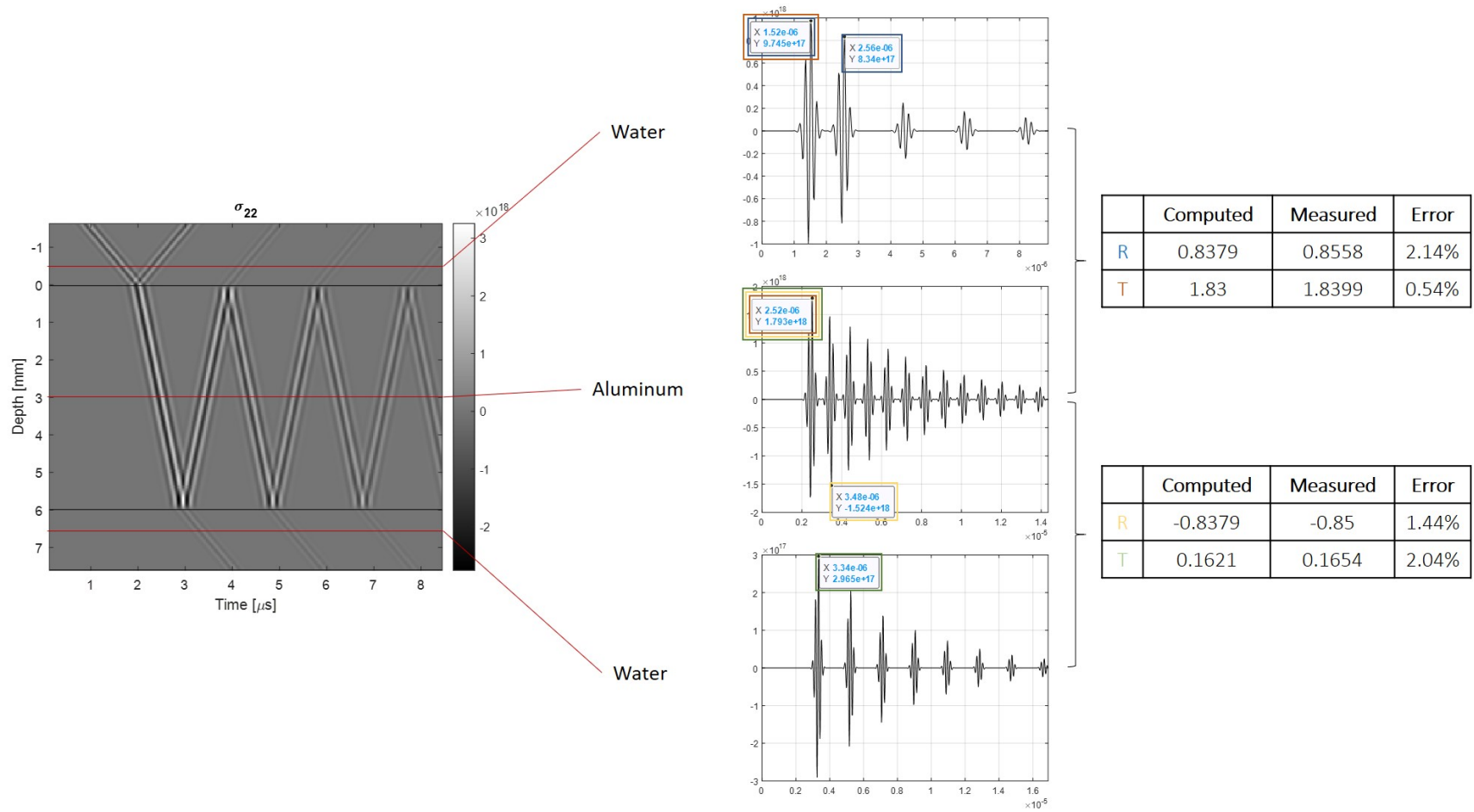


Figure 2.4: Verification of the Global matrix method solution using standard reflection coefficient for aluminum plate. Left panel indicates the full spatio-temporal evolution of an incident Gaussian pulse on the aluminum plate from a top water layer.

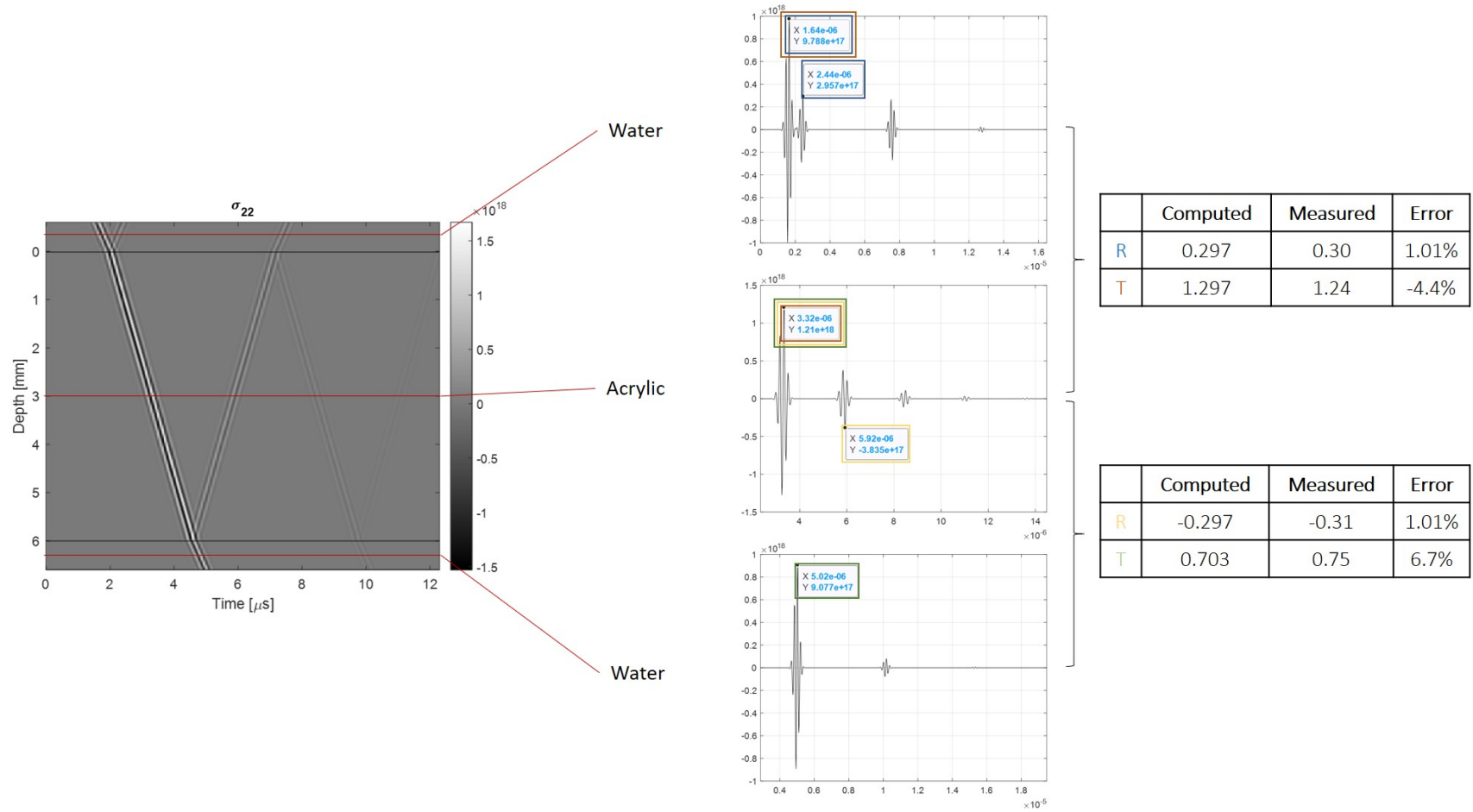


Figure 2.5: Verification of the Global matrix method solution using standard reflection coefficient for acrylic plate. Left panel indicates the full spatio-temporal evolution of an incident Gaussian pulse on the acrylic plate from a top water layer.

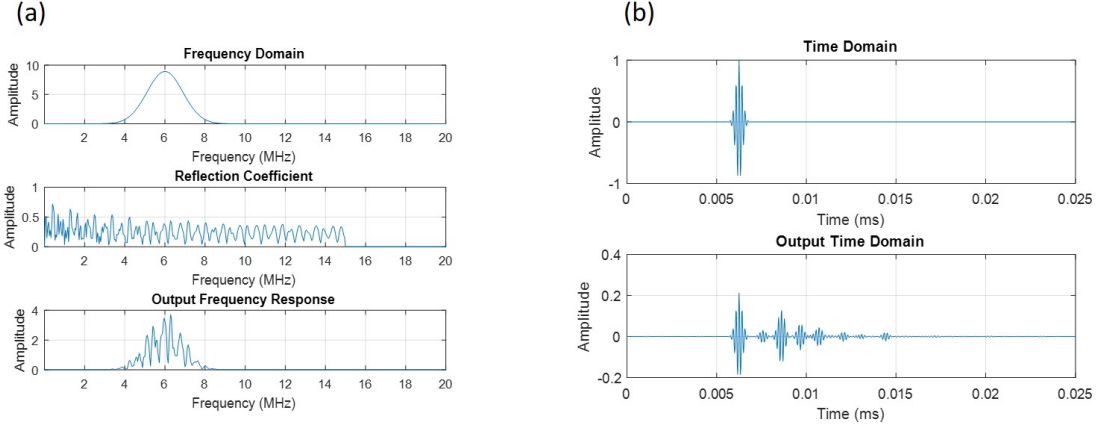


Figure 2.6: Evaluation of the temporal response of a four-layer horizontally stratified AID tag comprised of HDPE, acrylic, PVC, and polycarbonate. (a) Left column of subplots from top-down indicate the original source spectrum, the computed reflection coefficient for the AID tag, and the evaluated AID tag frequency response. (b) Right column of subplots from top-down indicate the original source in the time domain, and the temporal response of the simulated AID tag.

As an example of simulating a more complex layered system, a four layer, horizontally stratified AID tag comprising of 1.5 mm thick High Density Polyethylene (HDPE), Polyvinyl Chloride (PVC), acrylic, and polycarbonate sheets is simulated for a wideband Gaussian incident pulse centered at 6 MHz as in Figure 2.6. The left column of Figure 2.6 indicates the spectrum of the incident source, the AID tag's reflected frequency response, and the output spectrum obtained, while right column indicates the AID tag's computed temporal signature which can be used to identify the tag.

### 2.3 Modelling a library of unique acoustic signatures

Using the Global matrix method simulation framework as described in the previous section, it is possible to design unique AID tag backscatter signatures through varying the material and thickness parameters of the individual layers of the tag [45]. Furthermore, once a library of signatures is created, it is important to quantify the uniqueness of the generated AID tag signatures relative to each other. In other words, it is necessary to evaluate how decorrelated the tag signatures are. The higher the signature decorrelation, the easier it

becomes to separate different tags from one another.

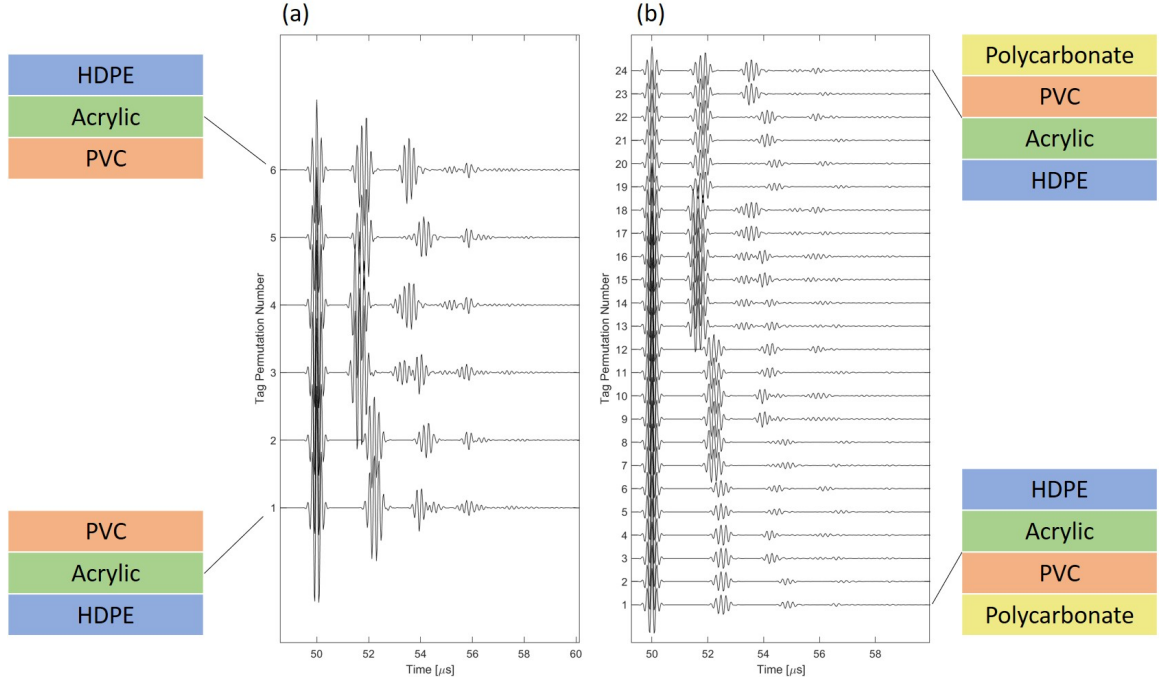


Figure 2.7: (a) Example tag signatures generated by permuting 3 different layers with arbitrarily selected material parameters and thicknesses. The first (Tag permutation number 1) and last (Tag permutation number 6) layer permutations are indicated for reference. (b) Example tag signatures generated by permuting 4 different layers with arbitrarily selected material parameters and thicknesses. The first (Tag permutation number 1) and last (Tag permutation number 24) layer permutations are indicated for reference.

As an example, it is possible to generate  $4! = 24$  tag signatures if a selection of four materials - here for illustrative purposes a 2 mm thick HDPE, 2.5 mm thick PVC, 2.25 mm thick acrylic, and 2.75 mm thick polycarbonate sheet each with different acoustic properties - are permuted as in Figure 2.7b.

By means of a normalized cross-correlation metric, the time-histories of each of the 24 reflected AID tag signatures can be compared to every other signature in the library to generate a correlation matrix as in Figure 2.8e. Here, the normalized cross-correlation between two signatures  $y_1(t)$  and  $y_2(t)$  is given by

$$R_{y_1, y_2} = \max \left( \frac{|y_1(t) * y_2(-t)|}{\sqrt{R_{y_1, y_1}(0) \cdot R_{y_2, y_2}(0)}} \right) \quad (2.33)$$

where  $*$  is the convolution operator, and the cross-correlation  $R_{y_1, y_2}$  is normalized by the autocorrelation of the individual signals  $R_{y_1, y_1}$ ,  $R_{y_2, y_2}$  at zero lag as shown for example in Figure 2.8(a-c).

The resulting cross-correlation matrix (Figure 2.8e) computed from the 24 different signatures allows for the selection of tag designs which are maximally decorrelated from each other. The diagonal elements of the cross-correlation matrix are all unity to correspond to perfect correlation of a tag signature with itself, while the darker regions in blue indicate signatures which are decorrelated from each other. The correlation matrix is symmetric about the main diagonal. The extent of decorrelation can be modified by suitably changing materials and layer thicknesses of different tags. In fact, cross-correlation matrices can be generated for AID tags with an arbitrary number of layers. For example, simulating AID tag signatures for tags with three layers (HDPE, PVC, and acrylic) as shown in Figure 2.7a, produces a corresponding cross-correlation matrix as in Figure 2.8d. Some entries in the correlation matrices with high correlation coefficients when comparing dissimilar layer combinations suggest that a potential misclassification of the acoustic tags may occur due to lack of uniqueness in their backscattered response. Careful selection of the library of allowed layer permutations i.e. using a subset of the AID tag designs which decorrelate with one another, would avoid such classification failures. More obviously, it is evident from the comparison of the correlation matrices for three and four layer AID tags that the increased library richness (more number of signatures) generated by the four layer combinations provides more tag designs that decorrelate well with each other.

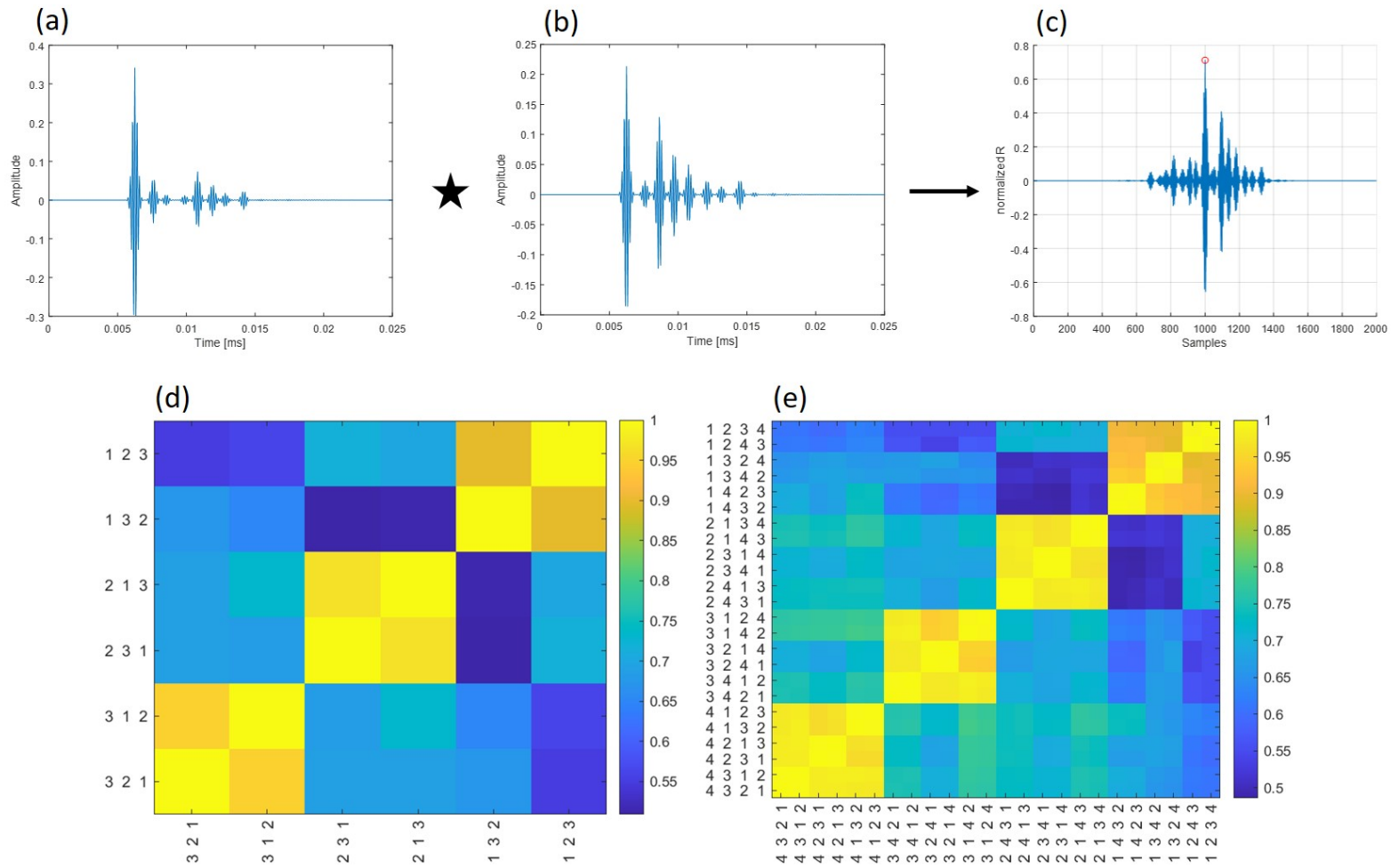


Figure 2.8: (a) Signature obtained from a HDPE-acrylic-PVC-polycarbonate tag (b) Signature obtained from a HDPE-PVC-acrylic-polycarbonate (c) Output cross-correlation of the signatures (a) and (b). (d) Correlation map for an AID tag designed with three layers as in Figure 2.7a. (e) Correlation map for an AID tag designed with four layers as in Figure 2.7b.

Additionally, in order to further decorrelate tag signatures with each other, an amplitude threshold can be applied to the tag signature being compared before cross-correlation. This clips the dominant first reflection from the tag response, and correlates the details of the tag response which arise from the interfacial reflections, which are more unique to each tag.

It is to be noted that the correlation maps presented here are not representative of the best AID tag configurations possible. Here, the lowest correlation observed between AID tag signatures is around 0.5. AID tag design strategies and optimization with a more principled approach to geometry selection will be discussed in chapter 4, while thresholding performance will be discussed in detail in chapter 5.

## **2.4 Experimental testing of horizontally stratified AID tags**

With the basic simulation framework in place to generate signatures for horizontally stratified AID tags, a preliminary experiment was designed to validate the numerical model. The experiment comprised of two stages - the fabrication of horizontally stratified AID tags, and the response characterization of the constructed tag. Taking advantage of the fact that the acoustic backscatter from any object is dependent on the size of the object relative to the insonifying wavelength, sub-scale AID tag configurations could be tested using an ultrasound setup before designing tags suitable for operation with SONAR. This setup allowed for quick prototyping of different tag combinations and avoided having to construct very large tags without the tag response being validated.

### 2.4.1 Sub-scale experimental setup

In order to calibrate the properties of the materials used in constructing AID tags, and to measure the acoustic response from different AID tag designs, a 128 element linear ultrasonic probe (Ultrasonix L14-5/38) [50] was suspended in a water bath, while a mount was placed in front of the probe to place the AID tag or material specimen. The probe transmitted a wideband Gaussian pulse centered at 5.68 MHz, with a fractional bandwidth of 0.69,

as computed from the calibration spectrum plotted in Figure 2.9b. The corresponding pulse in the time domain is as in Figure 2.9c.

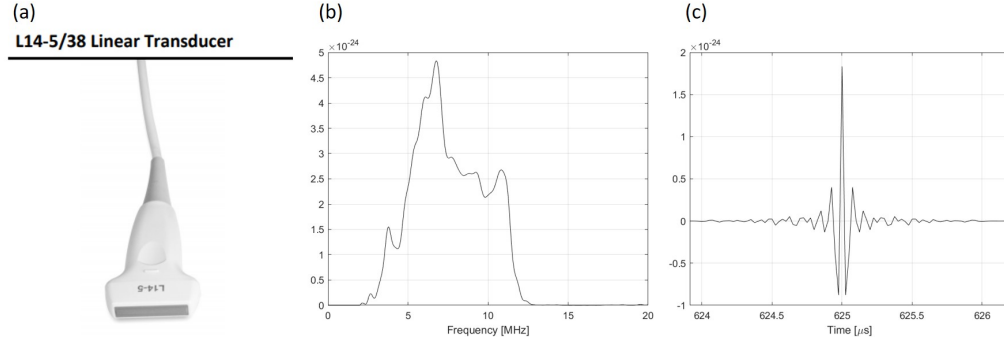


Figure 2.9: (a) Ultrasonix L14 5/38 Ultrasound probe head. (b) Ultrasound probe transmit signal spectrum. (c) Transmit signal pulse shape.

Prior to immersion, the head of the probe was coated with Parker Aquasonic 100 Ultrasound Transmission Gel (Parker Labs, Fairfield, New Jersey), and the probe was waterproofed in a thin nitrile covering. The specimen mount was maintained at a distance of approximately 3 inches ( $\sim 7.5$  cm) from the probe to ensure that the specimen lay within the far-field regime of the probe. Furthermore, the 3 in distance was chosen to minimize the strong propagation losses that high frequency ultrasound experiences underwater (see Figure 2.10)

The horizontally stratified AID tag or materials being tested were placed such that the main lobe of the incident pulse was approximately normal to the tag surface such that the specular reflection is recorded. The thickness of any layer of an AID tag, or material sample was selected to be greater than two pulsewidths of the transmitted ultrasound pulse in the layer medium, where pulsewidth is defined at the half-power point (corresponding to the -6 dB point of the pulse amplitude). For the ultrasound probe, layers were therefore selected to be greater than 1 mm. Furthermore, care was taken to ensure that the surface area of the specimen was large enough to accommodate the entire main beam of the ultrasound to avoid any edge diffracted returns. The ultrasound probe was programmed to transmit a single Gaussian pulse (Figure 2.9b) onto the stationary test specimen in intervals of 1



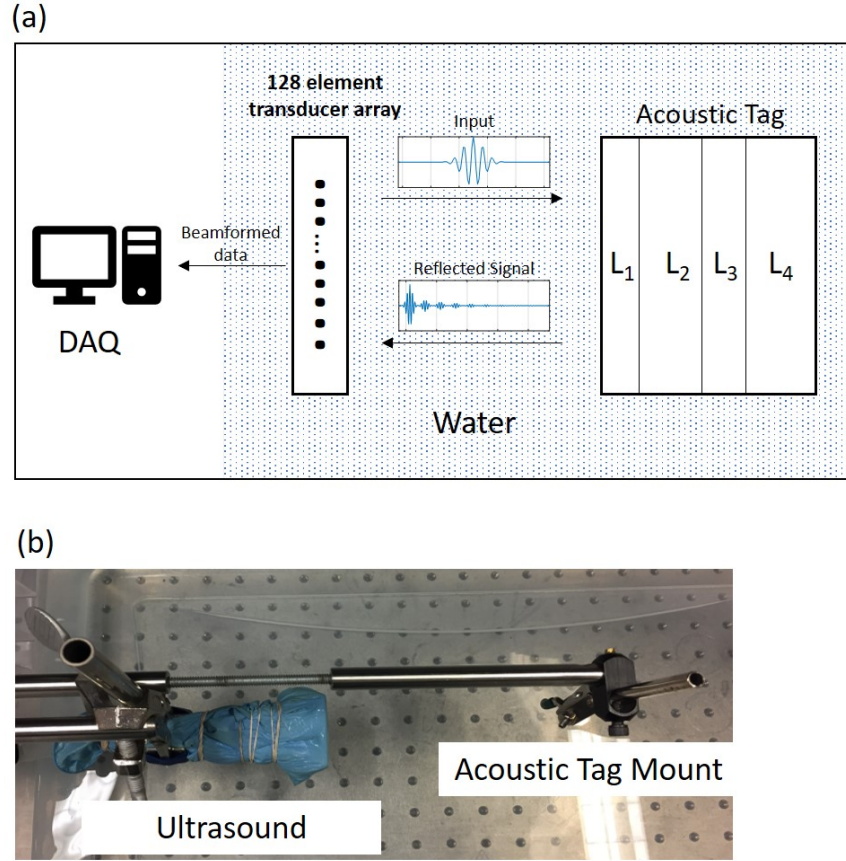


Figure 2.10: (a) Schematic of the data processing using the ultrasound probe. (b) Ultrasound probe and tag mount setup in a water bath.

second to allow sufficient time for tank reverberation to decay before the next pulse was transmitted. Data was collected by a collocated receiver, and sampled at 40 MHz by the digitizer on-board the Ultrasonix medical ultrasound system (Figure 2.3). The multiple recordings from each trial were averaged to reduce measurement noise, and the resulting data were used in further processing.

#### 2.4.2 Material selection

In order to be able to detect the multiple layers of an AID tag, the materials used in the tag layers should allow acoustic energy to transmit through, and interact with each layer interface of the AID tag. In order to accomplish this, care was taken to select materials which when placed adjacent to each other, had an impedance mismatch which allowed a

sufficient amount of energy to transmit across the interface between the two materials while still reflecting enough energy so as to contribute to the backscattered signature of the AID tag. Here, the acoustic impedance of a material, denoted by  $Z$  with units Mrayl, is the product of acoustic velocity ( $c_{L,S}$ ) and material density ( $\rho$ ), while the impedance mismatch is the difference in acoustic impedances of two materials  $\lambda$ .

As AID tags have been designed to be submerged in water, a minimum requirement was to select materials that had an acoustic impedance similar to that of water to limit the impedance mismatch. To this end, viscoelastic materials such as acrylic, HDPE, PVC, polycarbonate, etc. were used. Metals such as aluminium have very large acoustic impedances almost 10 times that of water (see Figure 2.11) and therefore will reflect a majority of the incident acoustic energy on them, and are unsuitable for the first few layers of the tag. However, metals can be used as the last layer of an AID tag to reflect as much energy from the AID tag as possible.

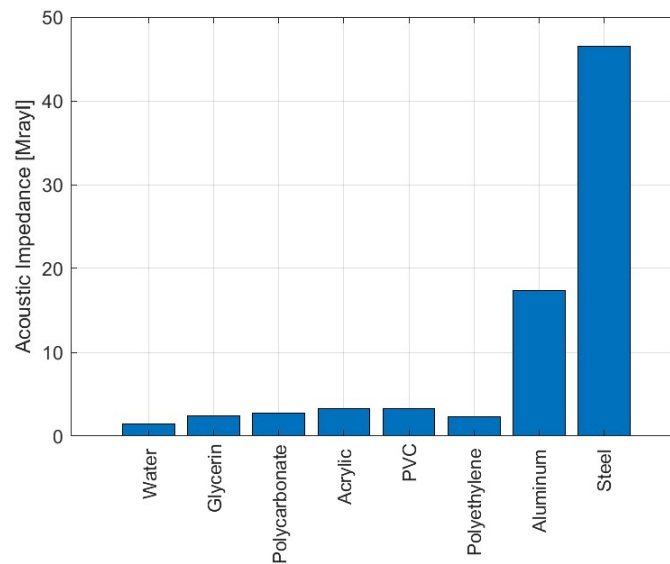


Figure 2.11: Material impedances in Mrayl for different viscoelastic materials and common metals.

### 2.4.3 Material calibration

Prior to measuring the backscattered response from a layered AID tag, the compressional acoustic velocity and attenuation coefficient of the various plastic sheets used were first characterized individually to provide the required input material parameters for the numerical predictions of the AID's backscattered responses as those values are typically not provided by the manufacturer, or may vary from standard datasheets available.

Backwall scattering experiments were conducted for five different plastics considered in the design of AID tag, namely Polyethylene Terephthalate Glycol (PETG), acrylic, HDPE, PVC, and polycarbonate. The time delay between successive pulses in the experiment were used to determine the compressional acoustic velocity of the materials using

$$c_L = \frac{2z}{t_1 - t_0} \quad (2.34)$$

and the frequency dependent attenuation coefficient  $\alpha$  in [nepers/wavelength] is computed using the relation

$$\alpha = \frac{\lambda}{2z} \ln \left( \frac{A_0}{A_1} \right) \quad (2.35)$$

Where  $A_{0,1}$  are the amplitudes of the first (front of plate) and second (back of plate) wall reflections from the rectified signal recorded at times  $t_{0,1}$ ,  $z$  the measured thickness of the test sample, and  $\lambda$  the wavelength of the center frequency of the pulse. Figure 2.12 shows the backwall scattering measurements for the different materials, where each plot is obtained by normalizing the absolute value of the pulse return, relative to the maximum amplitude over the acquisition. The coordinates  $(t_{0,1}, A_{0,1})$  indicate the values used in computing  $c_L$  and  $\alpha$  for each material.

Additionally, the acoustic attenuation in water is calculated from Ainslie and McColm [51, 52] for sources centered around 6 MHz, and 500 kHz, while the attenuation coefficient of glycerine is measured from the loss across two sandwiched plates with known acoustic parameters.

A consolidated table of these experimentally obtained material parameters, along with the acoustic properties of some common fluids and metals is provided in Appendix B.

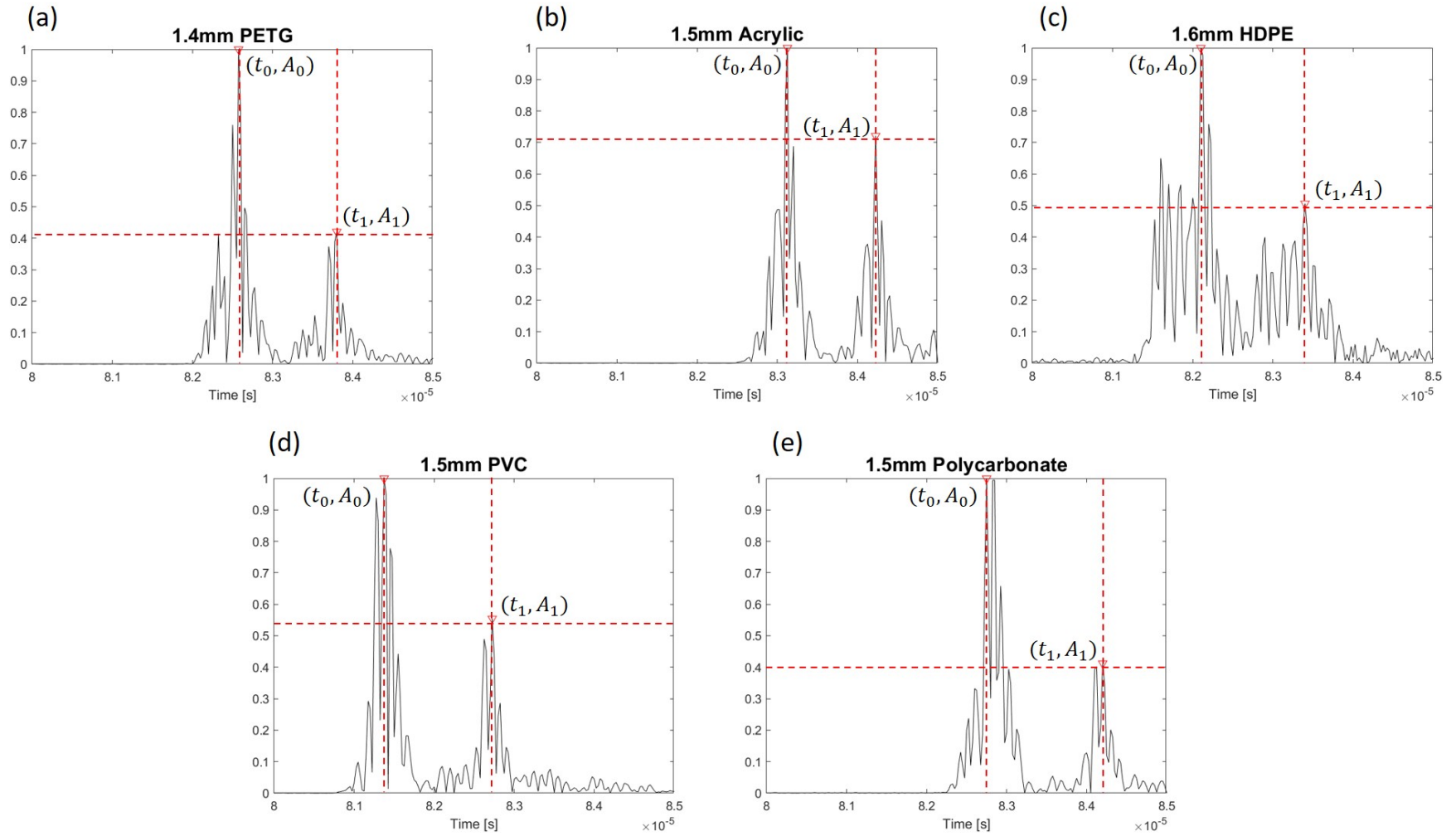


Figure 2.12: Material characterization from backwall scattering experiments for different viscoelastic materials. The absolute value of the echoes measured from (a) a 1.4 mm PETG plate, (b) a 1.5 mm acrylic plate, (c) a 1.6 mm HDPE plate, (d) a 1.5 mm PVC plate, (e) a 1.5 mm Polycarbonate plate are plotted. The coordinates  $(t_{0,1}, A_{0,1})$  indicate measurement points used in the determination of acoustic properties.

#### 2.4.4 Horizontally stratified AID tag fabrication

The horizontally stratified AID tag is the simplest design iteration studied in this research. Furthermore, the first attempt at manufacturing these AID tags comprised of stacking thin layers of different plastics such as acrylic, polycarbonate, HDPE, PVC etc. with varying acoustic impedances and thicknesses on top of each other. Maintaining material continuity between each layer was necessary to accurately approximate the displacement and normal stress continuity constraints applied in the numerical simulations. For this reason, two construction approaches were considered – the use of a methacrylate welding solvent called Scigrip 4 (Scigrip Adhesives, Durham, North Carolina) which creates molecular bonds between dissimilar thermoplastics, or the use of a conforming fluid acoustic couplant such as glycerin between each layer. As the use of Scigrip limited the design space to thermoplastics with very similar material properties, it was not suited to design a large library of acoustic tags.

Instead, thin coatings of glycerin were applied between each layer of the tag before the edges of the tag were sealed using silicone paste. The acoustic impedance of glycerin is similar to the plastics mentioned above [53] and is commonly used as a phantom in non-destructive evaluations of metals and plastics. The transmission loss due to impedance mismatch through the glycerin layer was minimized, although attenuation through glycerin layers is considerable. Provided the film of glycerin is thin enough, the effects of acoustic attenuation through the glycerin couplant can be minimized, and several layer combinations can be obtained. As will be demonstrated in chapter 4 it has been found that the use of water as the acoustic couplant is the more preferable design choice, however flat plate experiments with water coupling have not been conducted as glycerin worked well for the proof of concept.

Since the numerical simulations also assume that the horizontally stratified plates are of infinite length and width, care was taken to ensure that the tag-cross section would completely contain the beamwidth of the ultrasound. This additionally prevented edge

diffraction effects from corrupting the tag's backscattering signature, which was a design constraint mentioned in the previous subsection.

Several AID tags were fabricated in this initial phase but for representative purposes, this report shows a two layer tag comprising of acrylic (1.5 mm thick) and HDPE (1 cm thick) bonded using Scigrip (Figure 2.13a), and a four layer tag comprising of polycarbonate (1.6 mm), acrylic (1.7 mm), HDPE (1.6 mm), and PVC (1.5 mm) with a glycerin couplant between each plastic layer as in Figure 2.13b.

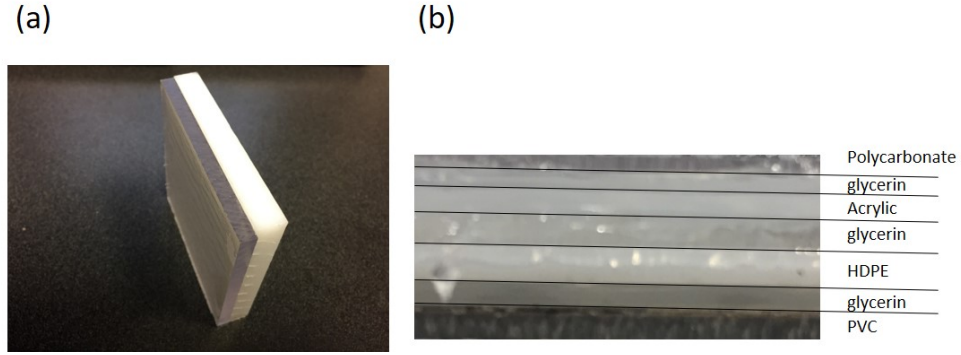


Figure 2.13: (a) Fabricated two layer AID tag. (b) Fabricated four layer AID tag.

#### 2.4.5 AID tag response measurements

As a proof of concept, a two layer tag made of 1.5 mm thick Polycarbonate and PVC sheets, and a four layer tag made of 1.6 mm Polycarbonate-1.7 mm Acrylic- 1.6 mm HDPE- 1.5 mm PVC sheets were constructed and tested using the setup shown in Figure 2.10, these tags were insonified by the ultrasound probe. The acoustic backscatter time series detected by the receiver was then compared to the AID tag response generated by the Global matrix simulation by the correlation metric described in Equation 2.33. Even by visual inspection of Figure 2.14(a, c), it is possible to notice that the arrival structure of the interfacial echoes from the tag layers match well between experiment and simulation. Normalized cross-correlations upwards of 0.75 are observed between simulation and experimental data, with  $R = 0.9$  for the two layer tag (Figure 2.14a), and  $R = 0.75$  for the four-layer tag (Figure 2.14c). Without going into the specifics in this section, the simulated tag signature

is also thresholded to 20% its peak amplitude (level indicated by the dotted lines in Figure 2.14(a-d)) and cross-correlated with the experimental realization. The thresholding focuses on the later details of the tag signature, while truncating some contributions of the dominant first arrival. In both the two layer and four layer tag cases, the thresholded cross-correlation value between simulation and experiment is around 0.7. While the thresholding reduces the overall correlation of between simulation and experiment, it will be shown that this technique boosts AID tag detection in noisy environments in chapter 5.



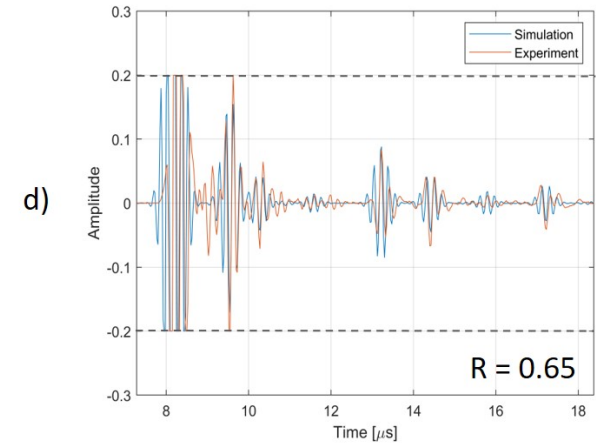
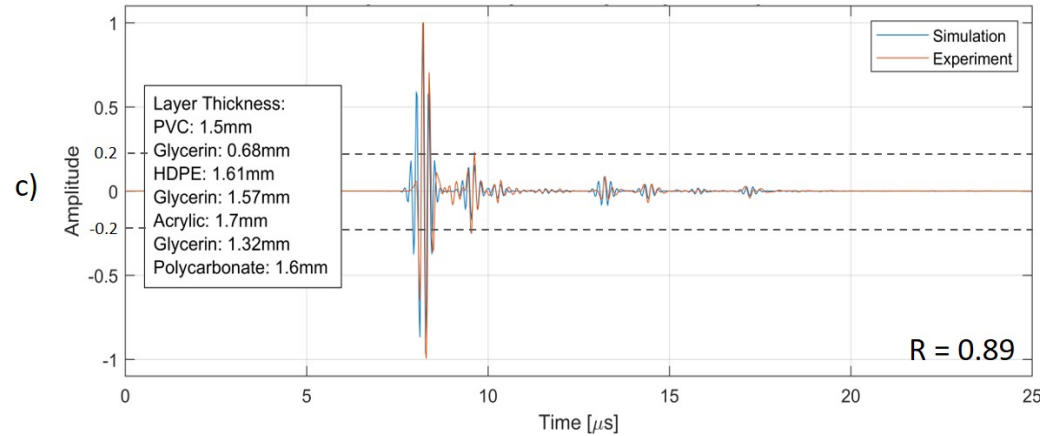
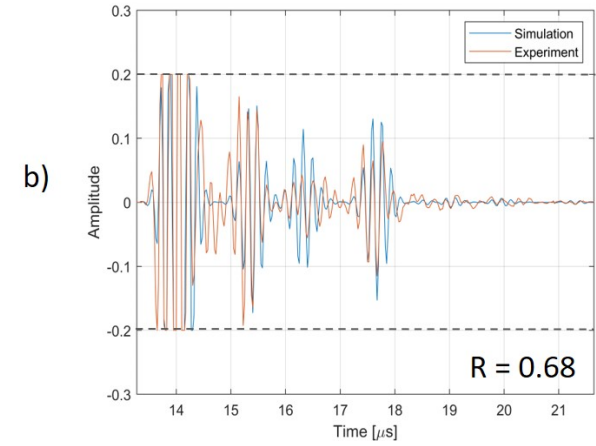
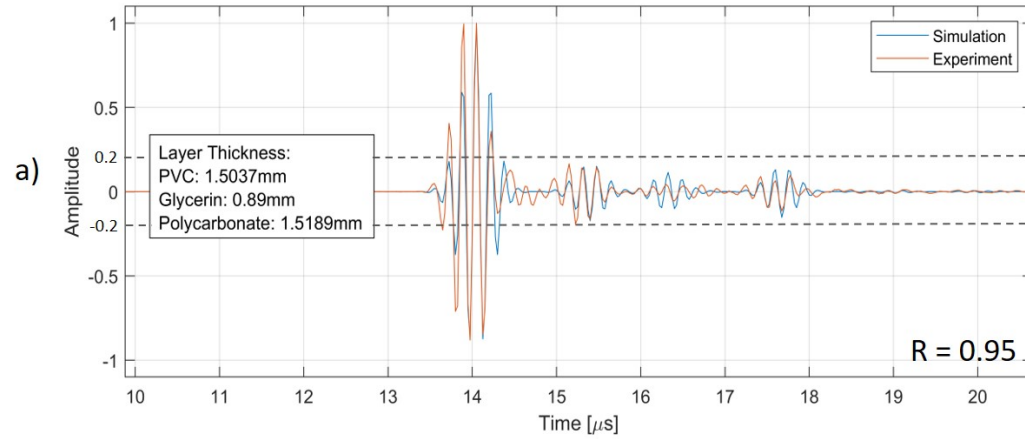


Figure 2.14: (a) Experimental data (orange) of a two layer AID tag with compared to the simulated tag signature (blue) for the same material properties. Here, no template thresholding has been applied before correlation. (b) The same comparison between the experiment and simulation of a two layer AID tag in (a), now with a 20% amplitude threshold applied to the simulated signature before correlation (c) Experimental data (orange) of a four layer AID tag with compared to the simulated tag signature (blue) for the same material properties. Here, no template thresholding has been applied before correlation. (d) The same comparison between the experiment and simulation of a four layer AID tag in (c), now with a 20% amplitude threshold applied to the simulated signature before correlation. It is noted in both (a) and (c) that only the plastic layers of that tag are considered in the total number of layers of the tag.

## **2.5 Chapter Summary**

This chapter introduced the design of a horizontally stratified AID tag, made of different viscoelastic layers. The acoustic signature of an AID tag with arbitrary layer specifications was simulated using the Global Matrix method, and the uniqueness of the simulated AID tag signatures was demonstrated using cross-correlations. Furthermore, as a proof of concept, two horizontally stratified AID tags were manufactured, and the simulated AID tag signature for the corresponding layer combinations were validated using ultrasound backscatter measurements from the manufactured tags. As a part of the experimentation, the acoustic parameters of numerous viscoelastic materials were found using backwall scattering measurements.

## CHAPTER 3

### PASSIVE AID TAGS WITH OMNIDIRECTIONAL BACKSCATTER

#### 3.1 Introduction

One potential limitation of the horizontally stratified tag (i.e. a tag with flat interfaces) is that the scattered response is dependent on the angle of incidence of the interrogating signal. In the typical case of monostatic sensing (i.e. where the source and receiver are collocated), any off-normal incident wave reflects away from the surveying vessel (see Figure 3.1a), and the backscattered signal cannot be detected. This chapter therefore proposes a curved tag design also as described in [54], whose backscattering response is more omnidirectional. Intuitively, this can be accomplished by concentrically layering curved shells of acoustically dissimilar materials to constitute the AID tag (see Figure 3.1b), rather than using flat plates. Therefore, any incident plane wave  $p_{inc}$  is reflected directly back to the source as  $p_{scat}$ . Furthermore, concentric spherical, hemispherical, or cylindrical shells can be designed such that their resultant backscatter for any radially incident acoustic source can still be approximated to the response from a flat plate which is more straightforward to simulate. The remainder of this chapter focuses on the theory and experimental results of AID tags designed with spherical and hemispherical symmetry.

Starting with a brief introduction to the analytical formulation for the backscattered response from a spherical shell, this chapter introduces the notion that sizing the constituent shells of an AID tag to lie in the 'geometric acoustics' regime where the dimensions of the AID tag are large relative to the wavelength of the source, allows for the flat plate approximation to be valid. It is demonstrated, however, that analytical results for shell scattering at high frequencies are unstable. Therefore, to support the flat plate approximation, the scattered field of an AID tag submerged in water, as computed by a finite difference solver,

is compared to the response from the global matrix method for the flat plate analog of the same AID tag. Using the same sub-scale experimental setup as discussed in chapter 2, the response from an AID tag comprised of concentric 3D printed hemispherical shells is reported, and validated with the flat plate code. Measurements from varying azimuths are also reported to demonstrate the omnidirectional nature of the scattered response from the AID tag.

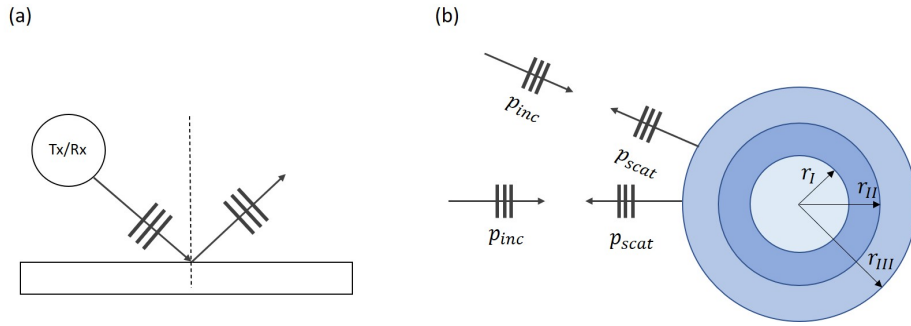


Figure 3.1: (a) Schematic demonstrating how an incident plane wave from a monostatic transmit/receive system onto a flat plate is reflected away from the vessel if not normally incident. (b) Schematic of the proposed curved tag geometry comprising of concentric shells with radii  $r_I$ ,  $r_{II}$ , and  $r_{III}$  which scatters incident acoustic waves back the same direction.

### 3.2 Scattering from an elastic spherical shell

Scattering from elastic shells, particularly with simple shapes such as spheres and cylinders, has been studied in detail in underwater acoustic research for the detection and classification of objects buried under or resting proud on the seabed [55], classification of marine life [56], the design of acoustic targets for use by SONAR systems [30, 31, 32], non-destructive evaluation and inspection of underwater pipelines [57], underwater archaeology etc. More specific to the design of AID tags with an omnidirectional response, methods of target detection and the analysis of the scattering from simple man-made spherical shells is of keen interest. Numerous analytical and experimental results [58, 59, 60, 61, 62] have been reported which describe the mechanics and acoustic structure of the scattering from single

spherical shells. This work extends the current analysis to scattering from multilayered shells with specific geometric constraints as will be described in the next section.

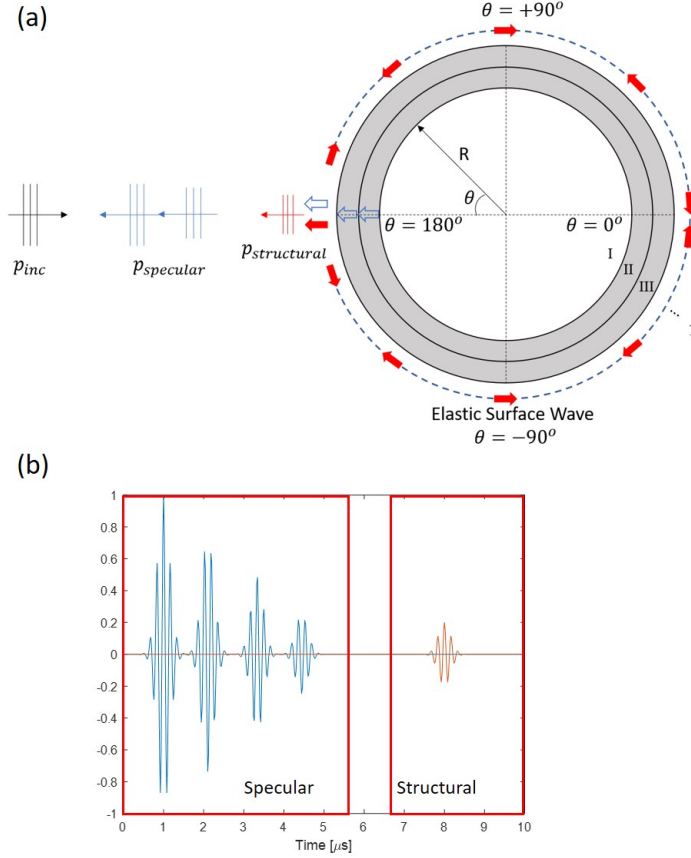


Figure 3.2: (a) A schematic representing the scattering physics for  $N$  concentrically layered spherical media (fluid or solid). The marked  $N$ th layer corresponds to the fluid halfspace, and layer  $I$  corresponds to the fluid core, with radius  $R$ . The angular convention used in simulations are marked. Incident plane waves generate the marked blue specular response and red structural response. The hollow arrows indicate interfacial specular reflections, and filled red arrows the ray path of the surface waves. (b) An example of a backscattering signature where the specular component arrives before the structural response. The specular component can be tuned depending on the layering strategy used.

The scattering from a submerged spherical shell with a fluid core can be qualitatively described as comprising of two main wave interactions - the specular reflection from the thickness of the shell in the direction of incidence, and the clockwise and anticlockwise creeping or elastic surface waves corresponding to the  $A_0$  (or zeroth-order anti-symmetric) leaky Lamb mode of the shell. Here the term 'leaky' refers to the fact that the shell is

fluid-loaded on both the outer and inner surfaces, and therefore, energy is 'leaked' into both media rather than staying contained in the flexural wave (see Figure 3.2a). The overall scattered field intensity at different azimuthal locations is therefore obtained as a combination of the specular and flexural components. One additional point to note for completeness in the analysis of spherical shell scattering is the formation of an energetic return termed as the Mid-Frequency Enhancement (MFE). This is formed by the combination of the clockwise and anti-clockwise travelling Lamb modes in the shell. In the context of target detection, previous work [63, 64, 65] have studied this phenomenon extensively and have used it as a means of detecting submerged man-made spherical shells using acoustically beamformed MFE signatures. The MFE signature typically can be observed at mid-frequencies as the acronym suggests, corresponding to a  $ka$  of approximately 25-75 relative to the inner radius  $a$  of the shell. In the high-frequency regime, the MFE and other structural responses are significantly delayed from the dominant specular reflections due to the shell thickness as will be shown. Therefore, designing spherical or hemispherical AID tags in the high frequency regime will allow for the separation of the AID tag signature from other returns, hence allowing for AID tag detection (see Figure 3.2b). There are however certain computational challenges in simulating the analytic response of an AID tag as will be shown next, after a summary of the typical analytical formulation of the scattering from a spherical shell.

### 3.2.1 Analytical model

Derivations provided separately by Fender, Schmidt, Goodman and Stern [59, 60, 58] quantitatively describe the previously mentioned scattering mechanics, and are used to obtain the scattered pressure field of a submerged elastic spherical shell with a fluid core. This section provides a summary of the derivation provided by Goodman [58] with variable notation used in chapter 2 for the scattered field infinite plate for comparison. A polar coordinate system is used, where field points are described by  $(r, \theta, \phi)$  with  $r$  being the radial

distance,  $\theta$  being the azimuthal angle, and  $\phi$  the elevation (or commonly called declination in SONAR literature) angle. For a single shell in free space, the water halfspace, the shell layer, and the core are numbered as layers 3, 2, and 1 respectively, and the subscript  $l$  is used to indicate generalized layer-specific quantities in the derivation. Similar to the derivation of the scattered pressure computed for an infinitely long elastic plate, the displacement field  $\vec{u}$  in any of the three media can be computed from the solution to the elastic wave equation (see Equation 2.1). Assuming a time dependence of  $e^{-i\omega t}$  and decomposing the displacement field in terms of scalar and vector displacement potentials  $\phi_l(r, \theta)$  and  $\vec{\psi}_l(r, \theta)$  which satisfy the wave equations Equation 2.3 and Equation 2.4 respectively in layer  $l$ , the wave equations can be expressed in the frequency domain as

$$(\nabla^2 + k_{l,L}^2)\phi_l(r, \theta) = 0 \quad (3.1)$$

$$(\nabla^2 + k_{l,S}^2)\psi_l(r, \theta) = 0 \quad (3.2)$$

where  $k_{l,L}$  and  $k_{l,S}$  are the longitudinal and shear wave numbers for layer  $l$  defined by

$$k_{l,L}^2 = \frac{\omega^2 \rho_l}{\lambda_l + 2\mu_l} \quad (3.3)$$

$$k_{l,S}^2 = \frac{\omega^2 \rho_l}{\mu_l} \quad (3.4)$$

and obtained using the bulk acoustic velocities of a layer (see Equation 2.5). Furthermore, due to the spherical symmetry of the scattering problem, the dependence of  $\phi$  can be ignored in the solution, and the vector potential  $\vec{\psi}_l$  comprises of a single component perpendicular to the radial and azimuthal unit vectors. The scalar quantity  $\psi_l(r, \theta)$  as used in Equation 3.2 will denote this component henceforth. The key difference in the solution of the displacement fields in infinite plates and shells lies in the definition of the gradient

operator. In the polar coordinate system, the Laplacian is defined as

$$\nabla^2(r, \theta) := \frac{1}{r^2} \frac{\partial}{\partial r} r^2 \frac{\partial}{\partial r} + \frac{1}{r^2} \left( \frac{1}{\sin \theta} \frac{\partial}{\partial \theta} \sin \theta \frac{\partial}{\partial \theta} \right) \quad (3.5)$$

and upon substitution of Equation 3.5 in Equation 3.1 and Equation 3.2, the solution to the displacement potentials  $\phi_l(r, \theta)$  and  $\psi_l(r, \theta)$  are the spherical Bessel functions of the first kind (denoted by  $j_n(kr)$ ), spherical Hankel functions of the first kind (denoted by  $h_n^{(1)}(kr)$ ) and the associated Legendre polynomials of degree 0 (denoted by  $P_n(\cos \theta)$ ). The subscript  $n$  represents the order of these functions. For a layer  $l$ , the general solution for the scalar and vector displacement potential, for example, has the following modal summation structure:

$$\phi_l(r, \theta) = \sum_{n=0}^{\infty} (n + 1/2) [A_l^j(n) j_n(k_{l,L} r) + A_l^h(n) h_n^{(1)}(k_{l,L} r)] P_n(\cos \theta) \quad (3.6)$$

$$\psi_l(r, \theta) = \sum_{n=0}^{\infty} (n + 1/2) [B_l^j(n) j_n(k_{l,S} r) + B_l^h(n) h_n^{(1)}(k_{l,S} r)] P_n^1(\cos \theta) \quad (3.7)$$

where the weights  $A_l^j(n)$ ,  $A_l^h(n)$ ,  $B_l^j(n)$ , and  $B_l^h(n)$  are to be determined for each layer and order based on the boundary conditions imposed. Here, the spherical Bessel function represents an incoming wave (travelling left to right), and the spherical Hankel function of the first kind an outgoing wave (travelling from right to left). In the most general case, an elastic layer can have four waves - namely a pair of incoming and outgoing longitudinal and shear waves. Simplifications can be made based on the materials of each media.

In the water halfspace for example, an incident monochromatic plane wave (arriving from  $\theta = \pi$ ) can be represented by

$$\phi_{inc}(r, \theta) = \sum_{n=0}^{\infty} (n + 1/2) [(2 \cdot i^n) j_n(k_{3,L} r)] P_n(\cos \theta) \quad (3.8)$$

where only the term for the spherical Bessel function is used, with the weights computed as in Morse and Ingard [66]. The scattered field in a similar fashion can be expressed purely



in terms of a spherical Hankel function of the first kind as

$$\phi_{scat}(r, \theta) = \sum_{n=0}^{\infty} (n + 1/2) [A_3^h(n) h_n^{(1)}(k_{3,L} r)] P_n(\cos \theta) \quad (3.9)$$

where the weights  $A_3^h(n)$  as computed from the boundary conditions describe the full scattered field.

The boundary conditions to be enforced at the halfspace-shell and shell-core interfaces are the continuity of radial displacement, radial stress, and vanishing shear stress (as both the halfspace and core are taken to be fluids here). A system of equations matching the the displacement and stress field quantities of the layers at each interface can be assembled similar in structure to the global matrix formulation and can be solved simultaneously to obtain  $A_3^h(n)$ . The computation can be repeated over a frequency range to obtain the frequency response of the shell. A full derivation of the computation of the displacement and stress terms is provided in Appendix A.

For monostatic scattering applications, the backscatter from the spherical shell along ( $\theta = \pi$ ) is of interest. As an example, the backscattering from an air filled steel shell with an outer radius of 53 cm and a shell thickness of 2.6 cm immersed in water is presented. The shell is insonified by a Gaussian pulse centered at 25 kHz with a fractional bandwidth of 0.3, and the backscatter computed at a radial distance of 10 m. The material properties used for the various media in the simulation are listed in Appendix B.

Figure 3.3a shows the computed backscattering spectrum for the shell and the source signal used. The simulation closely follows the results developed by [55], and is used to demonstrate the solution to the analytic shell scattering formulation and establish a baseline before high frequency calculations are run. The backscattering spectrum is computed up to a  $ka$  range of 100, using  $n = 100$  modes in the modal summation. Convergence tests to determine the modal truncation are reported in Anderson [55]. The time domain response of the source signal convolved with the shell impulse response is shown in Figure 3.3b, and indicates the specular return from the shell, the MFE return, and the subsequent Lamb

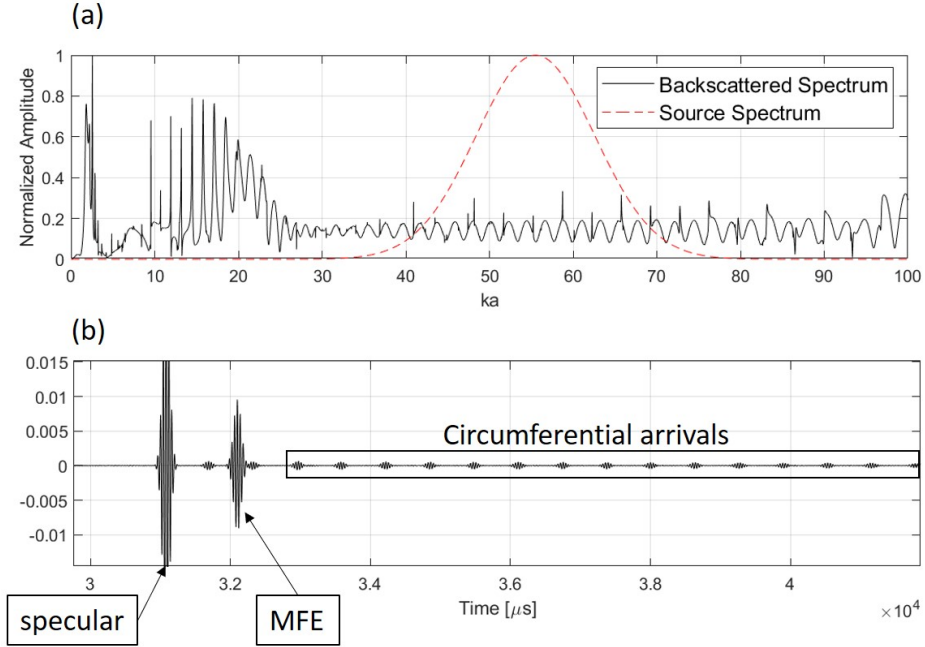


Figure 3.3: (a) The backscattered spectrum from a air filled steel shell submerged in water, alongwith the source spectrum used to generate the time domain response of the backscatter from the shell. Here,  $ka \sim 50$  corresponds to approximately 25 kHz. Both the backscatter spectrum and source spectrum are normalized for better visualization. (b) The temporal response of the backscatter from the steel shell, with the specular, MFE, and later structural arrivals indicated.

wave arrivals.

However, when performing the same computation for shell scattering in the high  $ka$  regime to compute the backscatter for a high frequency SONAR source (in this case on the order of  $ka \sim 2000$  for a 500 kHz source) in addition to numerically unstable results, the minimum number of modes required to simulate the backscatter is very high [67]. This makes the simulation computationally very expensive relative to the computations performed at the mid-frequency range.

As shown in the time domain response of the scattering of a 500 kHz wideband Gaussian source (see Figure 3.4b), the specular reflections from the thickness of the steel shell are accurately computed. However, the results are acausal, and the arrivals around the  $1.105 \times 10^4 \mu s$  mark are numerical artefacts from the modal summation. These are challenges presented at the single shell level and are exacerbated in multishell settings. This

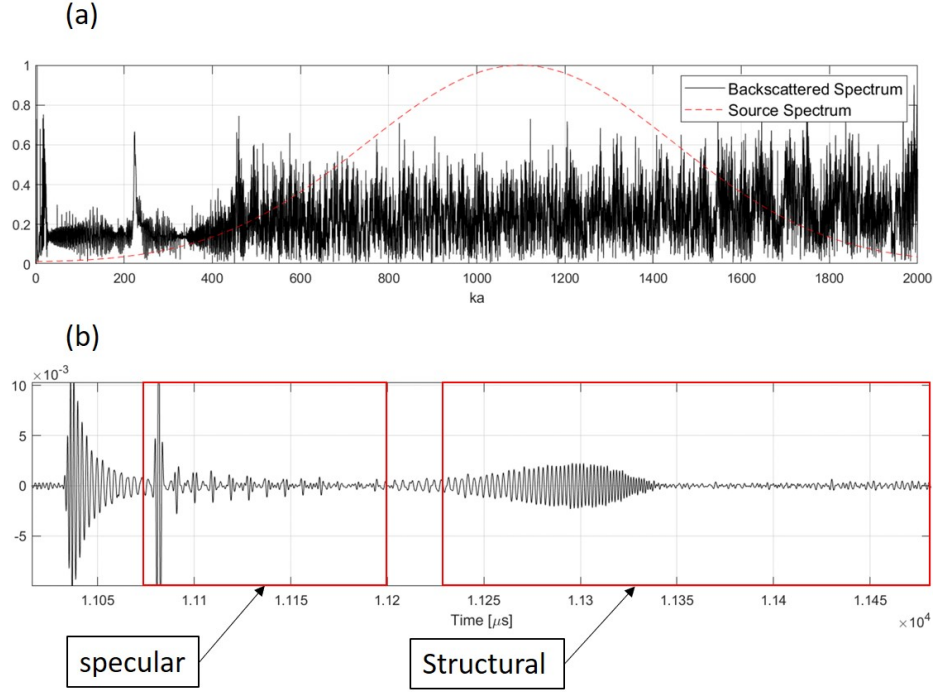


Figure 3.4: (a) The backscattered spectrum from the same air filled steel shell submerged in water as in Figure 3.3, computed now for a high frequency source, whose spectrum is marked in red. Here,  $ka \sim 2000$  corresponds to approximately 500 kHz in water. (b) The temporal response of the shell backscatter. The specular component is preceded by numerical noise, and the structural response is marked as arriving after the specular response.

presents the need to find more efficient methods of predicting the backscatter from a multilayered AID tag in the high frequency regime.

### 3.3 Modelling high frequency scattering from spherically layered AID tags

As discussed in the previous section, standard numerical models are computationally challenging to use to simulate the scattering from shells when the wavelength is much smaller than the radius of the shell. It is however in this range that AID tags with spherical symmetry seek to operate, as the backscattered response would hypothetically contain a dominant specular return due to the layering of the shells in the tag, while clearly separating other structural responses. In order to effectively predict the scattered response from AID tags with curved symmetry interrogated at high frequencies, it is therefore important to under-

stand the frameworks available for different scattering regimes. In literature [68], acoustic scattering is divided into three different regimes - the Rayleigh (or low  $ka$ ) regime where the scatterer is much smaller than the incident wavelength, the Mie or transitional regime when the nominal scatterer dimension (the inner radius of the elastic spherical shell in the current case) is comparable to the incident wavelength, and the geometric (or high  $ka$ ) regime where the nominal scatterer dimension is several wavelengths in size. Rayleigh scattering typically refers to the scattering of small particles and targets, whose scattering behaviour is therefore close to that of a monopole, and problems can be simplified accordingly. Scattering problems in the Mie and geometric acoustics regimes can be solved using analytic methods, finite and boundary element methods, spectral methods, ray tracing, and space-time marching schemes.

### 3.3.1 Setting up the AID tag simulation environment in k-Wave

It has been possible to simulate the scattered field from spherically symmetric, multi-layer AID tags designed for high frequency sources using a Pseudo Spectral Time Domain (PSTD) based elastic wave propagation solver from the open source k-Wave toolbox [69, 47] for Matlab. The solver accepts a discretized density map, discretized longitudinal and shear velocity maps, a (possibly time-varying) source pressure distribution (see Figure 3.5) and binary masks of the source location at which the pressure distribution is applied and virtual sensor locations from which simulation outputs are sampled.

The scattering from two types of AID tags - with fully spherical and hemispherical layers as in Figure 3.6(a-c) - in free space have been simulated in this study. The full sphere simulation (Figure 3.6(a)) is conducted to establish a baseline for the large  $ka$  scattering from a regular shape and demonstrate the separation of specular components from other structural returns. Using the same tag layering structure and sizing as in the full sphere case, with the addition of a 2 mm thick acrylic mounting plate, a hemispherically stratified AID tag is simulated for a source pulse incident at  $\theta = 0^\circ$  (Figure 3.6b) to demonstrate

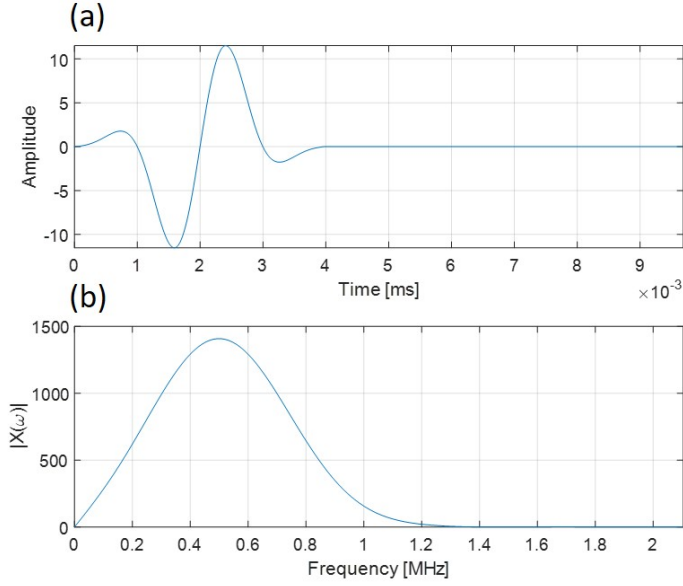


Figure 3.5: (a) Wideband 500 kHz Gaussian pulse used as source signal for k-Wave simulation. (b) Magnitude spectrum of (a)

the similarity in backscattered field from the spherical, and hemispherical tag. An additional simulation of an offset source ( $\theta \neq 0$ ) is run (Figure 3.6c) to verify that the scattered response from a hemispherically stratified tag is azimuthally invariant. No additional simulation is necessary for spherical tags due to symmetry.

The AID tags used here have the optimal design in terms of reflected signal energy, as will be discussed in more detail in chapter 4. Both the spherical and hemispherical AID tags defined for the simulation are made of four concentrically placed acrylic shells that are 2 mm thick, and an innermost, 2 mm thick spherical or hemispherical shale shell. The shells enclose four water layers of varying thicknesses. The individual layers and their dimensions are provided in Table 3.1. It is to be noted that the innermost shale layer is provided a radius of 3in (7.62 cm), and all other layer radii are increased accordingly by their thickness to form the concentrically layered tag. This shell sizing places the scattering from the AID tag in the geometric acoustics regime when a wideband 180 dB SPL explosive Gaussian source pulse centered at 500 kHz is used as the source signal. Here,  $ka$  for the AID tag found to be 160.

Table 3.1: Layer thicknesses for the four water-layer AID tag used in k-Wave and global matrix simulations. Here, layer 1 represents the top water halfspace, and layer 11 represents the bottom halfspace.

#	Layer Name	Layer Thickness [m]
1	Water	N/A
2	Acrylic	$2 \times 10^{-3}$
3	Water	$1.13 \times 10^{-2}$
4	Acrylic	$2 \times 10^{-3}$
5	Water	$1.04 \times 10^{-2}$
6	Acrylic	$2 \times 10^{-3}$
7	Water	$0.95 \times 10^{-2}$
8	Acrylic	$2 \times 10^{-3}$
9	Water	$0.87 \times 10^{-2}$
10	Shale	$2 \times 10^{-3}$
11	Water	N/A

As will be discussed in chapter 4, setting the innermost shell of an AID tag to a highly reflective material boosts the reflected response from the tag. While a metal such as aluminum or steel would be the ideal choice in actual manufacturing, the elastic solver in k-Wave offers solution accuracy only for weakly heterogeneous media (or limited impedance mismatch) [70], therefore shale is set as a reasonable proxy.

In the simulation environment, the point source signal (Figure 3.5a) is transmitted from the marked white points in Figure 3.6(a-c) which are all approximately  $20\lambda$  from the outermost shell of the tag, where  $\lambda$  is the wavelength of the center frequency of the source signal. An omnidirectional source is used here rather than a plane wave to serve as a baseline for simulations of AID tags near an interferer which will be discussed in chapter 5. The acoustic pressure is recorded along the solid white line connecting the source location to the center of each tag (see Figure 3.6) to represent the signal collected by monostatic systems. The total simulation time is set to 0.25 ms, so that all the interfacial reflections from each tag is captured at the transmit location.

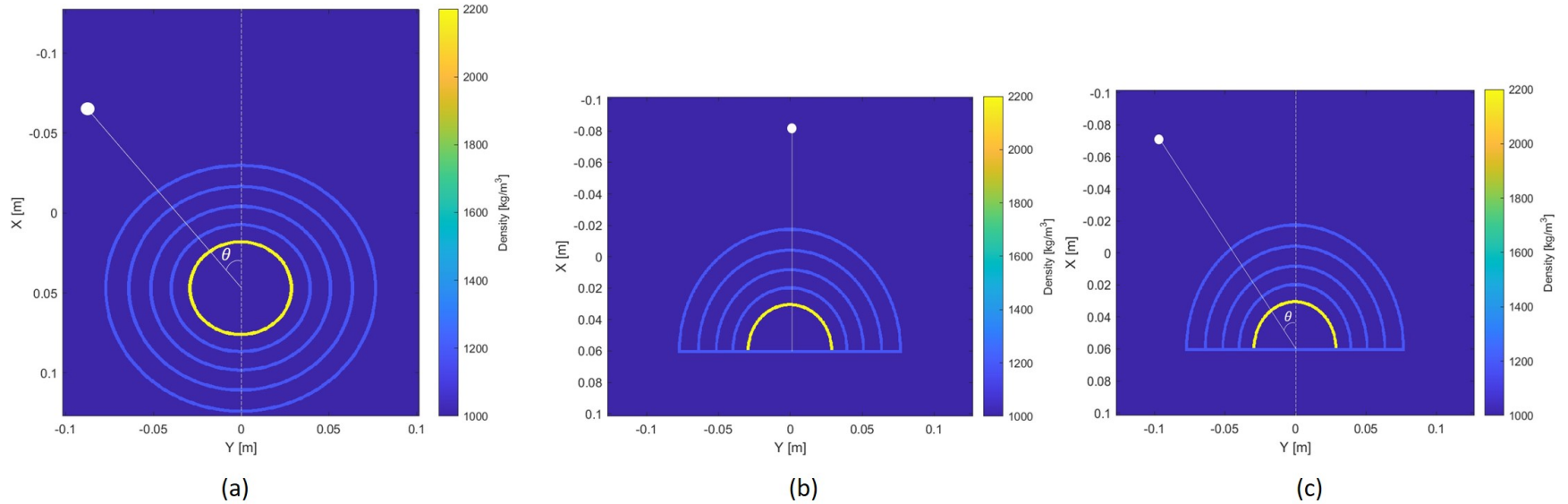


Figure 3.6: (a) Density map for a spherical tag immersed in water. The white circle indicates the source location, making an angle  $\theta$  to the indicated normal (dotted line). The light blue regions correspond to the acrylic shells and plate, the yellow region the shale layer, and the dark blue the water. (b), (c) Density maps for the hemispherically stratified AID tag immersed in water. (b) places an explosive point source to be normally incident to the AID tag i.e.  $\theta = 0^\circ$  while (c) uses a source offset from the center of the tag i.e. at an angle  $\theta$  as indicated. In (a), (b) and (c), the solid line connecting the center of the tag to the source represents the line of virtual sensor locations at which field measurements are taken.

It must be emphasized that the spatial discretization of the solution domain must support the source frequencies being used. As k-Wave computes portions of the solution in wavenumber space, the scattered field output is particularly sensitive to the sampling of grid points over the domain of interest. This can be computationally and memory intensive when simulating large domains with high frequency sources and therefore care must be taken in defining the domain and grid step sizes. A good rule of thumb for the spatial discretization of the grid is to set the stepsize  $\Delta x$  to at most  $\lambda_{min}/5$  so that 5 grid points cover one wavelength of the highest frequency propagating in the simulation. Ideally, 10 grid points per wavelength are preferred.

Furthermore, the discretization of the numerical grid makes use of the Courant-Friedrichs-Lewy (CFL) condition which specifies the permissible numerical time step  $\Delta t$  allowed for a spatial discretization of  $\Delta x$  to ensure solution stability. If the time step is too large, the difference equations being solved will not converge and is unstable. The opposing problem where the time step is too small leads to increased computational expense. Formally, the CFL condition used in k-Wave is defined as the ratio of the distance a wave can travel in one time-step to the grid spacing i.e.

$$CFL = c_{max} \cdot \frac{\Delta t}{\Delta x} \quad (3.10)$$

where  $c_{max}$  is the largest velocity value in the acoustic velocity map supplied to the solver. The time step can be readily defined using the grid spacing,  $c_{max}$  and a user specified CFL number as

$$\Delta t = CFL \cdot \frac{\Delta x}{c_{max}} \quad (3.11)$$

A CFL number of 0.1 offers the most stability, but also decreases the timestep, which increases computational time. This can be relaxed to 0.3 for large problems or for problems with weakly heterogeneous media. In the case of simulating an AID tag, a CFL number of



0.15 - 0.2 has been used to ensure that the solution can handle the acoustically dissimilar materials composing the the AID tag.

In order to simulate the fact that the AID tags are in free-space, a Perfectly Matched Layer (PML) of 30 grid points on all sides of the domain is used. The PML serves as an absorptive layer that attenuates any waves incident on the domain boundaries, and is well documented in computational physics literature [71].

### 3.3.2 k-Wave simulation results and the flat plate approximation

Time histories are collected along the line of virtual sensors of the k-Wave simulation for the spherical and hemispherical shells, and are shown in Figure 3.7(a-c). Here, the time-histories from each sensor is stacked one on top of the other to generate the composite images shown. The sensors are numbered such that sensor number 1 (top row of each plot) corresponds to the source location, and the sensor number increases along the line connecting the source and the center of the AID tag. Each row in Figure 3.7 represents the normalized pressure at the sensor number indicated. As is evident from Figure 3.7(a-c), the propagating incident pulse is recorded along the line of sensors, before it makes contact with the AID tag (the first inflection in the figures) where some energy is reflected back, and some transmitted through to the secondary layers. Each inflection point in the images therefore represents an interfacial reflection (similar to the reflection plots shown in Figure 2.4 and Figure 2.5), and the signal collected at the source location over the entire duration of the simulation is extracted from sensor 1 in all three cases.

Furthermore, to qualitatively compare the AID tag signatures scattered back towards the source location in each of the three cases presented in Figure 3.7, time histories are sampled at three arbitrarily selected sensor locations in the water halfspace and plotted in Figure 3.8(a-c).

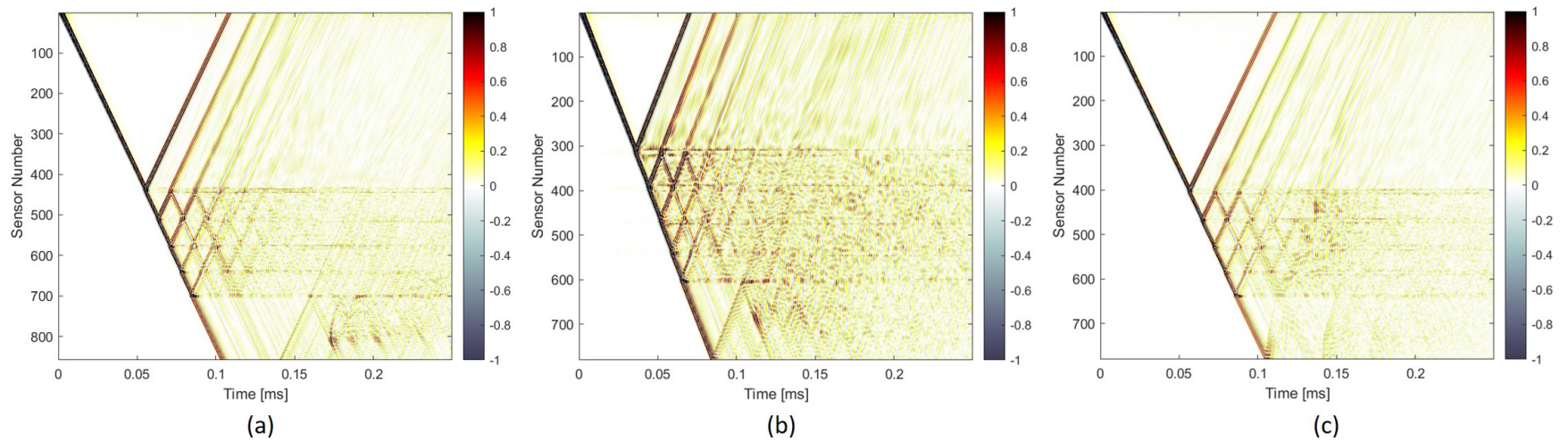


Figure 3.7: (a) Time-histories recorded along the sensor line (solid white line) shown in Figure 3.6a for the spherically stratified tag. (b) Time-histories recorded along the sensor line (solid white line) shown in Figure 3.6b for the hemispherically stratified tag, for a source incident from  $\theta = 0^\circ$  (c) Time-histories recorded along the sensor line (solid white line) shown in Figure 3.6c for the hemispherically stratified tag with an offset source signal ( $\theta \neq 0^\circ$ ).

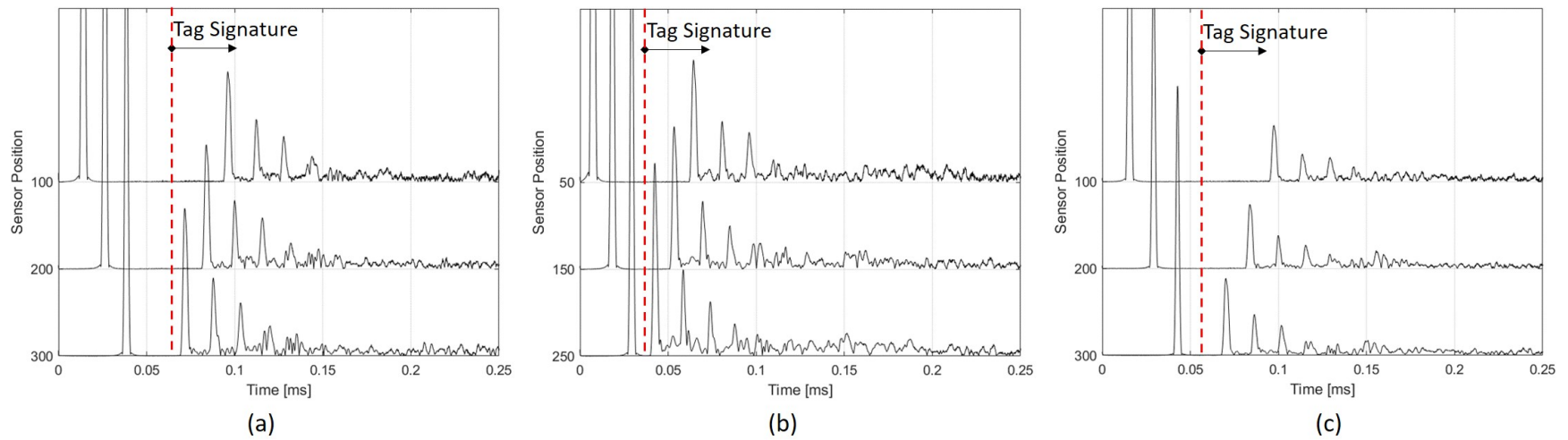


Figure 3.8: (a) Time-histories recorded at the 100th, 200th, and 300th sensor of Figure 3.7a. The signal after 0.05 ms corresponds to the backscatter from the AID tag. (b) Time-histories recorded at the 50th, 150th, and 250th sensor of Figure 3.7b. The signal after  $\sim 0.04$  ms corresponds to the backscatter from the AID tag. (c) Time-histories recorded at the 100th, 200th, and 300th sensor of Figure 3.7c. The signal after 0.05 ms corresponds to the backscatter from the AID tag.

In order to verify the claim that a spherically (or hemispherically) stratified AID tag produces the same backscattered signature as an AID tag made of flat plates, the results obtained from the top sensor of the three k-Wave simulations are compared with the AID tag response simulated for an equivalent flat layer stratification using the global matrix solution, and layer structure given in Table 3.1. Here, the same source signal transmitted in the k-Wave simulation (see Figure 3.5a) is used to obtain the flat-plate AID tag signature which is shown in Figure 3.9.

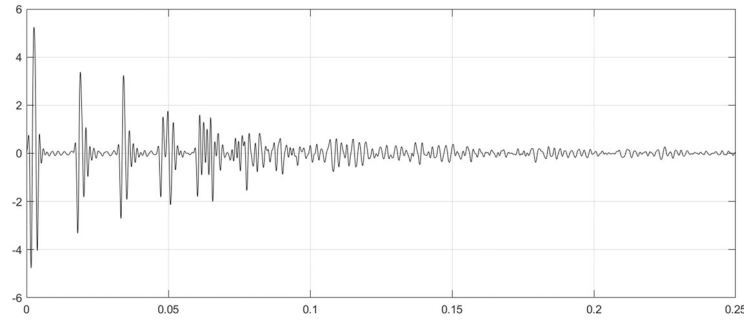


Figure 3.9: The backscattered response from a flat-plate AID tag simulated using the Global Matrix Method, using the same layer materials and thicknesses as in the spherical or hemispherical AID tag k-Wave simulation.

The time-histories from the k-Wave results are cross-correlated and aligned with the Global Matrix Method (GMM) solution, and plotted in Figure 3.10(a-c). It is to be noted that the GMM solution used is truncated to 0.06 ms in Figure 3.9, therefore enforcing the correlation of only the dominant features of the AID tag signature. Panel (a) corresponds to the spherically stratified tag simulation, panel (b) corresponds to the hemispherically stratified tag with the source incident at  $\theta = 0^\circ$ , and finally panel (c) corresponds to the hemispherical AID tag, with an offset source. All three k-Wave simulation outputs align well with the simulated global matrix solution, with the spherical tag and hemispherical tag at  $\theta = 0^\circ$  incidence simulations having a 86% correlation with the global matrix solution, while the hemispherical tag with an offset source correlating with the GMM solution by 78%. These correlation coefficients are also marked in Figure 3.10 for reference. As demonstrated, it is possible to approximate the scattered field from AID tags with shell

stratification to the global matrix solution in the 'geometric acoustics' or high  $ka$  limit.

It is to be noted from this study that the hemispherical AID tag response to an offset source (see Figure 3.6c) correlates less than the spherical and source at  $\theta = 0^\circ$  cases. This is attributed to some signal interference arising from the bottom left corner of the hemispherical tag and mounting plate. While the main specular reflection from the tag arrives before the interfering signal, some of the later details of the tag signature is mixed with this interfering signal, reducing the correlation with the flat plate solution. In the k-Wave simulation, this interference can be easily remedied by increasing the minimum diameter used in the AID tag so that the corner contribution from the tag arrives well separated from the specular component. As another option, an acoustically absorptive coating can be applied to the mounting plate used to affix the hemispherical shells, to minimize the strength of the interfering signal. These simulations have not been conducted however, since the primary objective was to demonstrate that the acoustic signatures from AID tags with spherical symmetry can be approximated by the signature generated by an equivalent horizontally stratified AID tag.

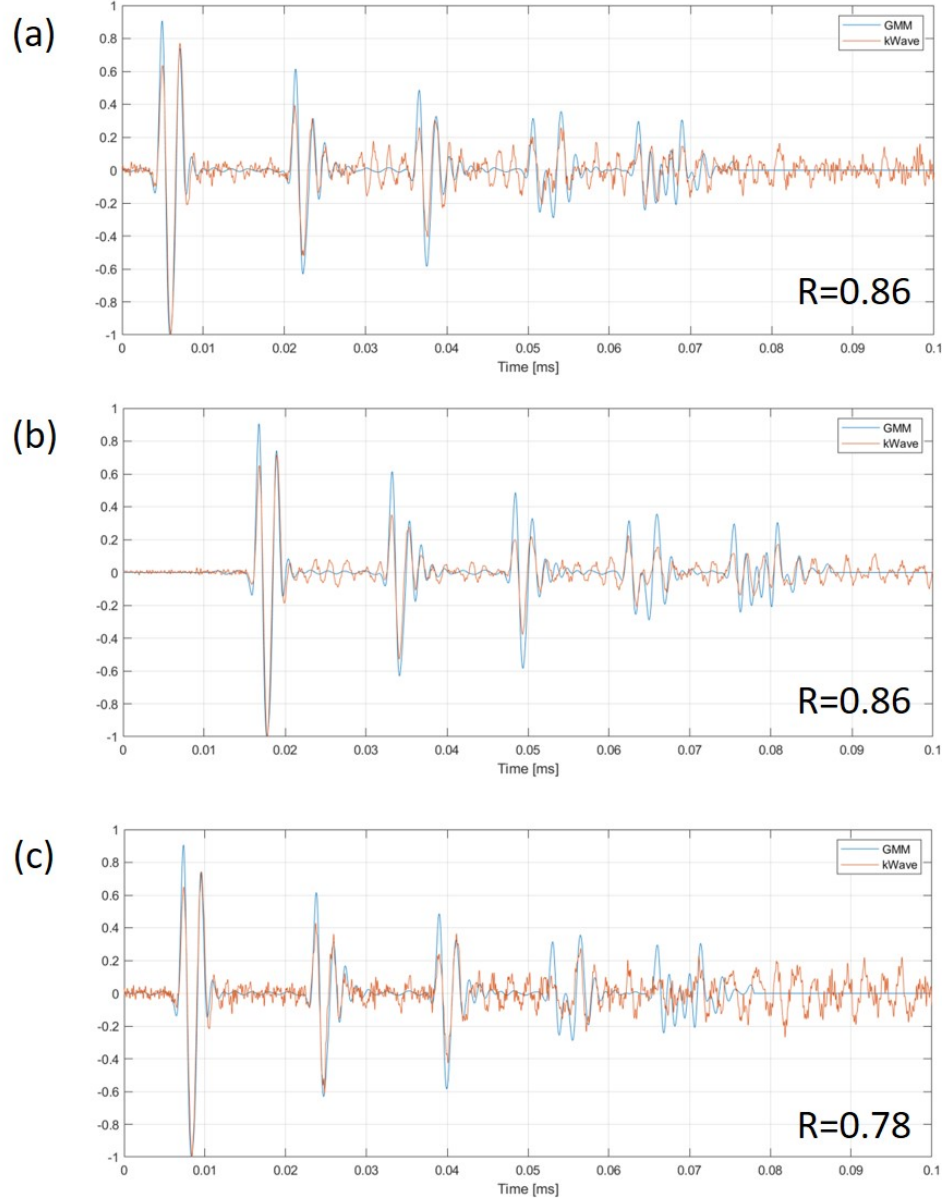


Figure 3.10: k-Wave obtained scattered field responses compared to equivalent global matrix solution for (a) Spherically stratified AID tag (b) Hemispherically stratified AID tag with source incident from  $\theta = 0^\circ$  (c) Hemispherically stratified AID tag with source at  $\theta \neq 0$ .

### 3.4 Experimental testing of hemispherically stratified AID Tags

With confirmation from simulations that it is possible to obtain AID tag signatures from stratified shells as described in section 3.3, a prototypical AID tag made of two 3D printed resin shells was manufactured and tested using the same sub-scale ultrasound setup described in section 2.4 [54].

#### 3.4.1 Experiment Setup and shell fabrication

Hemispherical shells with radii on the order of 40 mm were insonified with an ultrasonic Gaussian modulated pulse centered at 6 MHz with a full width half maximum bandwidth of 4MHz (corresponding to a minimum  $kR = 580$  in water) using the Ultrasonix L14-5/38 Linear Transducer (see section 2.4). While hemispherical shells were chosen in this study for ease of manufacturing and testing, their scattered response is also representative of scattering from a spherical shell due to symmetry (also as demonstrated from the k-Wave simulations). The hemispherical shells were manufactured by SLA using a Formlabs(Somerville, MA) Form2 printer hosted by the Invention Studio at Georgia Tech [72]. The outer and inner shells were fabricated using Formlabs proprietary UV curable “Clear” and “Tough” resins respectively. The SLA printing technique was selected so that the material properties of the printed shells are nearly homogeneous and isotropic. Maintaining constant bulk acoustic properties over the volume of the shells was critical in obtaining a spatially invariant backscattered response.

More specifically, two 2 mm thick shells were printed - an outer shell made of Clear resin with an outer radius of 40 mm, and an inner shell of Tough resin with an outer radius of 37 mm (see Figure 3.11(a-e)). The prototype AID tag was constructed by concentrically affixing both shells to an aluminum backing plate. The dimensions selected allow for water ingress into a 1 mm thick gap between the shells when the tag is immersed in water. The intermediate fluid layer acts as an acoustic couplant between the two solid shells.

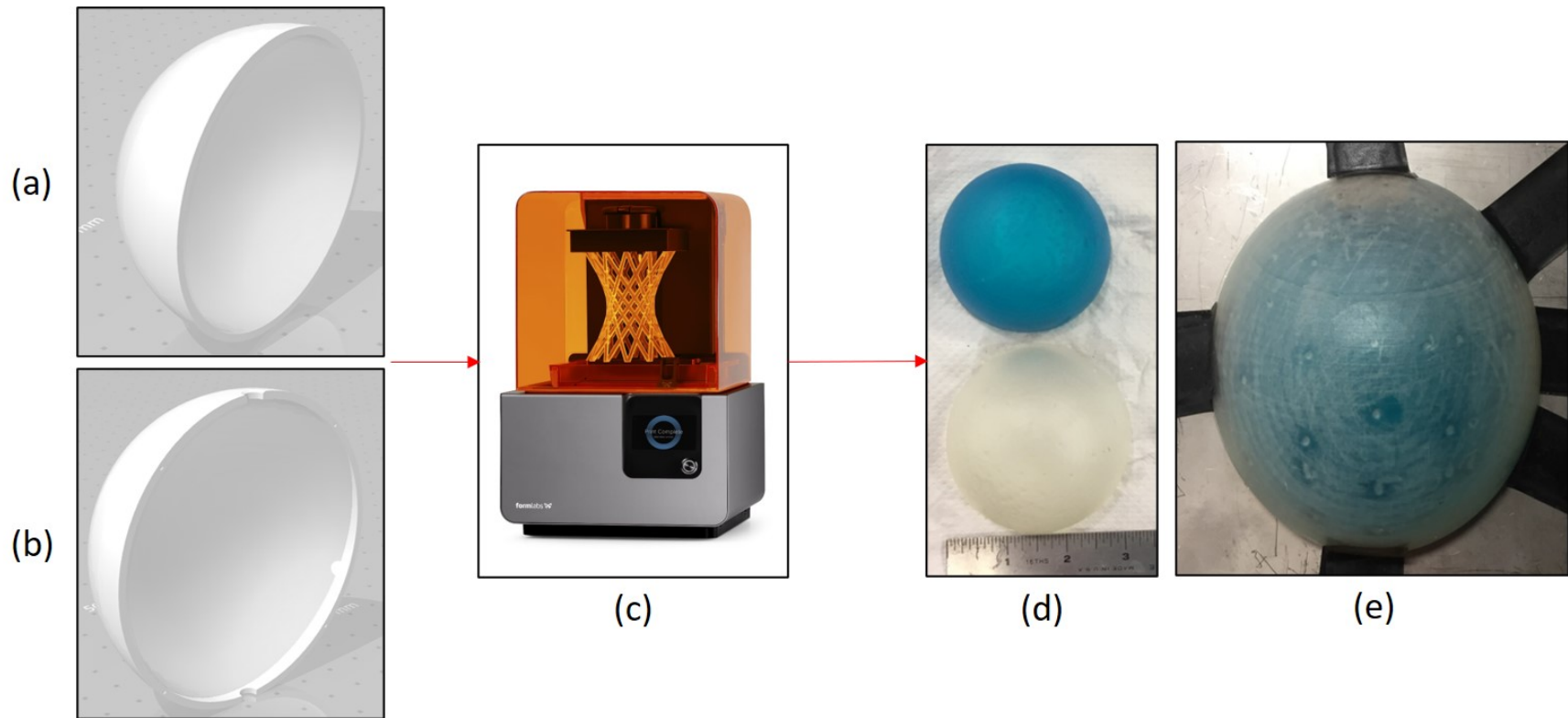


Figure 3.11: (a, b) Computer Aided Design (CAD) models of the inner (a) and outer (b) hemisphere, made of Formlabs "Clear" and "Tough" resins respectively. Both hemispheres are 2 mm thick, with outer diameters of 40 mm and 37 mm respectively. (c) The Formlabs Form 2 printer. (d) The printed hemispherical shells before assembly into an AID tag, where the blue hemisphere is the inner shell made of "Tough" resin, while the outer shell is made of "Clear" resin. (e) The fully assembled two-shell AID tag, with the hemispheres mounted on a 3 mm thick aluminum backing plate.



The ultrasonic transducer was maintained at 75 mm (i.e. approximately 290 wavelengths of the center transmit frequency in water) away from the test specimen in a water bath (see Figure 3.12(a, b)).

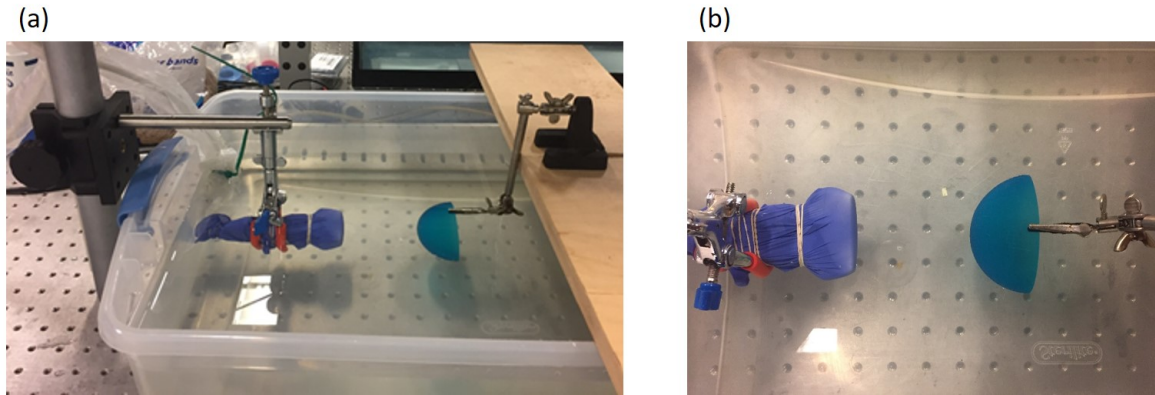


Figure 3.12: (a) Sideview of the "Tough" hemispherical shell placed near the ultrasound probe. (b) Top view of the same setup. The spacing between each grid point is 1in.

Prior to measuring the backscattered response from a layered acoustic tag, the compressional velocity and attenuation coefficient of the Clear and Tough resins were first characterized individually to provide the required input material parameters for the numerical predictions of the AID's backscattered responses. To do so, assuming locally normal incidence at high  $kR$ , the backwall reflections from individual hemispherical samples of a known thickness of 2 mm (see Figure 3.11d) were used as shown in Figure 3.13. The estimation method used is identical to the discussion in section 3.4

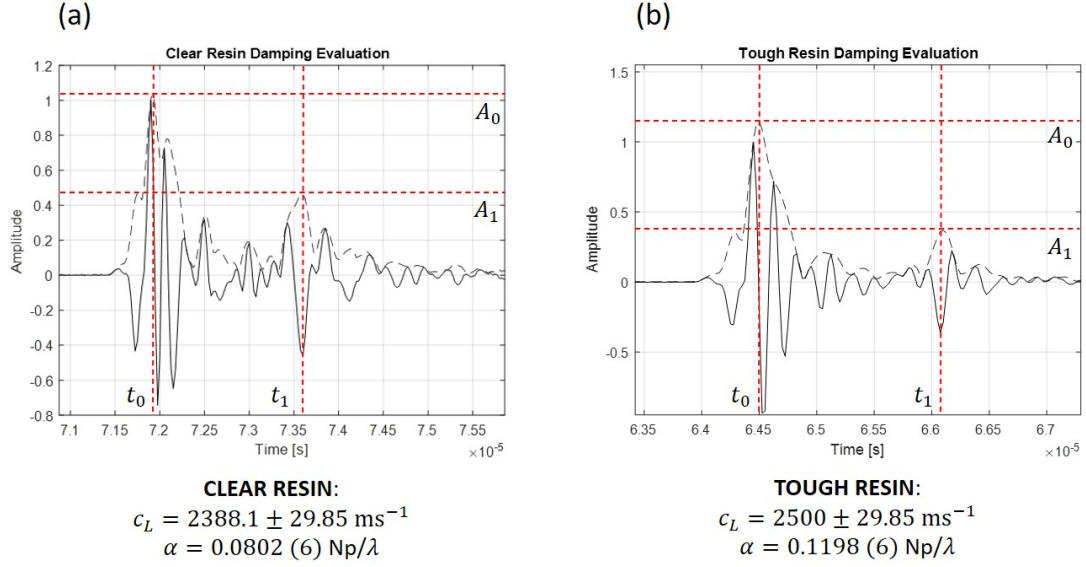


Figure 3.13: (a) Acoustic property estimation from the backwall scattering from the Clear resin shell (b) Acoustic property estimation from the backwall scattering from the Tough resin shell

Subsequently, the same setup shown in Figure 3.12, was used to obtain backscatter measurements for the two-layered hemispherical AID tag over a range of azimuthal angles in increments of  $10^\circ$  starting from  $\theta = 0^\circ$  as marked in Figure 3.14a. In addition to obtaining the AID tag's signature, the measurements from varying azimuth examines the spatial dependence of the scattered response as demonstrated in the subsequent section.

### 3.4.2 Hemispherical AID tag response measurements

Figure 3.15 displays the full acoustic response of the two-layered hemispherical AID tag shown in Figure 3.14 for a transducer at  $\theta = 0^\circ$  incidence. As hypothesized in section 3.3, in the high  $kR$  regime, Figure 3.15 experimentally confirms that the specular echoes generated by the multiple reflections from two hemispherical layers are time gated from successive reflections associated with the shell's structural response and reflections from the aluminum backing plate.

Furthermore, as expected, results shown in Figure 3.16 confirm that the specular component of the backscattered response of the two-layered hemispherical AID tag is inde-

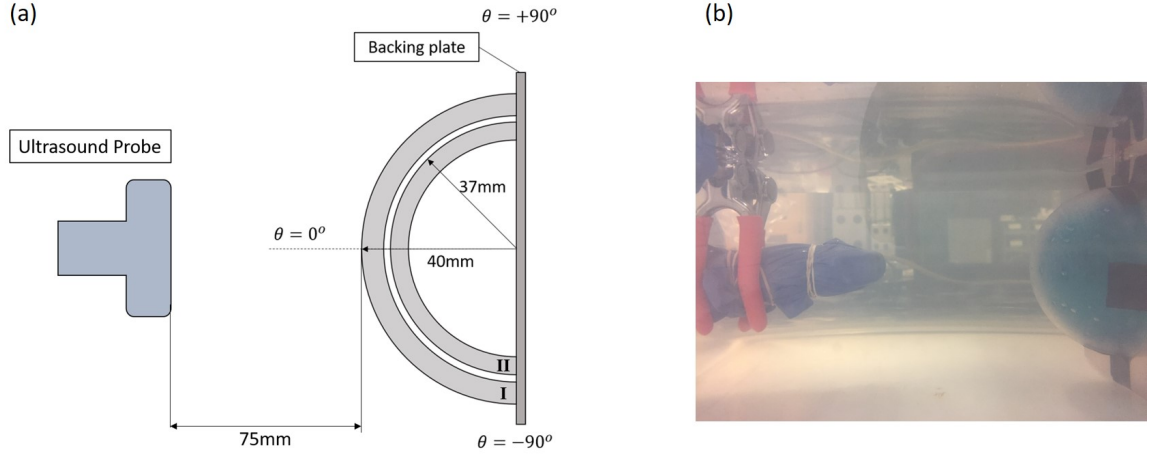


Figure 3.14: (a) Schematic of the experimental set-up, testing the assembled two-shell AID tag. Shell I is printed out of Clear resin, while shell II is printed out of Tough resin. The inter-shell space is filled with water acting as an acoustic couplant. The entire setup is immersed in a water bath. The convention for measured azimuthal angle is also marked. (b) Close up of the AID tag being tested.

pendent of the incidence orientation (up to manual positioning error) for the monostatic configuration of the ultrasonic probe.

Finally, the experimentally obtained measurements for  $0^\circ$  incidence on the single hemisphere (Figure 3.17a) and two-layered hemispherical AID tag (Figure 3.17b) are compared to the simulated waveform using the numerical model for horizontally stratified media mentioned in section 2.2. The acoustic parameters obtained experimentally for the Clear (white, outer shell) and Tough (blue, inner shell) resins (Figure 3.13a and Figure 3.13b) were used for the simulation.

The transmitted signal from the ultrasound probe used for the simulations was based on the estimated transmitted waveform separately isolated from the reflection off a single flat metal plate, although the default pulse as in section 2.4 can also be used to obtain similar results. The normalized cross-correlation coefficients between the simulated and measured acoustic signatures were high (0.94 for the single shell and 0.95 for the two-layered hemispherical AID tag) thus confirming that the simple numerical model for horizontally stratified media is suitable to predict the portion of the spherical AID tag's signature correspond-

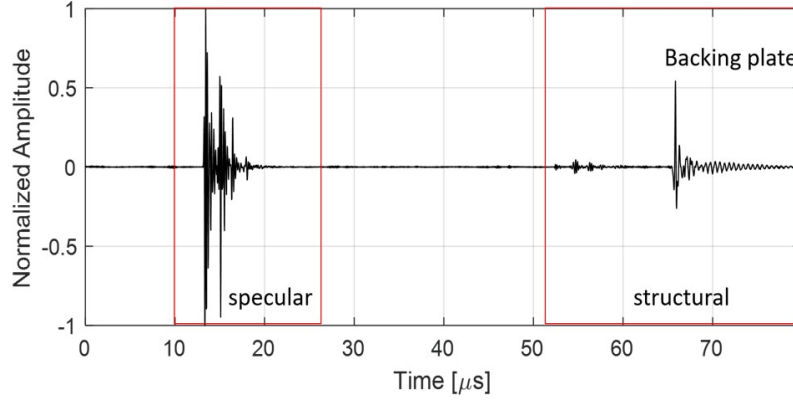


Figure 3.15: The full scattered response from the two-shell hemispherical AID tag tested using the ultrasound setup. The first red box indicates the specular component of the scattered field, while the second red box demarcates the late structural arrivals from possible guided waves and the aluminum backing plate.

ing to the specular reflection, provided accurate material properties and layer thicknesses of each layer of the AID tag.

The obtained experimental results are a proof of concept that stratified shells may be deployed as AID tags, and can serve as acoustic markers or acoustic bar-codes that reflect detectable acoustic signatures in underwater sensing applications. Furthermore, having experimentally validated that AID tags with spherical symmetry can be modelled and fabricated successfully for the ultrasonic regime, it is straightforward to extend the tag design to operate in the high frequency SONAR regime. Typical imaging SONARs such as the Starfish 452F by Tritech have transmit frequencies in the range of  $\sim 100$  kHz, so a minimum shell radius  $R$  can be computed using the high  $kR$  approximation. More generally, tag dimensions for any frequency range of interest can be specified using the proposed methodology once the material properties and thicknesses of each layers are suitably selected.

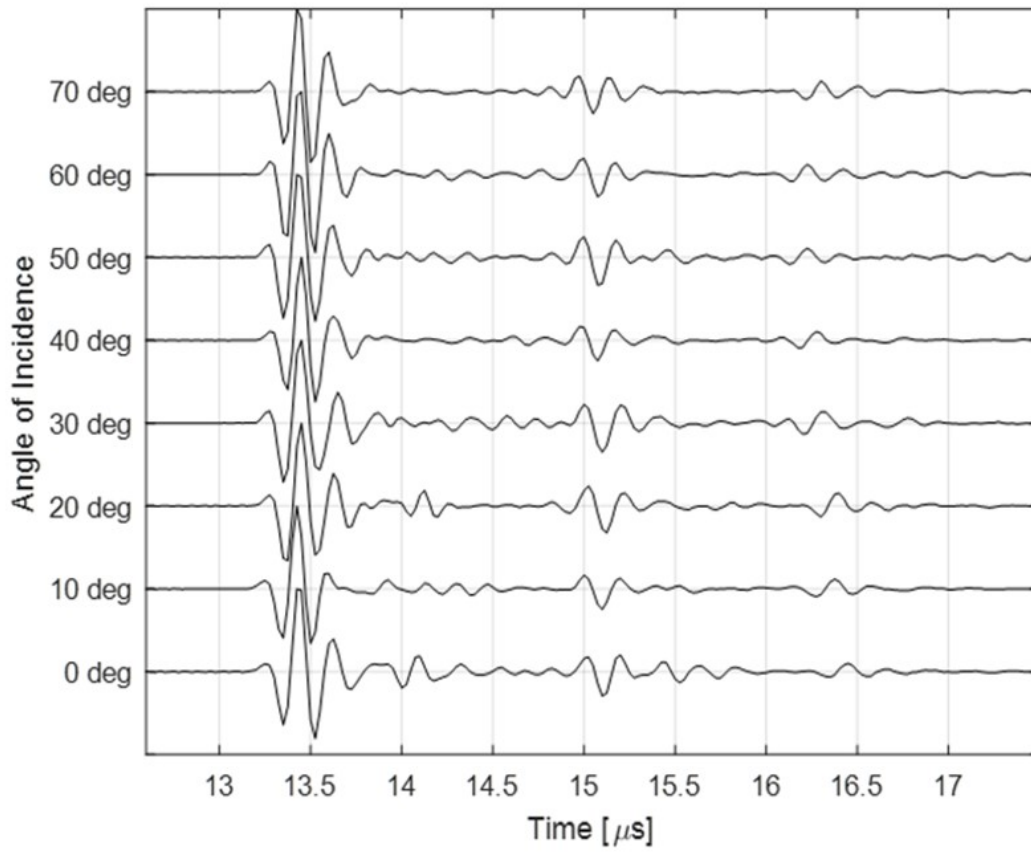


Figure 3.16: Backscattered responses collected over varying azimuthal incidence angles from  $\theta = 0^\circ$  to  $\theta = 70^\circ$  as marked.

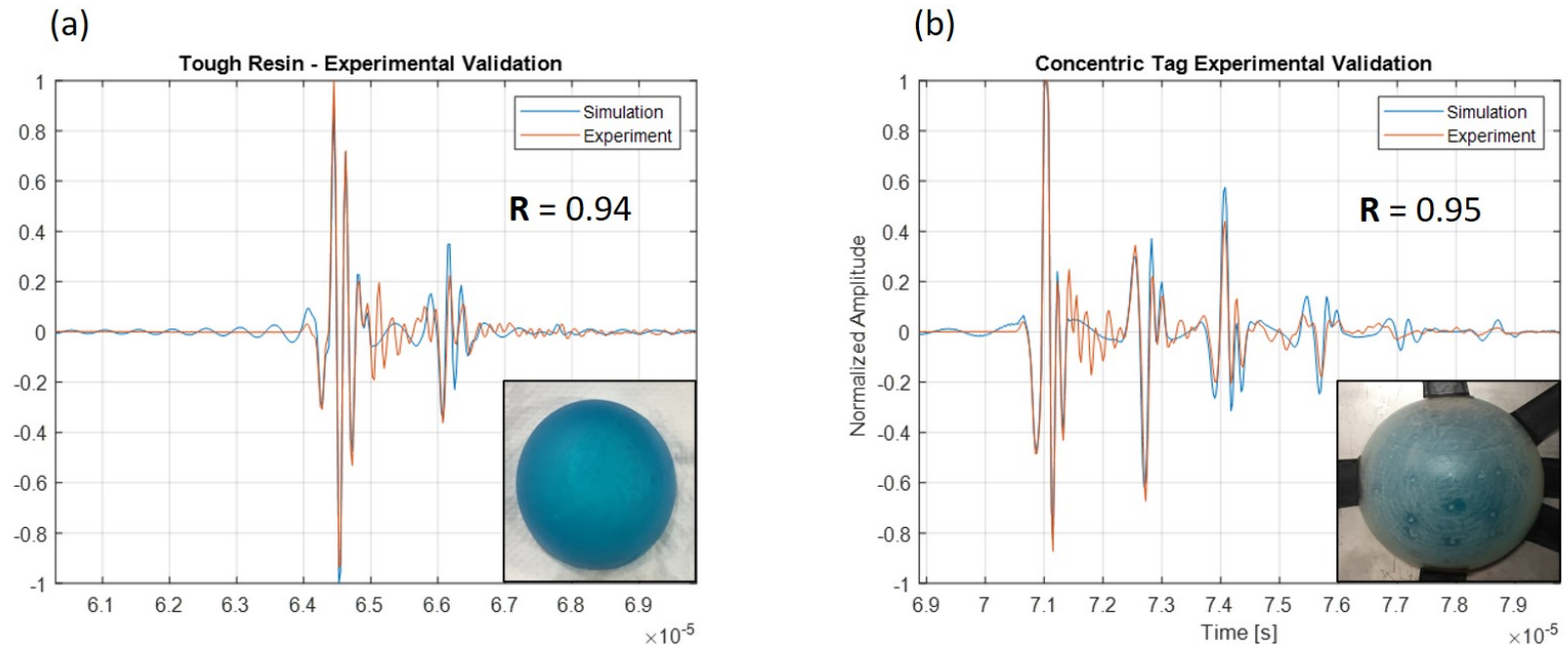


Figure 3.17: Comparison of the simulated waveforms (using the acoustic parameters listed in Figure 3.13a and Figure 3.13b) and experimentally measured waveform for a) a single Tough resin hemispherical shell and b) the two-layer AID tag. Correlation coefficient  $R$  between the two waveforms are also indicated

### 3.5 Chapter Summary

This chapter proposed a curved or spherically symmetric AID tag design comprised of concentric shells of different acoustic materials, so that the backscatter from the AID tag is omnidirectional. Furthermore, it was demonstrated that in the high frequency scattering limit, the specular response from the AID tag can be approximated by the response from an equivalent horizontal stratification, and the structural arrivals from the AID tag are well separated from the specular components. The backscattered response from a hemispherically stratified AID tag built of SLA manufactured shells was experimentally measured, and shown to be in close agreement with the corresponding simulated response. The material properties of the resin used to manufacture the shells were experimentally determined. Finally, the omnidirectional nature of fabricated AID tag was experimentally verified.

## **CHAPTER 4**

### **TAG DESIGN OPTIMIZATION**

#### **4.1 Tag Design Criteria**

As discussed in chapter 2, the reflected response from a passive AID tag is a function of the material of each tag layer, and the corresponding layer thickness (see Figure 2.1). While the selection of these parameters in tag design can be arbitrary, careful selection of material properties and layer thicknesses can optimize the performance (i.e. here both in terms of the strength and uniqueness of the reflected acoustic signature) of the tag over the frequency band of interest. The two primary physical mechanisms governing the response of the AID tag are the mismatch in characteristic acoustic impedance between successive layers of the tag, and the incurred acoustic attenuation of the interrogating signal as it propagates through the layers of the tag. The effects of impedance mismatch and attenuation on the tag response can be collectively modelled using efficient numerical methods for wave propagation in layered media. especially under the flat interface assumption in the high-frequency regime [45] for AID tags made of curved layered shells. As will be shown subsequently, this analysis aims at determining an effective layering strategy and layer thickness for a given frequency band of interest.

#### **4.2 Energy based layering strategy**

The notion of reflected and transmitted energy in each layer as discussed in section 2.2, can be formalized as an energy density per layer metric which indicates the total acoustic energy persistent in a layer when an AID tag is interrogated by a source. Mathematically, the energy density for the  $L$ th layer is computed as a space-time average of the instantaneous energy density [49] in the layer, given in terms of the instantaneous acoustic pressure



$p(z, t)$  (or normal stress) obtained from the Global Matrix solution, layer density ( $\rho_L$ ), and compressional velocity ( $c_L$ ) as

$$E_L(z, t) = \frac{p^2(z, t)}{\rho_L c_L^2} \quad (4.1)$$

Specifically, this instantaneous energy density is averaged over a time duration  $T$  that is chosen to be long enough to account for the multiple arrivals in the layer with the weakest attenuation, and the layer thickness  $d_L$  of the layer domain  $\Omega_L$  to obtain the energy density per layer in Joules/meter in the one dimensional case. It is to be noted that the half-space above and below the layers of the tag is also treated as a layer domain, with the top half-space containing the incident source signal and reflected AID tag signature in this simulation. Additionally, note that in the one dimensional case,  $\Omega_L$  spans the thickness of the layer. Therefore,

$$\hat{E}_L = \frac{1}{d_L T} \int_{\Omega_L} \int_0^T E_L(z, t) dt d\Omega_L \quad (4.2)$$

In the actual implementation, the starting time of the time-integration corresponds to the time when the source is incident on the top interface of the tag, as shown by the vertical dotted lines at the 5  $\mu$ s mark in Figure 4.1(a,b). For the simple cases of the 2 mm aluminium and acrylic plates in water, histograms of the energy density in each layer are shown in Figure 4.1c, and Figure 4.1d. Figure 4.1c shows that there is a clear concentration of energy in the top half-space as most of the incident energy is reflected from the aluminium plate, while Figure 4.1d shows that most of the incident acoustic energy is transmitted to the bottom half-space, with some energy reflected back into the top water half-space. These results are consistent with the expected features of the wave propagation in these layers, thus justifying the use of this simple energy density per layer metric to assess the design of more complex tag configurations. A straightforward implication of these results in tag design for monostatic insonification is the benefit of using a rigid backing plate as the last

layer of the AID tag to reflect as much of the remaining acoustic energy after propagating through all the AID tag layers (see Figure 4.2(a,b)).

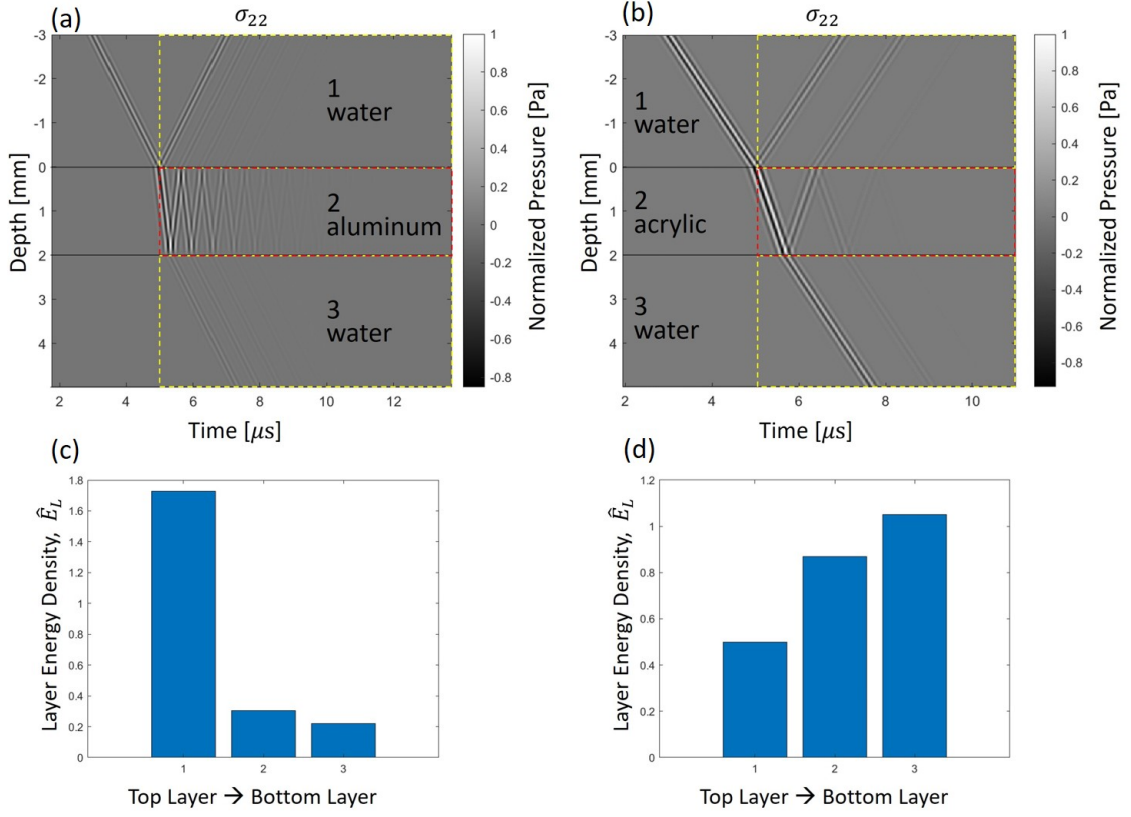


Figure 4.1: a) Time evolution of a Gaussian pulse [ $f_c = 6$  MHz,  $FBW = 0.56$ ] incident normally on a 2 mm aluminum plate; b) Same as (a) but for a 2 mm acrylic plate. Dotted boxes in (a) and (b) indicate the domains of integration for the space-time averaged energy density (see Equation 4.2). c) Histogram of the space-time averaged energy density (also called Layer Energy Density)  $\hat{E}_L$  [Joules/meter], in each domain for a 2 mm aluminium plate shown in (a); d) Same as (c) but for a 2 mm acrylic plate shown in (b).

Using the energy density per layer metric define in Equation 4.2, it is possible to analyze more complex layering strategies and select the one that permits the most incident acoustic energy to the innermost layers of the AID tag, and in addition has the most energetic reflected signal. Furthermore, it is desirable that the intermediate layers of the tag also contribute to the reflected tag signature, which places an impedance mismatch constraint between the adjacent layers of the tag. To motivate this idea, consider the tag layer structures shown in Figure 4.2(a,d). The tag shown in Figure 4.2a is composed of 2 mm

thick acrylic plates alternated with water layers and ending with an aluminum backing plate immersed between two water half-spaces, while the tag in Figure 4.2d replaces the intermediate water layers in the previous tag with PVC. The material properties of the layers of the tags are listed in Appendix B. Since the impedance mismatch between acrylic and water is relatively higher than that of acrylic and PVC, more of the incident acoustic energy at a water-acrylic interface is reflected back into the incident medium than in the acrylic-PVC case. However, close to 75% of the incident energy of a wideband source (1 kHz-1 MHz) is still transmitted across each acrylic layer to interrogate the deeper layers of the tag, and a complex acoustic signature - thus sufficiently unique for identification purposes - can be generated as shown by the trace of the received signal in Figure 4.2b. This is in direct contrast to the tag signature generated by the acrylic-PVC layering where the small impedance mismatch almost completely allows the incident wave to pass through the tag with minimal intermediate reflections as seen in Figure 4.2e. To complicate matters further for the acrylic-PVC tag, the high acoustic damping in the PVC layers significantly attenuates the source signal over the thickness of the tag, thus yielding a very short reflected signature with little uniqueness.

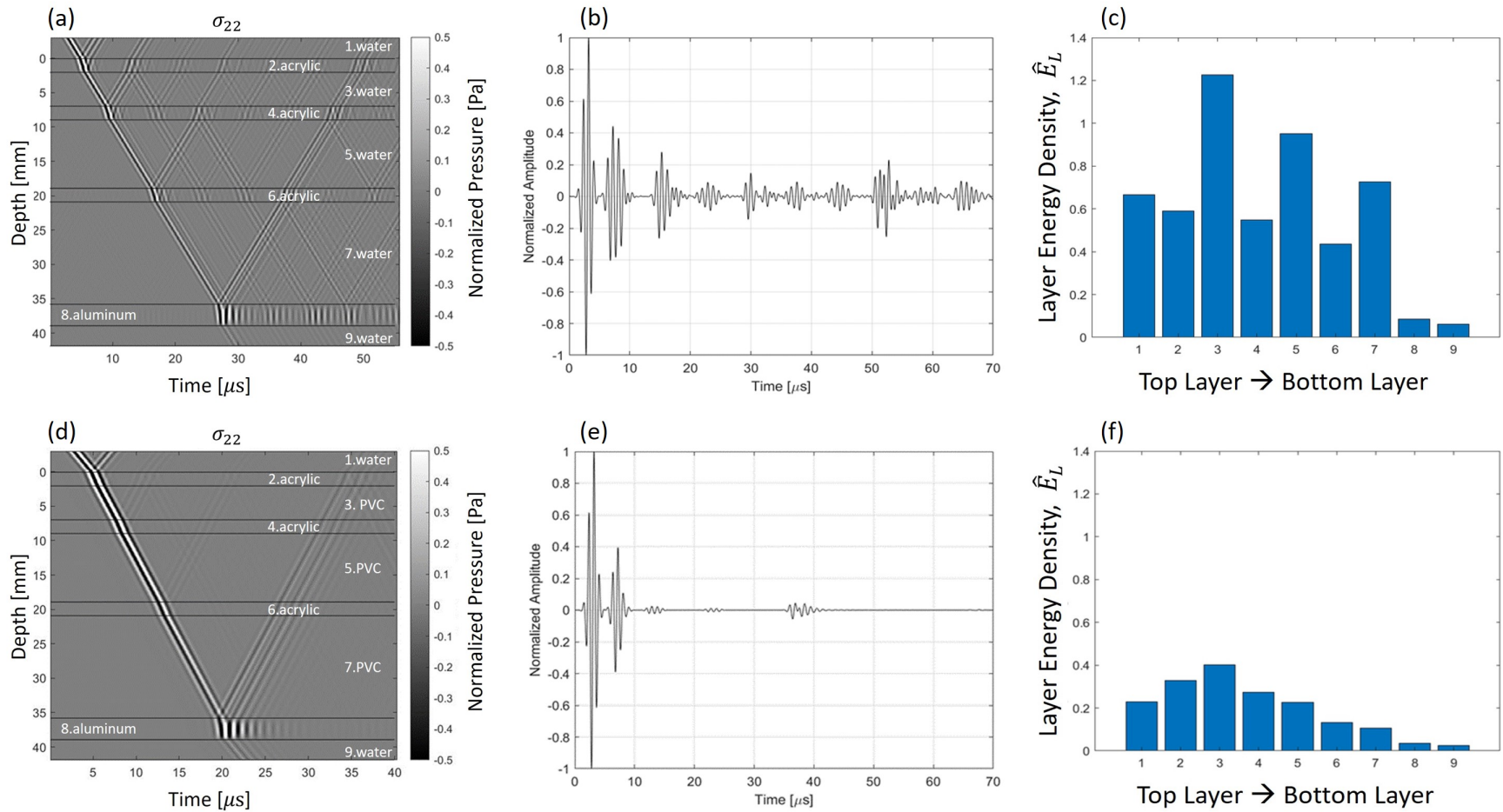


Figure 4.2: a) Time evolution of the same Gaussian pulse used in Figure 4.1 propagating across a tag with three water layers and rigid aluminum backing plate. b) Trace of the reflected signature from tag shown in (a) at depth = -2 mm. c) Layer energy density [Joules/meter] for tag shown in a. d) Time evolution of the same Gaussian pulse used in Figure 4.1 propagating across a tag with three PVC layers, with intermediate acrylic sheets welded to the PVC, and a terminal rigid aluminum backing plate. e) Trace of the reflected signature from tag shown in (d) taken at a depth = -2 mm. f) Layer energy density [Joules/meter] for tag in d).

To consolidate these observations, the layer dynamics for each tag can be summarized using the energy density per layer as in Figure 4.2(c,f). Clearly, the energy density in each layer of the acrylic-water based tag is almost twice that of the corresponding layers in the acrylic-PVC based tag suggesting not only the transport of more energy through the layers of the acrylic-water tag, but also the reduced attenuation of the incident signal propagating through the layer's thickness. It becomes evident therefore, that a tag designed with alternating fluid layers and thin solid layers reflects stronger and more complex signatures than one with welded solid layers even though the impedance mismatch at the fluid-solid interface is likely to be higher than interfaces between polymers of similar bulk properties. Indeed, more complex AID signatures are beneficial in applications such as information encoding or interferer cancellation for example (see chapter 5). Finally, on a practical note, fabricating tags with water layers in between acrylic sheets (which can be achieved by allowing for water ingress between spaced acrylic layers or shells) is also much simpler and durable than having to chemically bond two polymers together.

### 4.3 Optimal elastic layer thickness

Up to this point, mention has been made of tags using thin (2 mm - 3 mm) acrylic sheets as some of the tag layers without justification on the selection of this material and thickness. To formalize a selection strategy for these parameters, the impedance translation [40] theorem can be used to determine the thickness of a material submerged in water to achieve a desired reflected and transmitted power. For a single plate of characteristic impedance  $Z_0 = \rho_0 c_0$  rayl and thickness  $d$  immersed in water with impedance  $Z_1 = \rho_1 c_1$  rayl, the reflection coefficient in the top half-space under normal incidence conditions can be found as

$$R = \frac{i(Z_0^2 + Z_1^2) \tan k_0 d}{i(Z_0 + Z_1) \tan k_0 d - 2Z_0 Z_1} \quad (4.3)$$

where  $k_0[\text{radm}^{-1}]$  is the wave number of a monochromatic plane wave  $p_I$  normally incident on the plate from the top half-space. The reflected and transmitted powers  $R_{\Pi}$  and  $T_{\Pi}$  at the top halfspace-plate interface can be subsequently computed as

$$R_{\Pi} = |R|^2 \quad (4.4)$$

$$T_{\Pi} = 1 - R_{\Pi} \quad (4.5)$$

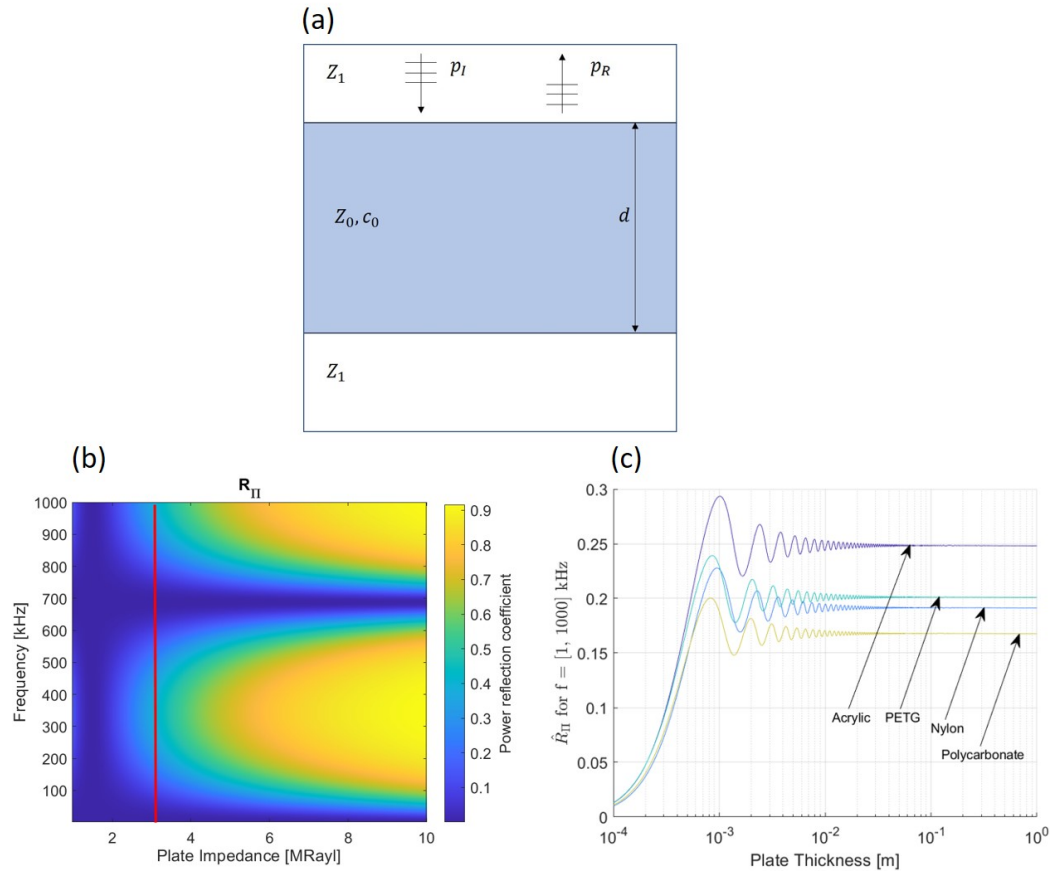


Figure 4.3: a) Schematic of a plate of thickness  $d$  and impedance  $Z_0$  immersed between water half-spaces with impedance  $Z_1$ . Monochromatic incident and reflected plane waves  $p_I$  and  $p_R$  respectively are present in the top water half-space. b) Reflected power as a function of frequency and plate impedance for a plate of constant thickness (here 2 mm) immersed in water, computed using the impedance translation theorem. (solid line indicates acrylic impedance) c) wideband [0 - 1 MHz] reflected power from plates of varying material and thickness immersed in water. For the case of a 2 mm acrylic plate for example, the reflected power  $\hat{R}_{\Pi}$  as computed from Equation 4.6 is  $\sim 0.23 \times$  the source power.

It is evident from Equation 4.3 that the plate reflection coefficient, and hence the reflected power in Equation 4.4 are dependent on the plate thickness  $d$ , and the frequency of the incident wave  $f$  in addition to its characteristic impedance. For a constant plate thickness - in this example, 2 mm - the reflected power computed for a range of frequencies and plate impedances is shown in Figure 4.3a. Clearly, a plate with an impedance of approximately 1.5-2 Mrayl transmits most of the incident acoustic energy over the entire frequency band due to impedance matching with water. As plate impedance increases however, nodes corresponding to complete transmission (dark sections) and antinodes corresponding to complete reflection (bright sections) arise over the frequency sweep indicating partial energy transmission through the plate, and energy reflected back into the water. The nodal regions that persist over the impedance sweep arise due to half-wavelength matching of the interrogating frequency with the thickness of the plate. It is to be noted that Figure 4.3b assumes a constant compressional velocity of the plate of 2750 m/s for all impedance values. This corresponds to the compressional velocity of acrylic and is set as a reference. With increasing plate impedance, there is an expected increase in reflected energy over a larger frequency band. Selecting a material with a plate impedance which permits some reflectivity is desirable, and in the current example of a 2 mm thick plate, a plate impedance in the range of [3.5 - 5] Mrayl is recommended. For reference, the plate impedance of acrylic is marked as a solid line in Figure 4.3b and suggests that the frequency bands between [50 - 600] kHz and [750 - 1000] kHz have a power reflection coefficient of approximately 0.4.

Furthermore, Equation 4.4 can also be used to evaluate the optimal plate thickness for a desired power reflection coefficient over a specified frequency band. Given a plate impedance  $Z_0$  and plate thickness  $d$ , a cumulative power reflection coefficient  $\hat{R}_{\Pi}(d)$  as a function of plate thickness can be computed as an average of the power reflection coefficients  $R_{\Pi}(f, d)$  at each frequency. That is

$$\hat{R}_{\Pi}(d) = \frac{1}{N} \sum_f R_{\Pi}(f, d) \quad (4.6)$$

Solving Equation 4.6 between [1 - 1000] kHz for different values of  $d$  for materials such as acrylic, polycarbonate, nylon-66, and polyethylene terephthalate glycol (PETG) provide the cumulative reflection curves plotted in Figure 4.3c. For very thin plates ( $< 0.5$  mm), the reflected power is close to zero as the plates merely act as very thin membranes separating two fluids. The reflected power increases to a maximum value as plate thickness increases, after which it oscillates about an average value. The oscillations in the reflected power are once again due the half-wavelength matching of frequencies for the given plate thickness. While either PETG or nylon prove to have the ideal reflected energy, 2 - 3 mm thick acrylic sheets have been selected for tag construction due to ease of availability and low costs. Acrylic sheets have power reflectivities in the range of [0.22 - 0.26] and are thus considered suitable for AID tag design in the remainder of this study.

#### **4.4 Effect of source bandwidth on AID tag detectability**

In addition to specifying the physical design parameters of the AID tag itself as in section 4.1, it is useful to understand the influence of the bandwidth of the insonifying source on the AID reflected signature. While it is intuitive that large source bandwidths afford better temporal (and therefore spatial) resolutions allowing for more complex, and thus more unique AID tag signatures, this comes at the cost of greater attenuation of the high-frequency source components and thus may limit the range of detectability of the tag. The effect of source bandwidth on the response of an AID tag with an arbitrary number of fluid layers sandwiched between thin polymer sheets is investigated in this section by simulating the temporal response of the tag to an incident Gaussian source signal of a given center frequency ( $f_c$ ) and fractional bandwidth ( $FBW$ ) using the simulation framework described in section 2.2. For simplicity, the simulations use constant thickness polymer sheets - here 2 mm thick acrylic sheets - separating the water layers of the AID tag. In order to resolve the interfacial reflections from the water layers of an AID tag, the water layer thicknesses need to be selected such that they are thicker than the attainable spatial resolution by the



source pulse.

For example, for a Gaussian pulse, the attainable spatial resolution can be specified in terms of the temporal pulsewidth as

$$\Delta x = 2 \times \tau_{-6dB} c_L \quad (4.7)$$

Where  $\tau_{-6dB}$  is the temporal pulse width at half the maximum pulse amplitude of a Gaussian source pulse, and where  $c_L$  is a reference wave propagation velocity. It is to be noted that the pulsewidth  $\tau_{-6dB}$  is also inversely proportional to the frequency bandwidth  $B$ . Therefore, in order to resolve the reflections from the water layers of the AID tag, the minimum water layer thickness  $d_{min}$  is set hereafter to be

$$d_{min} = 2.5 \times \tau_{-6dB} c_L \quad (4.8)$$

Where the factor of 2.5 is chosen as a conservative value close to the resolution limit stated in Equation 4.7. The thickness of every additional fluid layer  $d_l$  in the tag is specified as

$$d_l = (2.5 + \alpha(l - 1)) \times \tau_{-6dB} c_L \quad (4.9)$$

where  $l$  is the fluid layer number indexed from 1, and  $\alpha$  is a constant which specifies the layer thickness increment, proportional to the pulsewidth  $\tau_{-6dB}$ . Hereafter,  $\alpha$  is set arbitrarily to 0.25 so that the reflections from the additional fluid layers are clearly seen, while preventing the subsequent layers from being too thick since propagation losses over larger thicknesses would significantly attenuate the later arrivals. Furthermore, it will be shown in a later section that variable fluid layer thicknesses enhance the uniqueness of the tag, and therefore the current analysis assumes a non-zero  $\alpha$ . This method of specifying fluid layer thicknesses normalized by frequency band, allows the direct comparison of tags and their responses over for a range of bandwidths. Additionally, the simulation is run for

AID tags with and without terminal rigid backing plates to illustrate the efficacy of using a strong reflector at the end of the tag structure as indicated by the results shown in Figure 4.1 and Figure 4.2.

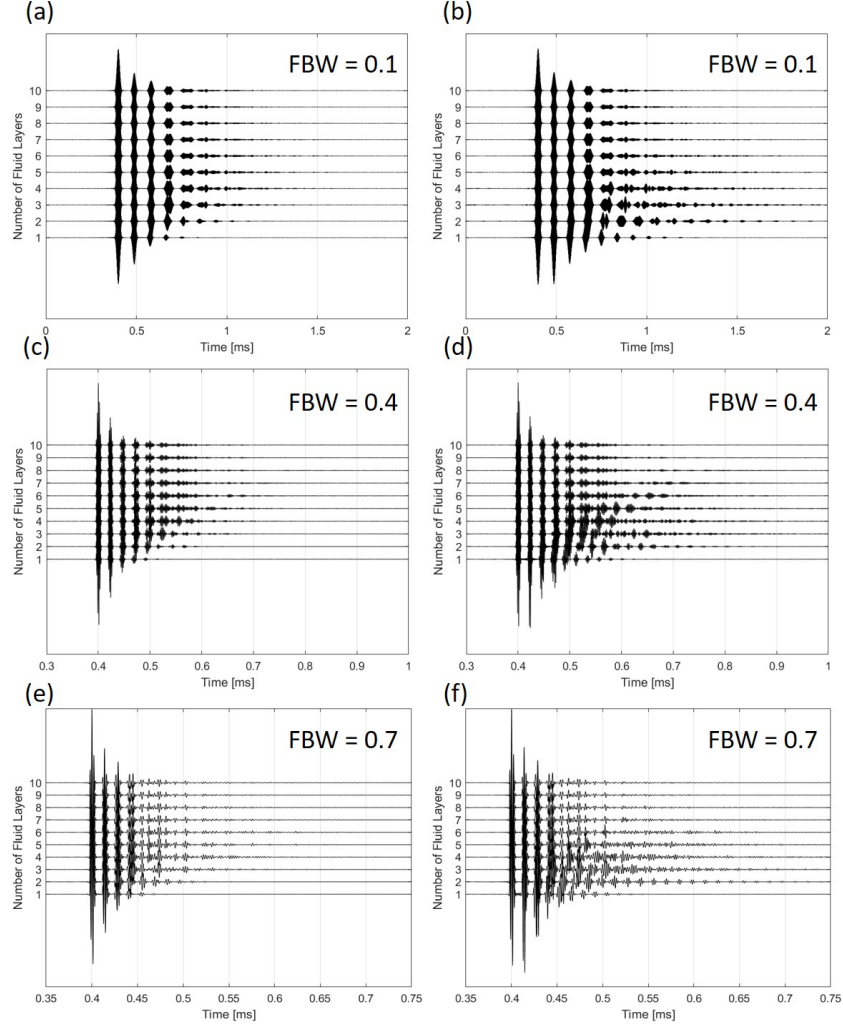


Figure 4.4: Simulated AID tag signatures for different source fractional bandwidths, and number of layers. The left column shows signatures of tags with no backing plate. The right column shows signatures of tags that have a 2 mm aluminium backing plate as the last layer. The top row (a, b) shows tag signatures for a narrowband source ( $f_c = 500$  kHz,  $FBW = 0.1$ ). The middle row (c, d) shows tag signatures for a mid-band source ( $f_c = 500$  kHz,  $FBW = 0.4$ ). The bottom row (e, f) shows tag signatures for a wideband source ( $f_c = 500$  kHz,  $FBW = 0.7$ ).

One simple metric for comparing the performance (in terms of practical detectability) of AID tags as a function of bandwidth is to compute the total energy  $E$  as the L2-norm of the reflected tag signatures. Prior to a full scale analysis of the effect of source bandwidth on AID tag energy, Figure 4.4(a - e) show simulated AID tag signatures for one to ten fluid layers, without and with a terminal backing plate respectively for a narrowband ( $FBW = 0.1$ ), midband( $FBW = 0.4$ ), and wideband( $FBW = 0.7$ ) incident Gaussian pulse source ( $f_c = 500$  kHz), with fluid layer sizing specified based on Equation 4.9, with 2 mm thick acrylic plates used to separate each fluid layer. It is to be noted that when AID tags are designed for narrowband sources ( $FBW \sim 0.1$ ) using Equation 4.9, the layer sizes can be large, and is a factor to consider while designing the tag. In each case simulated, the total energy of the incident pulse for all bandwidth cases is the same by suitably scaling the source amplitude.

The resulting AID tag signatures highlight the interaction between the polymer-water impedance mismatch and signal attenuation in the water layers. Indeed, with an increase in the number of fluid layers and thicknesses, two different template energy trends have been observed. For tags designed without a backing plate, the tag energy increases to a maximum value when there are 2-3 fluid layers, and approximately remains constant for more layers as no further layer contributions are returned due to the attenuation of energy through the later layers as in Figure 4.4a, Figure 4.4c, and Figure 4.4e. On the other hand, tag signatures for designs that include a rigid aluminum backing plate as in Figure 4.4b, Figure 4.4d, and Figure 4.4f contain returns from both, the fluid layers of the tag, and the strong energetic multiple arrivals from the aluminium backing plate. In the current tag design scheme, the AID tag with a single water layer and with an aluminum backing plate reflect the most energy, which is mostly contributed from the reflections of the aluminum plate. With the increase in the number of fluid layers, a monotonic decrease in tag signature energy is observed, corresponding to more attenuated arrivals at the aluminum plate, thereby weakening its contribution to the tag signature. Clearly from this qualitative study

of Figure 4.4, the presence of a backing plate is shown to generate stronger tag signatures for the same layer arrangement, and is the preferred method of AID tag construction.

For a more comprehensive understanding of the relationship of the source bandwidth on the tag template energy, tags with one to ten fluid layers are simulated as discussed previously, now over a broader range of source fractional bandwidths  $[0.1, 0.7]$  incremented in steps of 0.03. Template energies for each tag signature are computed and the simulation is repeated with and without a backing plate. Both simulations are normalized by the same maximum template energy across both simulations. Figure 4.5a indicates the tag energy for designs without the backing plate, and as discussed earlier, there are energy maxima for tags with two or three layers, followed by a gradual decrease in template energy. As expected, all template energies of tags without a backing plate are lesser than those of tags with backing plates. Figure 4.5b shows the monotonic decrease in template energy with increase in the number of fluid layers. While it is desirable to have tags with several intermediate fluid layers so as to generate a complex reflected signature, the inherent decrease in template energy with increase in the number of layers suggests that around four to six fluid layers provide the best compromise between the response complexity (i.e. the uniqueness of the arrival-time structure of the AID tag's reflection) and response strength (to ensure detection of the tag's response over ambient noise or surrounding clutter).

In order to maximize the likelihood of tag detection, it would be desirable to select source signals that generate the most energetic reflected responses from AID tags. Figure 4.5b suggests that any source bandwidth generates tag templates with the same energy for a given number of fluid layers. Care must however be taken to acknowledge the inverse relationship between source bandwidth and minimum layer size as discussed earlier (see Equation 4.8 and Equation 4.9). In order to resolve the interfacial reflections from tags using sources with small fractional bandwidths such as 0.1 or 0.2, the fluid layer thicknesses of the tags can become quite large due to the spatial resolution constraints. Using Equation 4.7, the minimum attainable spatial resolution of a water layer in a tag is approx-

imately 1.5cm when a narrowband source ( $f_c = 500$  kHz,  $FBW = 0.1$ ) is used. Here, the center frequency of the source is set to 500 kHz as typical high frequency SONAR devices[cite Starfish] operate around this regime. Over large numbers of layers of varying thicknesses, the size of the tag can grow to be considerably large. Furthermore, previously demonstrated omnidirectional acoustic tags using hemispherical shells [54] are designed for the high wavenumber-radius ( $kR$ ) regime which implies that the large wavelengths of the source signal force the minimum radius of the hemispherical shells to be large. As a design compromise, using a fractional bandwidth of 0.4, say, increases the spatial resolution by a factor of 4 while the tag template energy for this source is still approximately 60% the energy of the most energetic template. In this manner, AID tags can be designed for varying source bandwidth specifications.

## 4.5 Chapter Summary

This chapter proposed an energy based AID tag layer optimization strategy to maximize the energy that penetrates the different layers of a tag. It was shown that using alternating plastic and water layers provided the most energetic and complex AID tag signature, relative to using welded plastics. Using the impedance translation theorem, a relationship between the thickness of the plastic layers used in tag construction and the corresponding wideband power reflection coefficient was established for different plastics. Finally, a source bandwidth dependent water layer dimensioning strategy was specified for AID tags such that the layers of the AID tag could be spatially resolved by the interrogating source.

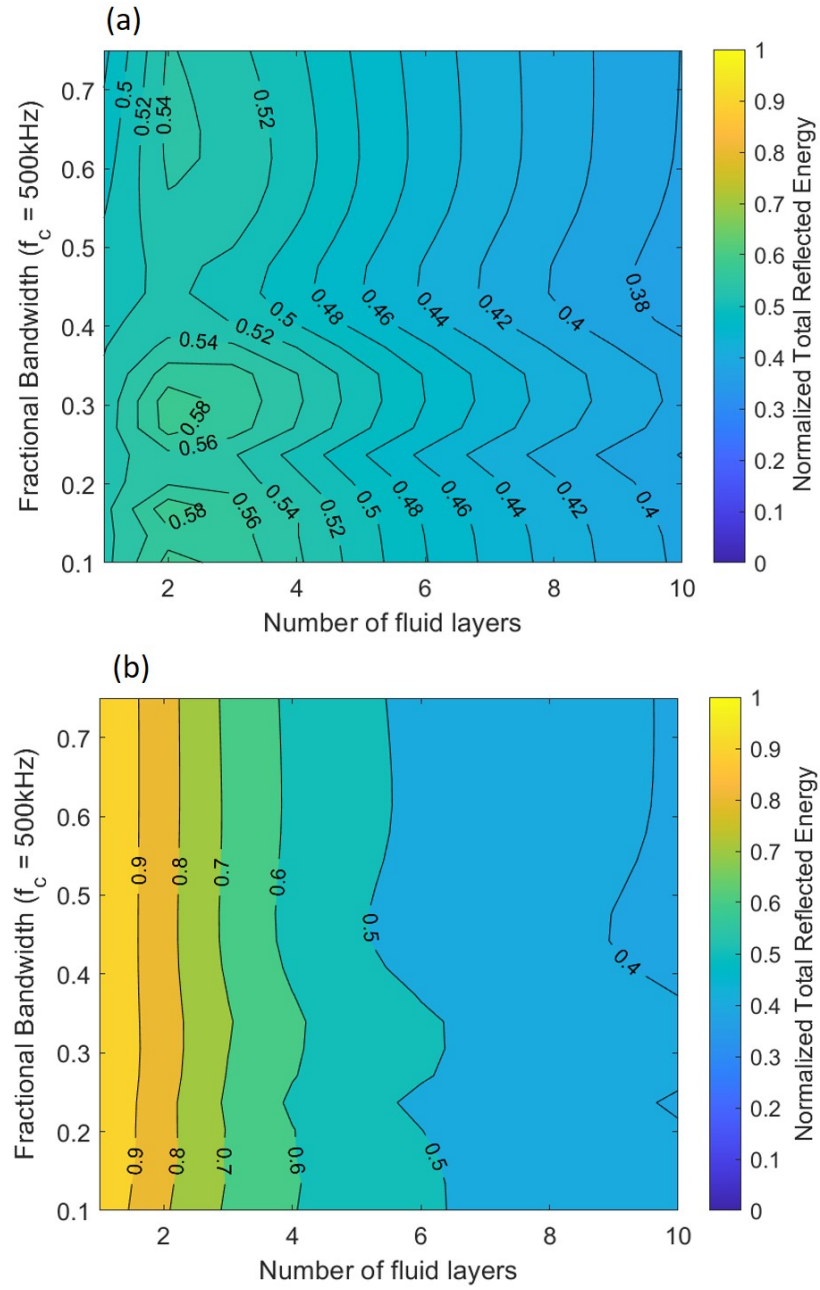


Figure 4.5: a) Total reflected energy for AID tags with different numbers of fluid layers with no rigid backing plate, as a function of source fractional bandwidths. b) Total reflected energy for AID tags with different numbers of fluid layers with rigid backing plate, as a function of source fractional bandwidths. Both a) and b) are normalized by the same maximum template energy value across both simulations.

## CHAPTER 5

### AID TAG DETECTION

#### 5.1 Match-filtering performance of AID tags

Two key points of study in the design of AID tags are the detectability of a tag signature in the presence of an interferer such as an echo from surrounding clutter, and the correlation coefficient between pairwise combinations of various AID tag signatures to quantify the uniqueness of each AID tag signature for identification purposes. The prior is of interest since possible applications of AID tags would see them deployed near the sea bed where the sediment or other clutter may strongly reflect any incident signals. Other scenarios where AID tags might be situated near rigid underwater man-made structures could also see the AID tag signature competing with the reflections and reverberation of the surrounding area. Additionally, the capability to uniquely identify one AID tag from another allows for the use of different markers to convey different instructions to an AUV for example.

Match Filtering (MF) is a signal detection technique where a stored 'template' AID tag signature is cross-correlated with the target data - which contains either another AID tag signature to measure the degree of similarity between the two templates, or noisy data where the tag signature is embedded, possibly near an interfering signal. This cross-correlation operation serves to boost the tag signature and suppress noise and interference by means of phase matching delayed versions of the template and the data [73]. The discretized, normalized cross correlation ( $\hat{R}_{xy} \in [-1, 1]$ ) of noisy data ( $x_n$ ) against shifted copies of a template ( $y_n$ ) (both of length  $N$ ) is given by

$$\hat{R}_{xy}(m) = \frac{1}{\sqrt{\hat{R}_{xx}(0)\hat{R}_{yy}(0)}} \sum_{n=0}^{N-m-1} x_{n+m}y_n^*, m \geq 0 \quad (5.1)$$

where  $m \in [0, N - 1]$  is the number of samples the tag template has been shifted,  $\hat{R}_{xx}(0)$  and  $\hat{R}_{yy}(0)$  are the autocorrelation values of the raw data and template at 0 lag (corresponding to the total energy of each signal) respectively.

## 5.2 Tag detection near an interferer

One practical challenge in detecting an AID tag is the presence of a strong interfering signal. However, if the arrival time structure of the reflected signal from the interferer is sufficiently different from the reflected signal from the tag (i.e. the tag template), then match-filtering using a tag template as a reference waveform can be used to boost the AID tag's return in the matched-filtered output. The more decorrelated the tag template's signal is with the interferer signal, the greater the confidence in detection. The Original Signal-to-Interference Ratio (OSIR), i.e. before match filtering, is defined in terms of the ratio of the peak amplitudes of the tag signature and interferer (see Figure 5.1a), and is given by

$$SIR = 20 \log \left( \frac{P_{tag}}{P_{int}} \right) \quad (5.2)$$

where  $P_{tag}$  represents the peak amplitude of the tag signature (typically corresponding to either the first layer reflection or backing plate reflection, and  $P_{int}$  the (known) peak amplitude of the simulated interferer. On the other hand, the raw data containing the tag and interferer's reflected signal (e.g. see Figure 5.1a) can also be match filtered using the AID tag template (known *a priori*), and the resulting peak amplitude ratio of the tag and interferer signal can be computed after detecting correlation peaks using standard peak detection algorithms. The Signal-to-Interference Ratio (SIR) after Match Filtered Signal-to-Interference Ratio (MFSIR) can therefore be expressed as

$$MFSIR = 20 \log \left( \frac{|p_{MF}(t_{tag})|}{|p_{MF}(t_{int})|} \right) \quad (5.3)$$



where  $p_{MF}(t)$  represents the match filtered output signal,  $t_{tag}$  the time corresponding to the AID tag's match filtered peak, and  $t_{int}$  the time corresponding to the interferer's match filtered peak.

For example Figure 5.1a shows a 4-layer tag with an aluminium backing plate and with the layering strategy described in section 4.4 simulated for an incident Gaussian source pulse ( $f_c = 500$  kHz,  $FBW = 0.75$ ). In this simulation, in order to better visualize the effect of matched-filtering, the reflected signal from the tag is arbitrarily separated by 0.5 ms from a strong interfering signal whose peak amplitude is arbitrarily selected to be 0.9 times the original source pulse's maximum amplitude (e.g. to mimic a very reflective clutter feature such as a rigid boundary). Furthermore, a 5 dB white Gaussian noise relative to the total (tag + interferer) power is added to simulate a moderate level of additive measurement noise. The OSIR of the (tag + interferer) simulation before match filtering is found to be -5.96 dB using Equation 5.2 and is the ratio of the tag peak at  $t = 2$  ms and interferer peak at  $t = 2.5$  ms. The strong interfering signal correlates highly with the energetic first reflection of the tag signature (due to the most energetic reflection from the first layer of the tag) as both arise from the same Gaussian source. However, the later arrivals of the tag signature add constructively to the matched filtered output using the tag's template as a reference and thus provide a final MFSIR of +1.29 dB (from Equation 5.3), corresponding to an SIR gain of 7.25 dB as shown in Figure 5.1c allowing now for a positive detection of the AID tag.

While template matching in this manner still allows for the detection of the tag, using a template that is thresholded to a fraction of its peak amplitude [74, 75, 76] offers better match filter gains as the thresholding operation essentially balances the match filter gains from the strong first reflection from the template, with the detection of the later details of the template's structure (which are now effectively amplified by the thresholding operation). Indeed, the match filtered output for the same simulation setup as described above, but using a 4-layer template thresholded to 50% of the maximum tag amplitude

(corresponding to the truncated portion of the AID signature between the dotted lines in Figure 5.1b), produces a final SIR of +2.79 dB (corresponding to an SIR gain of 8.75 dB) and outperforms the unthresholded template by +1.5 dB as shown in Figure 5.1(b,d). Furthermore, it is to be noted that the SIR gain (or compression gain) achieved by the match-filter template is agnostic to the strength of the receiver and is specific to each AID tag designed and match-filter used.

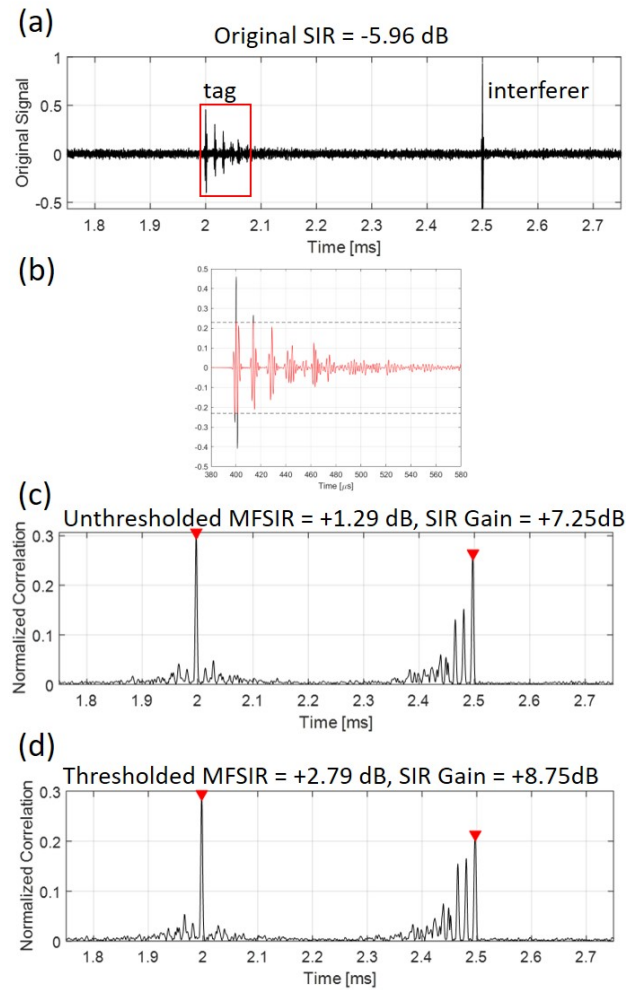


Figure 5.1: a) Simulated 4-layer tag response (marked in box) in the proximity of a strong interferer and in the presence of added measurement noise. b) Enlarged version of the 4-layer tag signature marked in (a). The truncated portion of the signal between the dotted lines corresponds to the 50% thresholded signature. c) Match filtered output using an unthresholded (100%) template boosting the original tag signal with an SIR gain of +7.25 dB. d) Match filtered output using a thresholded (50%) template boosting the tag signal with an SIR gain of +8.75 dB.

As a continuation to the idea of thresholding the template signature in order to boost the MFSIR of tags near an interferer, a full parameter study is presented to evaluate the effects of amplitude thresholding on tags with various geometries. Specifically, tags with 1 to 10 fluid layers, with and without terminal backing plates are simulated with either uniform layer thicknesses or varying layer thicknesses. The uniform layer thickness case assumes that all fluid layers in the tag template have the same thickness, and serves as a reference to understand the impact of varying fluid layer thicknesses. For both the case of AID tags with uniform and varying layer thicknesses, the layer sizing is as described in section 4.4. As earlier, an interfering signal with an arbitrarily set amplitude equal to 0.9 times the amplitude of the original source signal is placed now 2 ms away from each tag signature, and -5 dB white Gaussian noise is added to the signal mixture, relative to the total signal power. Each simulated signal is match filtered with the corresponding template, thresholded to various amplitude levels in decrements of 5% starting from no thresholding (or 100% saturation level). All simulations are run using the same wideband source pulse ( $f_c = 500$  kHz,  $FBW = 0.75$ ). Four simulations are set up by permuting the use of a rigid backing plate, and the use of uniform fluid layers. For each case, the SIR gains for various thresholding levels is assembled into a contour map which represents the set of tags' performance curves as shown in Figure 5.2(a - d). Any combination of thresholding, use of backing plate, and layering strategy that yields an SIR gain sufficient to boost the MFSIR to 0 dB or greater will theoretically allow for the detection of the corresponding tag for the selected simulation parameters.

By inspection of Figure 5.2, it is evident that the use of the backing plate offers the highest SIR gains, with all other parameters constant. Nonetheless, tags without a backing plate can still be detected under the right thresholding and layering combinations. For example, a two layer tag with varying layers, but without a rigid backing plate as in Figure 5.2d can still be detected near strong interference (OSIR  $\sim$  -6 dB) if the template is saturated to around 60% its peak amplitude. Given the obvious advantage that a backing plate presents,

the rest of the discussion will focus on tag designs using backing plates, but the analysis generalizes to the cases without a backing plate as well. Figure 5.2(a,c) indicate that the use of fluid layers with varying thicknesses offer a performance advantage over tags with uniform layers. The variability in the layer sizes enhances the complexity (or diversity) of the arrival time structure of each tag signature therefore increasing the detection gains, akin to increased channel capacity in complex telecommunication channels [77, 78]. In both the uniform and varying layer thickness cases however, the maximum SIR gains are seen for the cases of tags with 2 to 6 fluid layers, relating directly to the limitations set by the impedance mismatch and attenuation mechanism described in section 4.1.

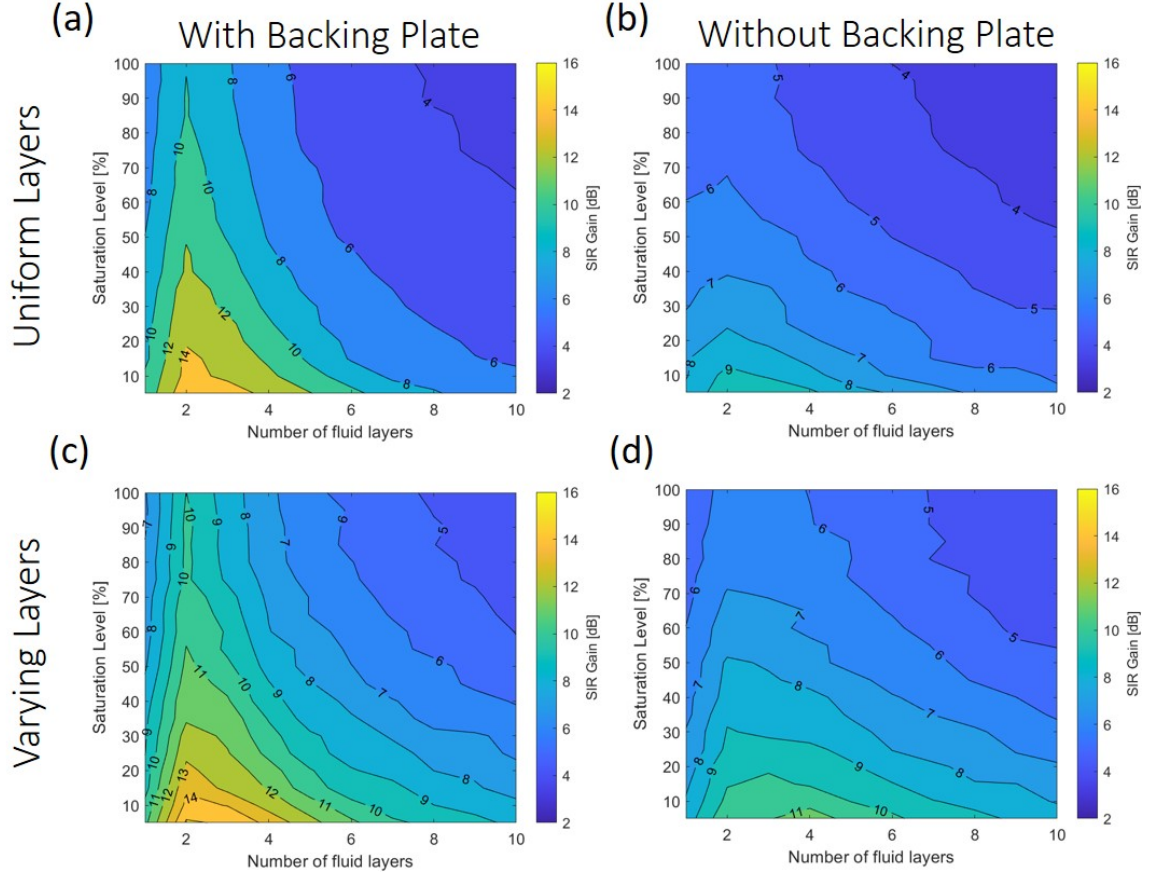


Figure 5.2: Post match filtered SIR gains (see Equation 5.3) of tags near a strong interferer for a wideband (375 kHz) source ( $f_c = 500$  kHz), as a function of the number of fluid layers in a tag and template saturation limits using a similar numerical configuration as show in Figure 5.1. a) Variation of SIR gain contours for tags with uniform layer thicknesses and rigid terminal backing plate as a function number of fluid layers and saturation level of the thresholded template signature used for matched filtering. b) Variation of SIR gain contours for tags with uniform layer thicknesses, and without backing plate. c) SIR gain contours for tags with varying layer thicknesses and rigid terminal backing plate. d) SIR gain contours for tags with uniform layer thicknesses and without backing plate.

The previous thresholding simulations were run using the same Gaussian source with a fractional bandwidth of 0.75, corresponding to a source bandwidth of 375 kHz for a source centered at  $f_c = 500$  kHz corresponding to a wideband source. In order to quantify the effect of the source bandwidth, the simulation of tags with varying fluid layer thicknesses and a rigid backing plate is then repeated using instead narrowband ( $FBW = 0.08$ ,  $BW = 40$  kHz) and midband ( $FBW = 0.4$ ,  $BW = 200$  kHz) sources which are more typical to commercially available SONAR instrumentation. Figure 5.3(a - c) indicate the SIR gains for the narrowband to wideband cases respectively. Here, Figure 5.3c is a repeat of Figure 5.2c to ease direct visual comparison. The reduced frequency diversity of the narrowband source leads to the lowest SIR gains of the three cases as the narrowband versions of the AID tag signature become more correlated with the interferer signature when compared to the broadband cases [77, 78]. Overall, the midband case offers a reasonable compromise between hardware requirements and tag performance.

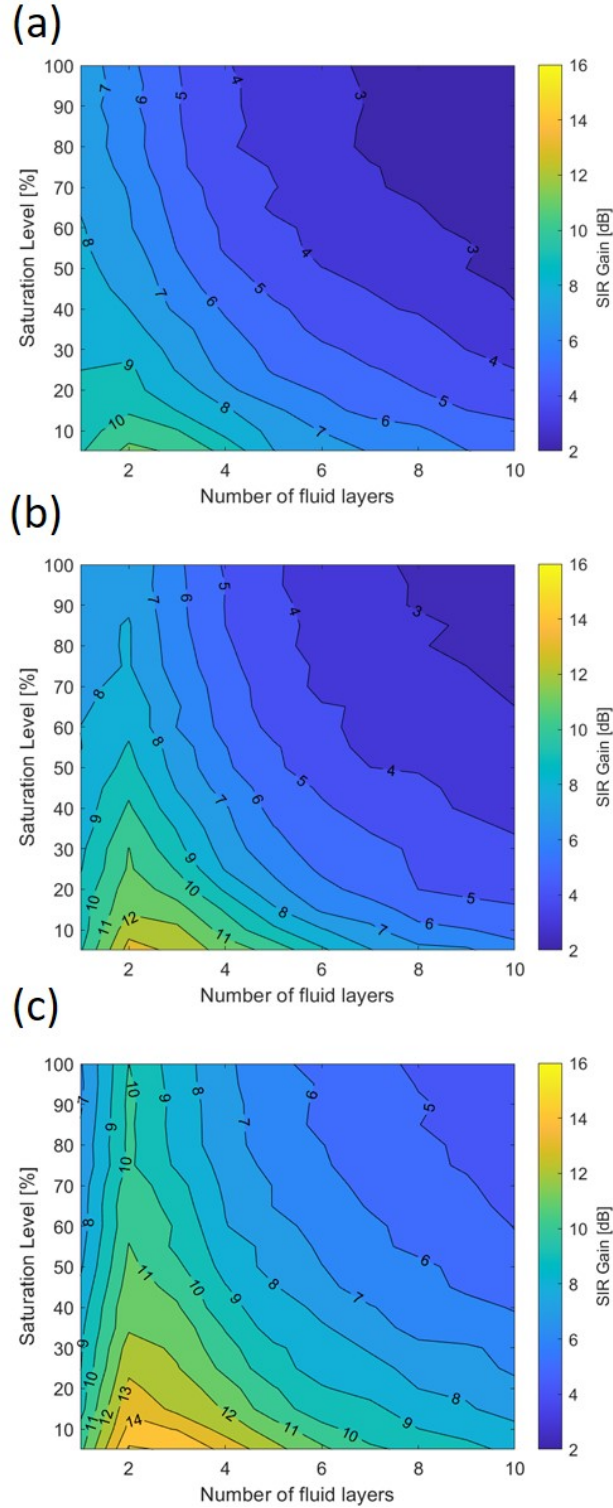


Figure 5.3: Post match filtered SIR gains using tag templates with different numbers of fluid layers, thresholded by different amounts, and designed for different source bandwidths. All simulations use a source with a center frequency of 500 kHz. a) Narrowband (40 kHz) response. b) Midband (200 kHz) response. c) Wideband (375 kHz) response (identical to panel shown in Figure 5.2c)

### 5.3 Template correlations

In addition to detecting an AID tag in the proximity of an interferer, it is also important to be able to distinguish one tag from another to allow for instance, different tags to convey different instructions to an AUV while operating simultaneously. Different tag signatures can be obtained by turning the intermediate acrylic layers of a multi-layer tag 'on' and 'off', akin to changing a binary value where the bit symbol 1 corresponds to the presence of a particular inner acrylic layer, and the bit symbol 0 corresponds to the acrylic layer's absence. For example, a four layer tag contains an outermost acrylic layer, an innermost backing plate, and three intermediate thin acrylic layers to create four fluid-layer partitions in the enclosed volume. A different tag signature may be obtained by the removal and retention of a subset of the intermediate layers. There are  $2^{(N-1)}$  possible combinations in which this is possible for an  $N$  layer tag, and therefore 8 combinations for the four-layer tag above. In practice, it is desirable that the signatures generated by these combinations are as decorrelated as possible from each other, such that standard match-filtering (as used in the previous subsection to reduce the presence of an interfere) can distinguish a target tag from others. Figure 5.4a shows tag correlations for the signatures generated by the four-layer tag mentioned above when the template tag was not thresholded to any value. The average correlation over all comparisons (excluding the autocorrelations) is 0.56, with the most correlations in the [0.45, 0.5] range. Contrasting these results with the case when the target template is thresholded to 20% of its maximum amplitude as in Figure 5.4b, there is a significant decorrelation between signatures, with the distribution of correlation values shifting to a mean of approximately 0.4, with over 50% of the signature correlations in the range [0.3, 0.4].

For instance, Figure 5.4(c,d) show the acoustic signatures corresponding to the 1-1-1 (on-on-on) configuration, and 1-0-1 (on-off-on) configuration respectively. The portions of the signatures between the dotted lines indicate the thresholded signals for an arbitrarily



selected 20% saturation level.

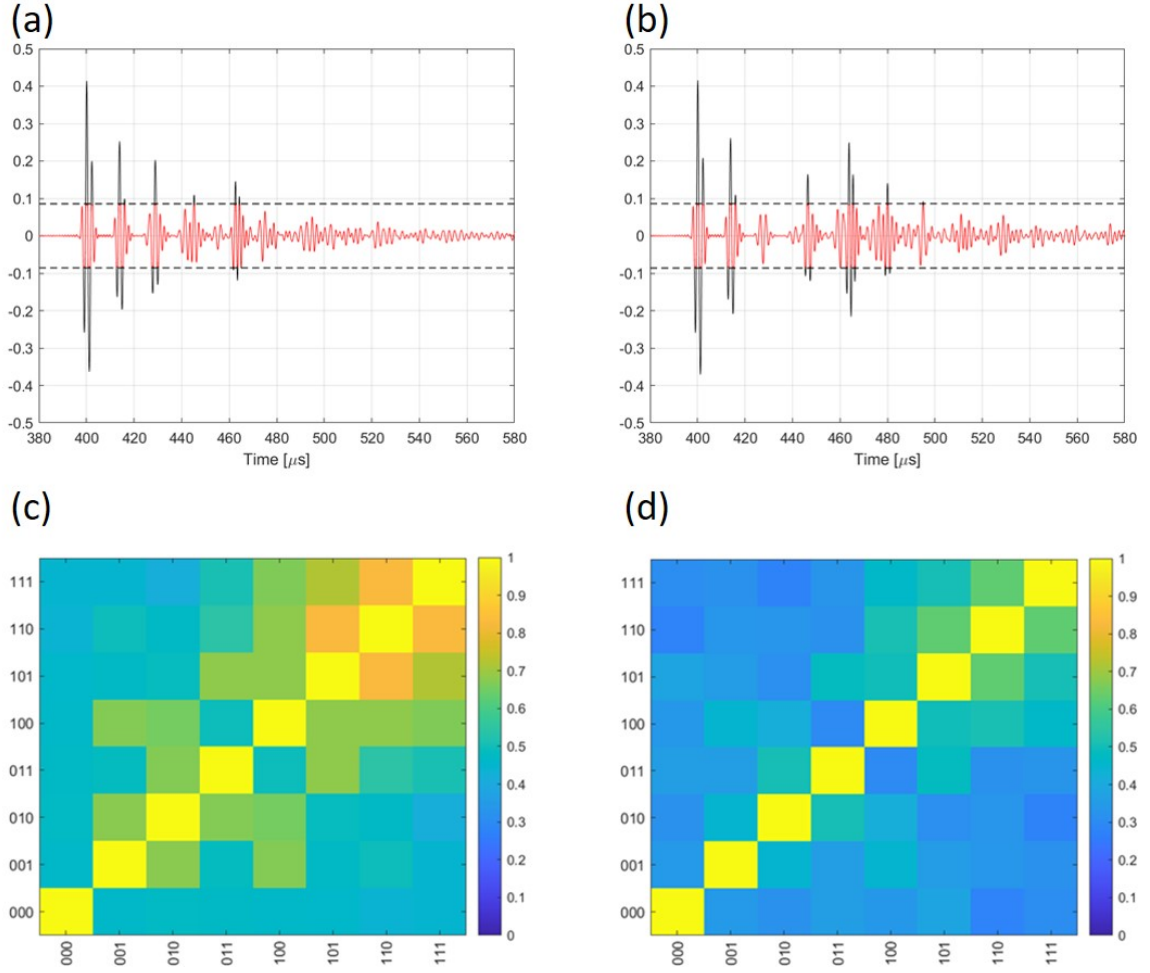


Figure 5.4: a) Tag signature corresponding to the 1-1-1 configuration, corresponding to turning the three inner acrylic layers of a 4-water-layer AID tag ‘on’. This follows the convention where a present or ‘on’ acrylic layer is represented by the bit symbol 1 and an absent or ‘off’ acrylic layer is represented by bit symbol 0. b) Tag signature corresponding to the 1-0-1 configuration. Regions within the dotted line in (a) and (b) correspond to the signature with a 20% threshold applied. c) Variation of the pairwise correlation coefficient between all possible AID tag combinations using the described binary convention. d) Same as (c) but the template signatures are now thresholded to a 20% saturation level.

#### 5.4 A case study of two AID tags in proximity to each other

For additional reference, the case where two tags having a 20% threshold based correlation coefficient in the range of  $[0.3, 0.4]$  (for example the 1-1-0 and 0-1-0 AID tag signatures from Figure 5.4) and are present in the same data acquisition window with equal strength is discussed. Both the 1-1-0 and 0-1-0 tag signatures are simulated and are separated in time by approximately 1 ms to represent the 'raw data' as in Figure 5.5a. The SIR of Figure 5.5a is -0.3 dB, treating the 1-1-0 signature as the signal and the 0-1-0 signal as the interference. Furthermore, no additive noise is added in this simulation. Using a 20% thresholded version of the 1-1-0 AID tag's signature as a template, the raw data is match filtered, and shown in Figure 5.5b. The match filtered peaks of both the 1-1-0 and the 0-1-0 tag are marked and the MFSIR obtained from the peak ratios using Equation 5.3 is found to be +8.4 dB, indicating a clear identification of the 1-1-0 tag, from the 0-1-0 tag, and an overall SIR gain of +8.7 dB.

To demonstrate the robustness of the detection, two additional cases are also presented. The first case places both AID tag signatures closely separated in time to the extent where the 0-1-0 tag signature overlaps with the 1-1-0 signature, as shown in Figure 5.6a. Due to the linear superposition of the two tag signatures, the original SIR for the overlapping signals is in fact lower than the well separated case, and is found to be -0.7 dB. Using the same 1-1-0 template as described previously, a strong detection peak at the location of the 1-1-0 tag, and a weaker 0-1-0 detection is observed and indicated in Figure 5.6b. The MFSIR for this case is found to be 8 dB, corresponding to an SIR gain of +8.7 dB.

Finally, white noise is added to the overlapping tag signatures such that the Signal-to-Noise Ratio (SNR) of the overall signal is -5 dB relative to the combined power of the two AID tag signatures. Here, the SNR is used to specify the standard deviation of the additive white noise, relative to the power of the combined tag signatures. The noise power (or the

variance of the noise,  $\sigma^2$ ) is given by

$$\sigma^2 = P_{signal} 10^{-\frac{SNR}{10}} \quad (5.4)$$

where  $P_{signal}$  is the combined power of the two AID tag signatures, using the standard definition of signal power for a finite support signal  $y(t)$  as

$$P_{signal} = \frac{1}{T} \int_T |y(t)|^2 dt \quad (5.5)$$

where  $T$  is the time duration over which the signal  $y(t)$  persists. In the current case,  $T$  corresponds to the duration of the overlapping AID tag signatures.

This case represents a likely tag detection scenario in underwater environments, where ambient noise and additional interference might overpower the actual reflected signal from an AID tag. Figure 5.7a shows both 1-1-0 and 0-1-0 signatures embedded in noise, in the same locations as in Figure 5.6. While the additional noise occludes a large portion of both AID tag signatures in this simulation, the SIR of the data is found to be -2.57 dB, computed again from the ratio of peak amplitudes from the known locations of both AID tags. The lower SIR is again attributed to the contributions from the noise and tag signature superposition to the interfering signal. Using the same template as in the previous cases, the match filtered output of the signal is shown in Figure 5.7b, where the 1-1-0 tag is clearly identified, while the 0-1-0 signature is suppressed. The MFSIR is found to be 7.15 dB, corresponding to an SIR gain of +9.72 dB, which is interestingly higher than the previous two cases.

Table 5.1: Match filtered results obtained using a 1-1-0 AID tag template thresholded to a 20% saturation level to detect a 1-1-0 AID tag in proximity of a 0-1-0 tag under varying conditions of signal overlap and noise.

Case	OSIR [dB]	MFSIR [dB]	SIR Gain [dB]
Well Separated	-0.3	+8.4	+8.7
Overlap	-0.7	+8	+8.7
Overlap + Ambient Noise	-2.57	+7.15	+9.72

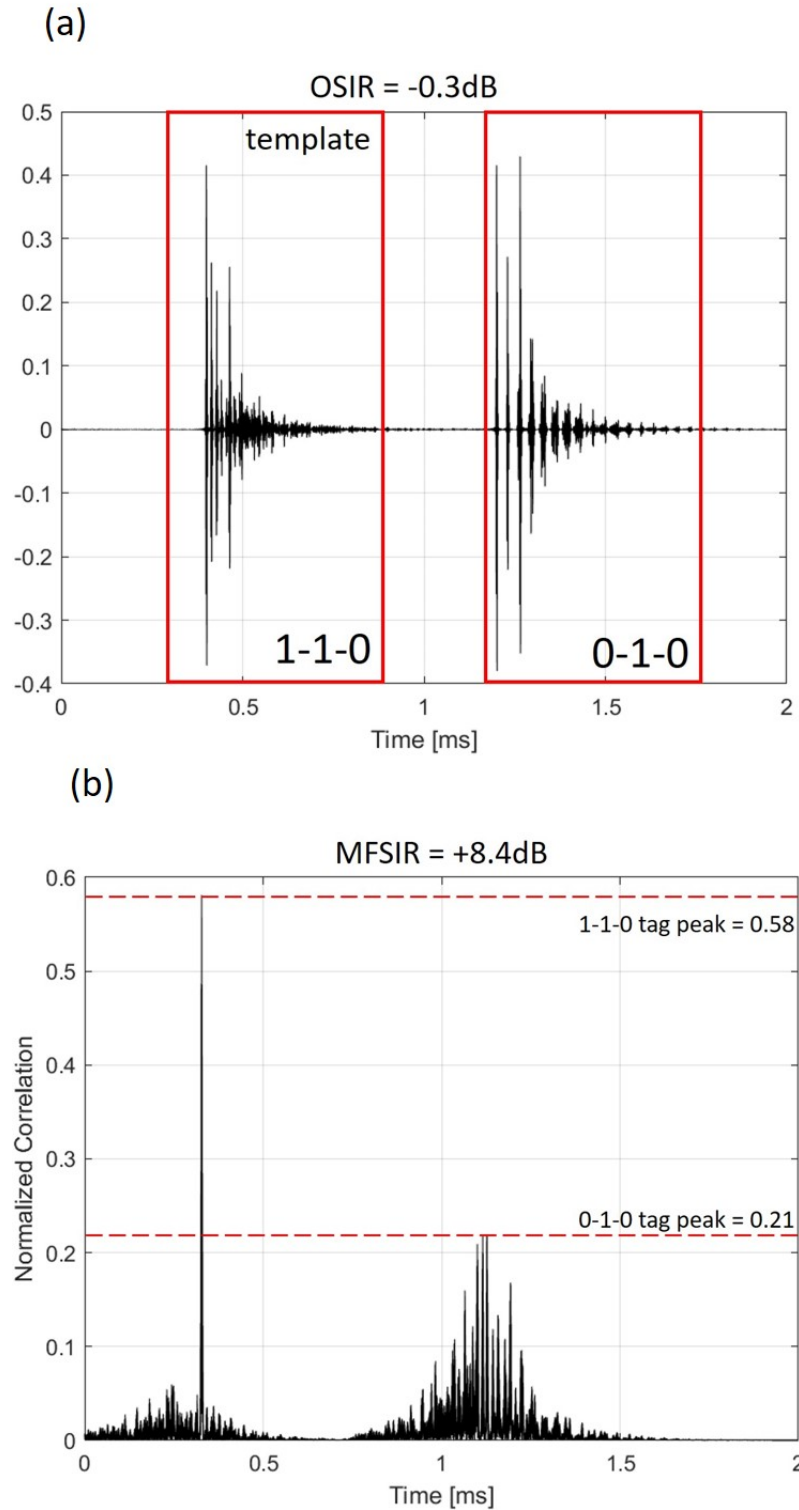


Figure 5.5: a) Simulated signal containing the 1-1-0 and 0-1-0 AID tag signatures, separated in time by approximately 1 ms as marked. The OSIR of the signal mixture is -0.3 dB. b) The match filtered output obtained by using a 20% thresholded version of the 1-1-0 template for the case described in (a). The MFSIR is found to be +8.4 dB.

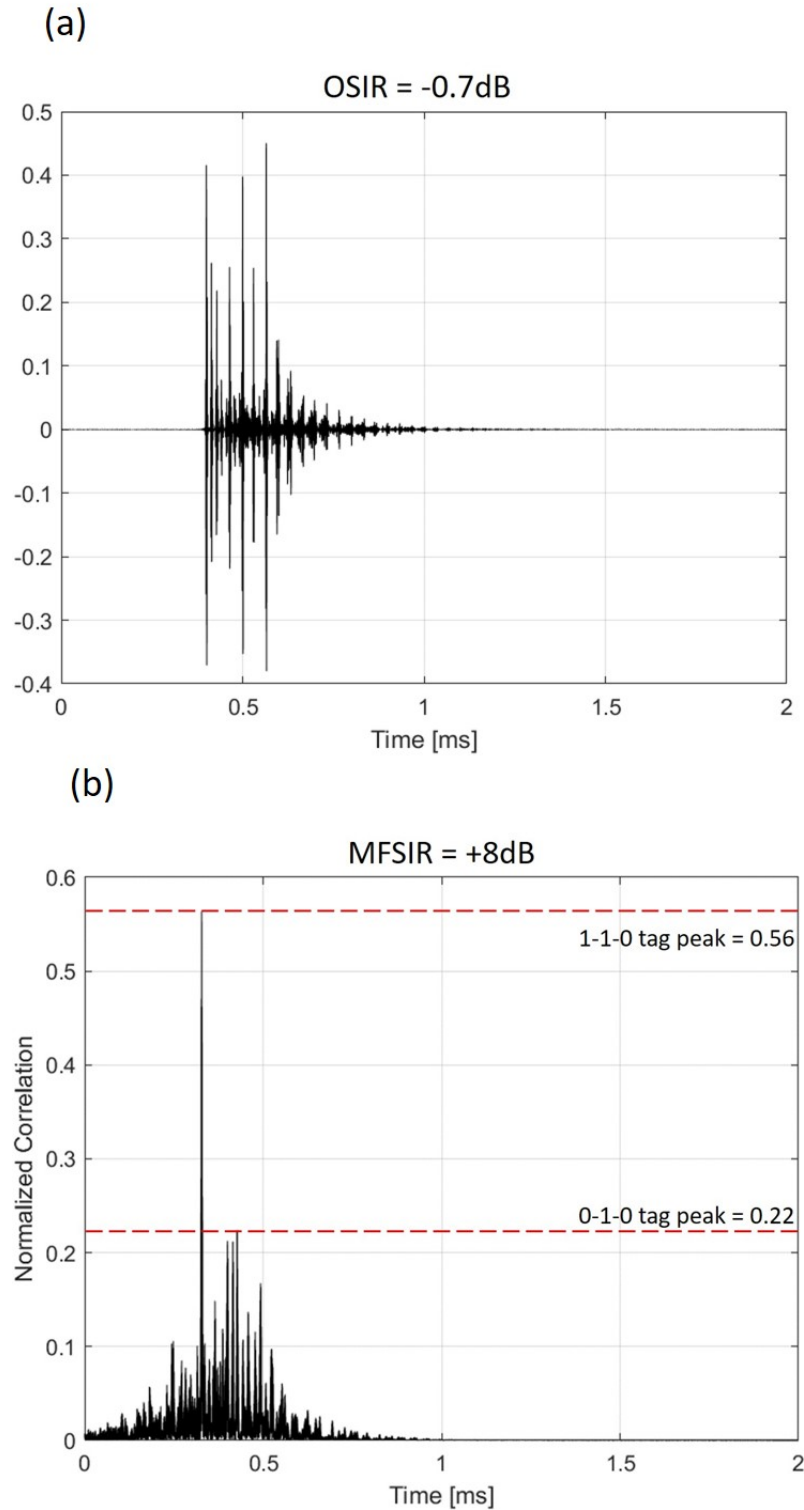


Figure 5.6: a) Simulated signal containing the 1-1-0 and 0-1-0 AID tag signatures, similar to Figure 5.5, but now placed such that both tag signatures overlap in time. The OSIR is -0.7 dB. b) The match filtered output obtained by using a 20% thresholded version of the 1-1-0 template for the case described in (a). The MFSIR is found to be +8 dB.

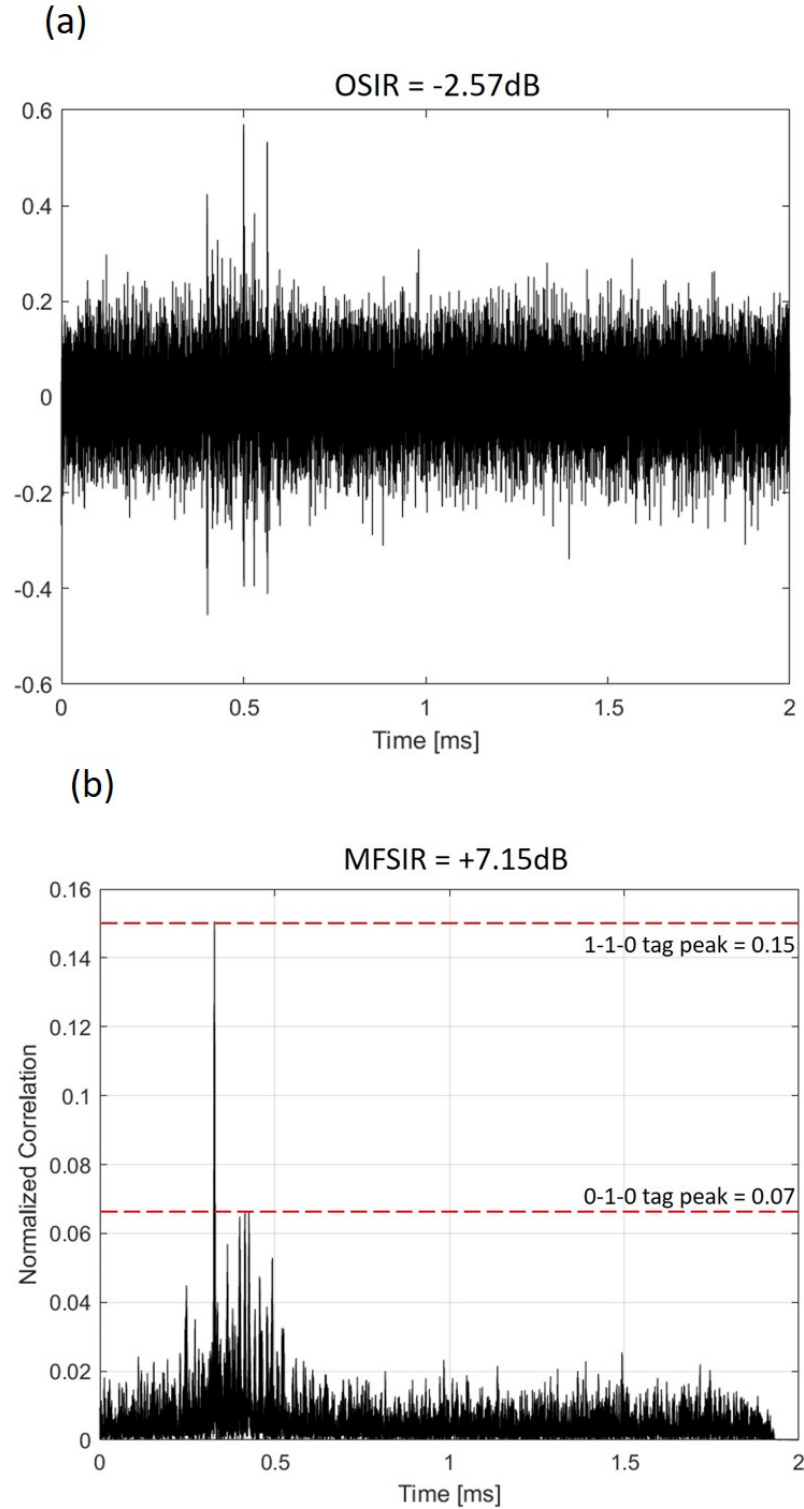


Figure 5.7: a) Simulated signal containing the 1-1-0 and 0-1-0 AID tag signatures, similar to Figure 5.6, but now with additive white noise such that the SNR of the signal is -5 dB relative to the combined power of the two AID tag signatures. The OSIR is -2.57 dB. b) The match filtered output obtained by using a 20% thresholded version of the 1-1-0 template for the case described in (a). The MFSIR is found to be +7.15 dB.

## 5.5 Simulation of an AID tag near a hard shale sediment

In addition to evaluating the detectability of AID tags in the presence of a simulated interferer as in section 5.1, a more realistic simulation of a four fluid-layer AID tag placed near a rough shale seafloor was conducted using k-Wave [69], with the intent of better representing the scattered signal a monostatic SONAR might detect during actual AID tag deployment. The shale bottom is acoustically rigid, and is representative of other acoustically rigid structures and interferers that may produce backscatter that interferes with the AID tag's signature.

In specific, the hemispherical four water-layer AID tag simulated in k-Wave in section 3.3 (see Figure 3.6(b,c)) was placed 2 cm above a rough shale bottom, and a 180 dB SPL explosive monopole pulse (see Figure 3.5) was used as the source signal. The roughness of the shale bottom was modelled as a periodic surface with a fundamental frequency of 30 Hz. The amplitude of the roughness was set to be  $25\lambda$  relative to the upper frequency of the 3 dB-bandwidth of the source signal (here approximately 675 kHz). Furthermore, additive Gaussian noise was added to the roughness profile to provide more realistic small-scale surface variation. Specifying the roughness of the shale bottom in this manner allows for the visualization of scattering from large scale interference structures such as the low frequency carrier profile, while also generating scattering noise. Finally, the simulation environment was spatially discretized to support frequencies up to 1MHz as discussed in section 3.3. Virtual sensors from the center of the tag to the source location are set to collect monostatic scattering data over the course of the simulation. The full simulation environment, source and sensor positions used are shown in Figure 5.8.

The sensor histories over 0.25 ms of simulation time are collected and shown in Figure 5.9. In order to visualize the scattered pressure received at the source location, row 50 (corresponding to sensor number 50 in Figure 5.9) of the sensor histories is sampled. This is in contrast to sampling data from sensor 1 as done in section 3.3 as the highly impulsive

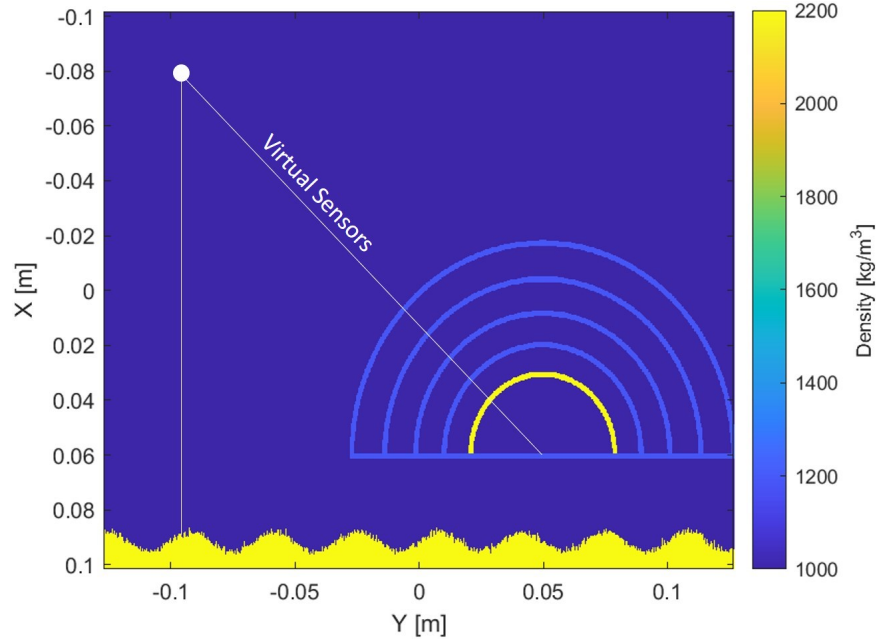


Figure 5.8: k-Wave environment (shown as a density map) used to simulate a four fluid-layer tag (see Figure 3.6(b,c)) near a rough shale bottom (yellow region below the tag). The white point indicates the origin of the explosive monopole source, while the line radially joining the AID tag to the source marks the location of the virtual sensors. The vertical line from the source to the seabed indicates the shortest distance from the source to the seabed.

monopole source used in this simulation generated some numerical noise, making measurements from sensor 1 inadmissible. However, there is hypothetically minimal variation between data collected at sensor 50 and sensor 1 due to their proximity to each other, and therefore data from sensor 50 serves as a viable proxy for the signal received at sensor 1. The time history of sensor 50 is shown in the dotted box in Figure 5.9, and the tag arrivals and interfering signal are clearly marked. The OSIR of this data was found to be -0.7 dB.



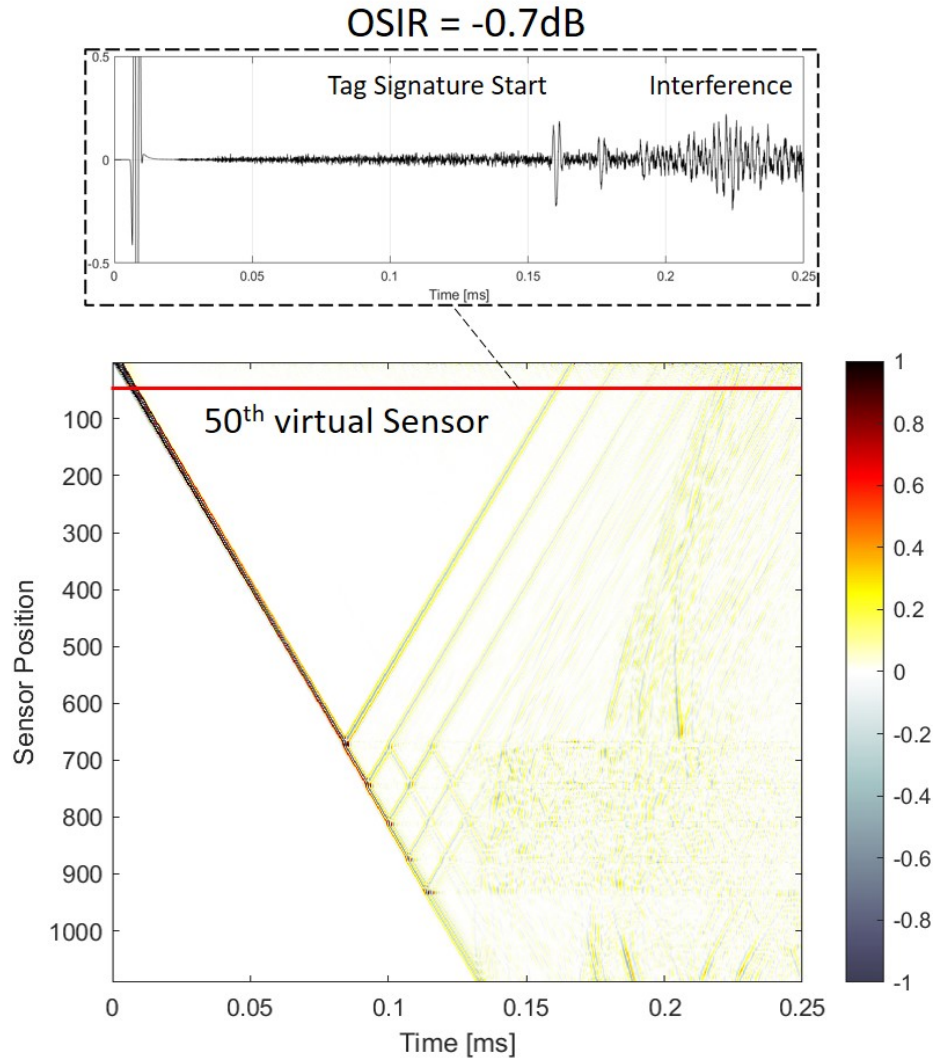


Figure 5.9: Time-histories recorded along the sensor line shown in Figure 5.8 for the four water-layer hemispherically stratified AID tag. Here, the callout box (in dotted lines) shows data collected at the 50th virtual sensor, indicating the source signal, the AID tag signature, and interference from the rough shale bottom. The OSIR of the sensor data is -0.7 dB.

The extracted scattered response from the k-Wave simulation is match filtered using the AID tag signature simulated using the Global Matrix method (shown in Figure 3.9) as the template. Figure 5.10a shows the GMM template aligned with the kWave data at the location of maximum cross-correlation. The match filtered outputs using an unthresholded and thresholded version of the template AID tag signature are shown in Figure 5.10(b,c). The unthresholded template produces an MFSIR of +5.86 dB, while the 20% thresholded template produces an MFSIR of +7.2 dB, corresponding to SIR gains of +5.93 dB and +7.9 dB respectively, and clearly suppressing the interference produced by the shale. In this case, the interfering signal from the shale is separated from the AID tag signature, but the detection performance would be similar in the case where interfering arrivals more adversely return the AID tag's signature as well, as demonstrated in section 5.4.

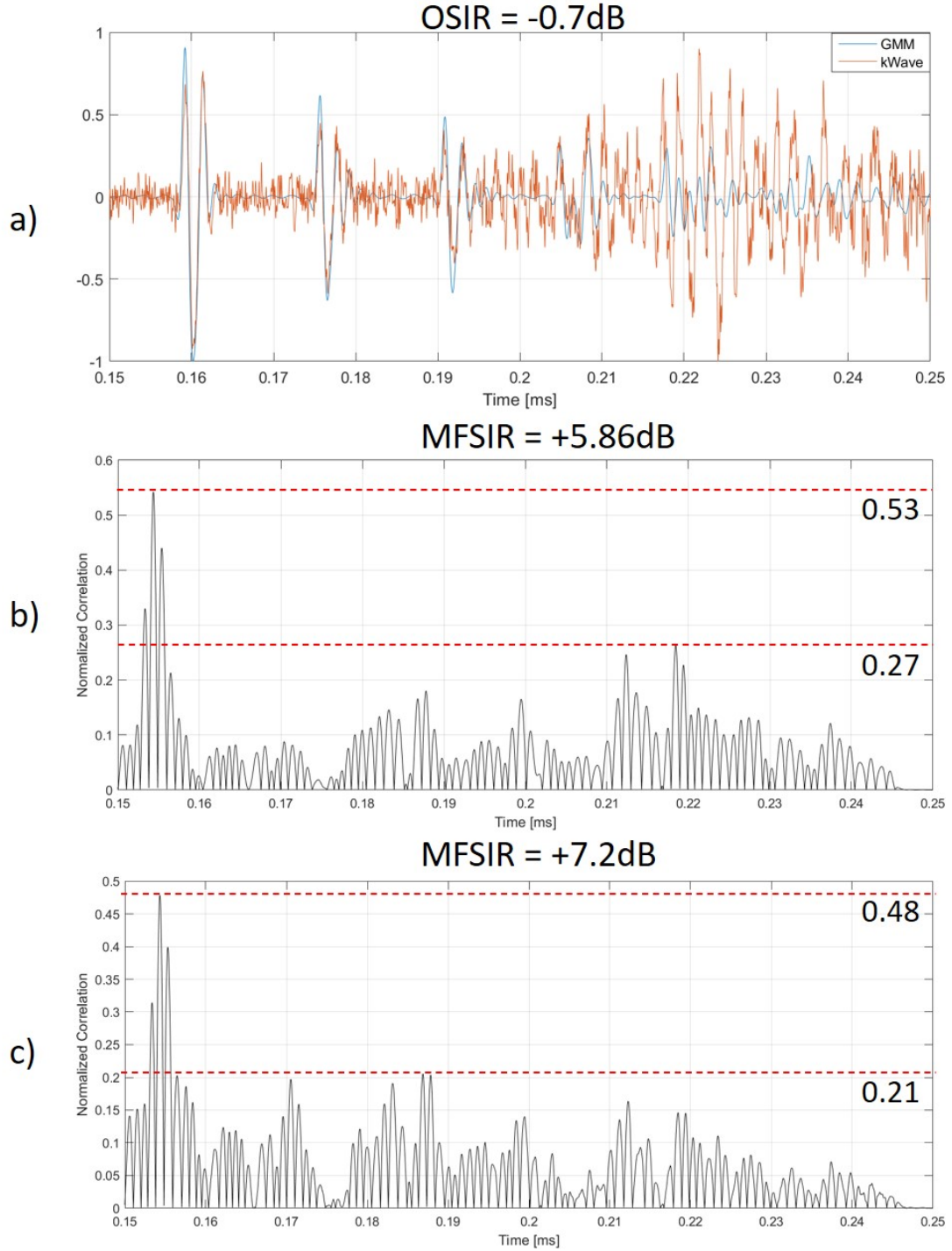


Figure 5.10: a) Overlay of the four water-layer AID tag template simulated using the global matrix code (GMM), and the backscattered signal extracted from the k-Wave simulation of a four water-layer AID tag near a rough shale surface. b) The match filtered output of the kWave simulation data using the GMM template without any thresholding. The computed MFSIR is +5.86 dB. c) The match filtered output of the kWave simulation data using the GMM template thresholded to 20% of its maximum amplitude. The computed MFSIR is +7.2 dB.

## 5.6 AID tag detection range

In addition to the detection of an AID tag signature in the presence of interference and other AID tags, a back-of-the-envelope upper bound on the range of tag detection is also computed using the Sonar Equation Calculator Toolbox available in Matlab (Mathworks, Natick, MA). For the case of monostatic sensing as in an AUV, the SNR of a target signal as received by the vessel is governed by the active SONAR equation [79] given by

$$SNR = SL - 2TL - (NL - DI) + TS \quad (5.6)$$

where  $SL$  is the source level,  $TL$  corresponds to the one-way transmission loss across the water channel due to spherical spreading,  $DI$  the directivity index of the receiver (also called array gain), and  $NL$  the noise level at the receiver. All quantities in Equation 5.6 are expressed in dB. The Sonar Equation Calculator uses the active SONAR equation to compute the maximum range from which an acoustic target (here, an AID tag) can be detected with a specified SNR threshold. Selection of the input parameters to the toolbox for the active SONAR equation solution is discussed below.

There are four aspects that need to be considered in the specification of the range at which an AID tag can be detected for a given source level (here 200 dB re  $1\mu\text{Pa}$ ), namely the characteristics of the receiver elements used to detect the AID tag signature, the target strength of the AID tag itself, the characteristics of the source signal, and propagation environment. As an example, the four-water layer hemispherical AID tag simulated in section 3.3 is used to define the AID tag properties, while receiver properties are taken from the datasheet of a Starfish 452F sidescan SONAR [80], as this hardware was used for experimentation as will be discussed in chapter 6. It is to be noted that a wider source bandwidth than that of the Starfish 452F is used in the following range simulations (i.e. a fractional bandwidth of 0.75 as compared to 0.08) to accommodate the four water-layer tag design used. AID tags in this work are assumed to operate in shallow water with column

depth of 50m.

### 5.6.1 Receiver based parameters

The receiver array geometry defines the  $DI$  or array gain of the SONAR system. For the Starfish 452F that has a line array receiver, the array gain is given by

$$DI = 10 \log_{10} \frac{2L}{\lambda} \quad (5.7)$$

where  $L$  is the characteristic array length, and  $\lambda$  the wavelength of the center frequency of the source (450 kHz here). The value of  $L$  can be estimated from the manufacturer specified 3 dB half-beamwidth of  $\theta_{3dB} = 30^\circ$  as

$$L = \frac{25.3\lambda}{\theta_{3dB}} = 2.8\text{mm} \quad (5.8)$$

from which  $DI$  can be computed using Equation 5.7 as 2.25 dB. Underwater ambient, reverberant, and electrical interference noise can contribute to the  $NL$  specification. In this work, the full characterization of underwater noise-levels is not carried out, and  $NL$  is specified to between a range of [73, 100] dB re  $1\mu\text{Pa}$ .

### 5.6.2 AID tag based parameters

The reflective properties of the AID tag contribute to the target strength  $TS$  parameter in the active SONAR equation. Here, the target strength is defined in [81] by the relation

$$TS = 10 \log_{10} \frac{\sigma^{back}}{4\pi} \quad (5.9)$$

expressed in dB re  $\text{m}^2$ , where  $\sigma^{back}$  is the backscattering cross-section (BSX) of the AID tag. The backscattering cross-section is defined as the ratio of backscattered to incident acoustic intensity, which varies for different types of scatterers [81]. Using the expression for high frequency backscattering intensity for a rigid sphere, scaled by the wideband power

reflection coefficient of 0.23 (from Figure 4.3c) of the outermost acrylic shell with radius 12.6 cm, the BSX of the four water-layer AID tag is found to be

$$\sigma^{back} = R_{\Pi} \pi a^2 = \pi \cdot 0.23 \cdot 0.126 = 0.0912 \quad (5.10)$$

therefore providing a target strength of -21.39 dB upon substitution of  $\sigma^{back}$  in Equation 5.9. To this, the additional MFSIR gain of +11 dB obtained from Figure 5.3c for a four-layer tag assuming a conservative 30% template threshold is added with a 3 dB margin, providing an AID tag target strength of  $-21.4 + 11 - 3 = -13.4$  dB.

Computing the target strength in this deterministic manner only provides an average  $TS$ , and does not take the variability of the BSX into account however. The fluctuation of the BSX between measurements is therefore represented by statistical models developed by Peter Swerling [82], where different types of scatterers have been documented to follow different probability distributions of BSX variation. AID tags are assumed to follow a Swerling 3 model i.e. a target whose BSX is assumed to fluctuate slowly over time, and potentially changes only on a scan-to-scan basis from possible AUV positioning variations. In this model, the probability density of BSX variation is governed by a Chi-squared distribution given by

$$p(\sigma) = \frac{1}{\sigma_{Av}} e^{-\sigma/\sigma_{Av}}, \sigma > 0 \quad (5.11)$$

where  $\sigma_{Av}$  is the average BSX, and  $\sigma$  the fluctuating BSX and  $p(\sigma)$  the probability distribution for the variation of  $\sigma$ . For further details, the reader is directed to [82] for the full theory behind Swerling models.

In addition to Swerling model specification, the Sonar Equation toolbox also accepts probabilities of detection and false alarm to compute the SNR required at the receiver for an AID tag detection following those probabilities. As AID tags assist in navigation, it is desirable to minimize false alarms while maintaining high probabilities of detection. With

this in consideration, the probability of detection is set to 0.97, and the probability of false alarm is set to 0.001.

Using the parameters discussed, the four water-layer tag can theoretically be detected at a range of 34 m with a 97% probability of detection, and a 0.1% false alarm rate. The full table of simulation parameters and computed range for the detection of a four water-layer AID tag is given below:

Table 5.2: Simulation parameters used to compute the range at which a four water-layer AID tag can be detected.

Parameter	Value
Noise Level [dB re $1\mu\text{Pa}$ ]	100
Directivity Index [dB]	2.25
Target Strength [dB]	-13.4
Upper Frequency Bound [kHz]	618.75
Channel Depth [m]	50
Source Level [dB re $1\mu\text{Pa}$ ]	200
Probability of Detection	0.97
Probability of False Alarm	0.001
Swerling Model	3
<b>AID Tag Range</b>	<b>34.2m</b>

## 5.7 Chapter Summary

This chapter demonstrated AID tag signature detectability in the proximity of strong interference and other AID tags using match filtering. Thresholding the known AID tag templates used to match filter data containing the tag signature and interference (or another AID tag) was shown to greatly increase the SIR of the match filtered output. Simulations of an AID tag placed near a rough seabed demonstrated the detectability of a tag in more realistic, reverberant environments. Furthermore, AID tag signatures from different tags were shown to decorrelate to a greater extent when thresholded versions of these templates were used. Finally, a range of detection was specified for AID tags using the active SONAR equation.

## CHAPTER 6

### AID TAG EXPERIMENTS IN THE SONAR REGIME

Finally, as a proof of concept of AID tag operation using a conventional interrogating SONAR, experiments were conducted in the Acoustic Water Tank facility at the Georgia Institute of Technology [83]. A Starfish 452F high-frequency sidescan SONAR [80] by Tritech (Aberdeenshire, Scotland) whose ensonification waveform was a  $400\ \mu\text{s}$  Linear Frequency Modulated (LFM) pulse with a bandwidth of 40 kHz, centered at 450 kHz was used to ensonify AID tags fabricated for this frequency range. This very basic side-scan SONAR was only selected to provide a proof of concept based on hardware availability, especially as it was shown in chapter 5 that using a broadband source would outperform this narrowband source. The Starfish had a  $60^\circ$  vertical beamwidth and  $0.8^\circ$  horizontal beamwidth which was factored while positioning the SONAR and AID tags. The spatial resolution of the SONAR given its source characteristics was about 1.8 cm from Equation 4.7, assuming the sound speed in water to be 1480 m/s, which placed a limit on the minimum fluid layer thickness that could be used in building AID tags for this SONAR.

The SONAR was mounted onto a computer controlled 4-axis (X-Y-Z-azimuth) traverse mechanism and immersed into the ( $40' \times 20' \times 24'$ ) water tank. An off-board, manufacturer provided set top-box was used to control the LFM transmit (Tx) signal from the port side of the SONAR, while the port side receive (Rx) signal was routed from the top-box to a National Instruments (Austin, Texas) NI-5133 High Speed Digitizer and sampled at 25 MHz or 50 MHz over different experimental trials. The full data acquisition and processing pipeline is shown in Figure 6.1.

The fabricated AID tags were interrogated using the SONAR, and the AID tag signatures measured were analyzed to demonstrate the capability of detecting an AID tag with a known template in the midst of interference, and to show the uniqueness of AID tags with



different layering properties in this frequency regime.

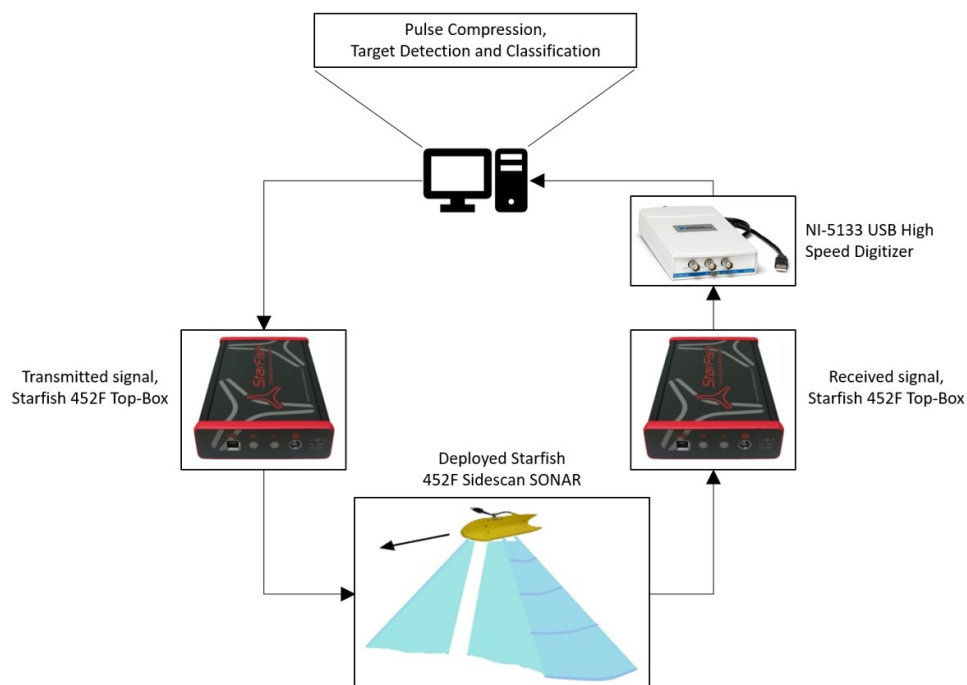


Figure 6.1: The data collection pipeline used during experimentation.

## 6.1 Calibration of the Starfish 452F SONAR

Before any tag detection algorithms were run, raw data collected from the digitizer were pulse compressed. The technique of pulse compression is commonly used in underwater imaging. In brief, the SONAR transmits an LFM pulse to interrogate the environment. The resulting reflected signal is collected by the receiver on board the vessel, and is match filtered using the known LFM pulse transmit waveform. Copies of the LFM pulse present in the reflected signal show up as peaks in the match filtered output, while ambient noise is suppressed. This match filtered signal can then be used in post-processing. One thing to note however is that the performance of the pulse compression process is only as good as the LFM template used in match filtering the raw data. Typically, SONAR systems come with multi-tap filterbanks which perform the pulse compression operation on custom hardware, and do not make the template used for pulse compression available. Furthermore,

the National Instruments digitizer used in the data acquisition clipped the original high amplitude transmit signal sent by the SONAR in the recorded data, therefore potentially making this clipped signal unviable as a candidate for the pulse compression template. Due to these issues, it therefore became necessary to characterize the transmit signal used by SONAR before testing any AID tags.

For this purpose, the SONAR was immersed 6 ft underwater in the empty (i.e. not containing an AID tag) acoustic water tank, and a transmit pulse was triggered from the portside Tx transducer element of the SONAR. The recording window was set to approximately 15 ms to allow for the transmit pulse to reflect from the walls of the tank, and arrive at the receiver. The received signal therefore contained copies of the true transmit signal sent by the SONAR, which were recorded as unclipped signals by the digitizer as they were attenuated to levels below the digitizer's saturation limit. For better visualization of this process, a spectrogram (time-frequency plot) of the raw data collected in this baseline experiment is shown in Figure 6.2. Here, the 400  $\mu$ s source signal is indicated in the white box labelled (a), and is an upward LFM signal in the [430, 470] kHz frequency band. The wall reflections from the tank arrive from the 6 ms mark onwards as indicated. In order to accurately estimate the transmit signal, a wall reflection which was well separated from other reflections, such as the one marked in the white box labelled (b) was used.

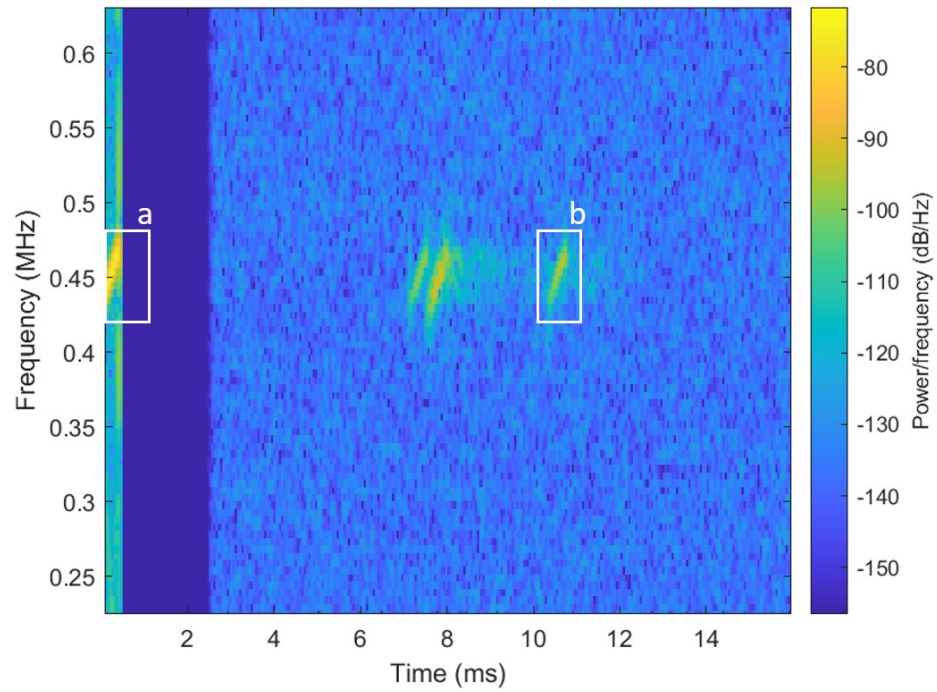


Figure 6.2: A spectrogram of the baseline experiment conducted in the acoustic water tank. The portside element transmits an LFM signal marked as (a) in the figure, while the wall reflections are copies of (a) arriving at different times. A well separated wall reflection such as (b) is used to estimate the true transmit signal sent by the SONAR.

Finally, the frequency spectra of the extracted signals marked in Figure 6.2, i.e. the transmit signal as recorded by the receiver at  $t = 0$  ms, and the wall reflection marked in box (b) are compared with each other as shown in Figure 6.3. Figure 6.3a shows the original spectrum of the transmit signal from box (a) in Figure 6.2 as the black line. While the frequency spectrum between [430, 470] kHz is the known LFM spectrum, there are additional high frequency distortion components due to the clipping of the transmit signal. In order to remove the distortion effects, a hamming window was applied over the [400, 500] kHz band as shown by the dotted red line in Figure 6.3a. To verify that this windowed version of the Tx signal could serve as a valid template, the spectrum of the wall reflection (shown in black in Figure 6.3b) was also windowed over the same frequency range, and the phases of both windowed spectra were compared using standard cross-correlation as defined in Equation 2.33. The correlation coefficient between both the windowed Tx signal and the wall reflection was found to be 0.92, indicating excellent agreement between the two signals, suggesting that it was possible to use the windowed Tx signal from box (a) of Figure 6.2 as the template for pulse compression of all future recorded data.

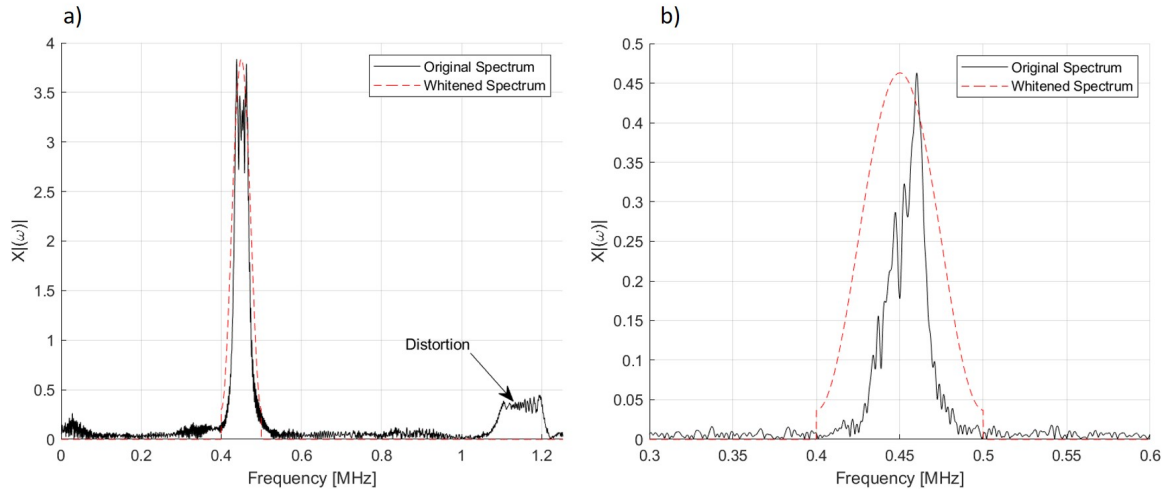
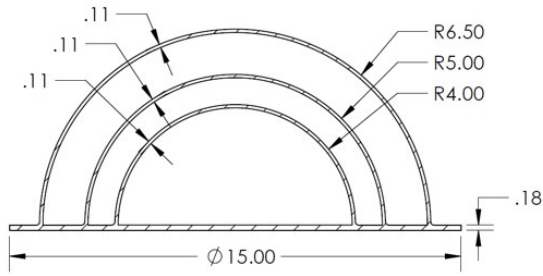


Figure 6.3: a) The magnitude spectrum of the transmit signal indicated by box (a) of Figure 6.2. The black line indicates the original spectrum, while the red dotted line shows the hamming window applied to the magnitude spectrum of the signal. b) The magnitude spectrum of the wall reflection indicated by box (b) of Figure 6.2. The black line indicates the original spectrum, while the red dotted line shows the hamming window applied to the magnitude spectrum of the signal.

## 6.2 Tag Fabrication

One and two water layer AID tags were designed and manufactured for use with the Starfish 452F SONAR. Three commercially available (SupremeTech, fulfilled by Amazon.com) 2.8 mm thick flanged hemispherical acrylic shells with outer diameters of 13 in, 10 in and 8 in respectively were selected, which when nested, created two fluid layers with thicknesses of 3.53 cm (1.4 in) and 2.3 cm (0.9 in) that satisfied the SONAR's spatial resolution constraint. The shells were bolted onto a 15 in diameter laser-cut acrylic backing plate (see Figure 6.4). The ideal tag design would contain a hemispherical metal core, or metal backing plate but the flat acrylic backing plate was selected here for ease of manufacturing and testing. Different AID tags could be obtained by permuting through the permissible shell layering combinations i.e. by removing one or both of the inner shells as discussed in chapter 5. This allowed for the testing of four different AID tags - a 13 in-10 in-8 in tag, a 13 in-10 in tag, a 13 in-8 in tag, and a 13in tag. Here, the tag names are specified based on the diameters of the shells used to construct them. 1 mm thick washers (not shown in drawing (Figure 6.4a)) were placed between the flanges of the shells and the backing plate to provide a gap for water ingress into the layers of the tag upon immersion. Provision was made on the backing plate to attach the tag to a mounting bracket or hook so that it could be suspended underwater for testing. The key consideration in the design of the mounting mechanism was that it should minimally interfere with the scattered response from the tag. Acoustically transparent ropes, nets, and brackets can also be designed based on the tag's application.

(a)



(b)

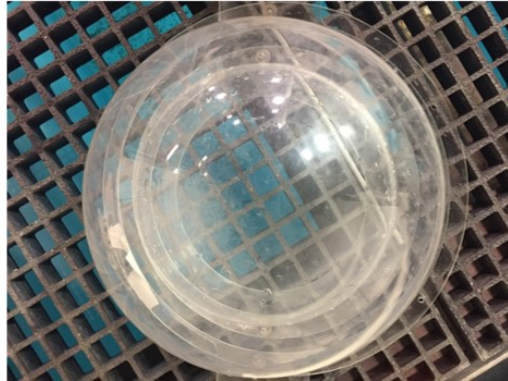


Figure 6.4: a) Dimensions (in inches) of the two water layer AID tag deployed for a SONAR source with center frequency 450 kHz and 40 kHz bandwidth. The sections between the shells get filled with water upon immersion. Other tags can be obtained by removing one or both of the inner shells of the tag shown. b) Constructed AID tag with two fluid layers enclosed within three nested acrylic shells of outer diameters 13", 10" and 8" respectively.

### 6.3 AID tag response measurements

The fabricated 2 layer AID tag (or any other AID tag permutation) was suspended 5 ft below the water surface using a custom mount which attached to the tag's backing plate. The SONAR was placed at the same depth at a distance of 6 ft from the tag and was oriented such that its beam was incident on the horizontal diameter of the tag, in order to mimic as much as possible, the insonification of the tag from an omnidirectional source. Figure 6.5a shows a schematic of the tag-SONAR setup, where the outermost tag layer and flange are indicated in the top view and projected onto the front view as two concentric circles. The shaded triangle in the top view indicates the SONAR's horizontal field of view corresponding to the  $60^\circ$  beamwidth, while the thin shaded rectangle in the front view indicates the  $0.8^\circ$  beamwidth.

For the current tag-SONAR configuration, two types of returns have been observed as mentioned earlier, and are marked in Figure 6.5 as 1 and 2, corresponding to the tag signature and the radially diffracted rays from the backing plate respectively. The signal received by the SONAR will therefore be a combination of the tag signature and delayed and attenuated versions of the source pulse based on the distance of the SONAR to the flanges. If the SONAR is placed on the axis of symmetry of the tag, the reflected rays from the flange arrive at the SONAR at the same time, and coherently sum. If the SONAR is offset from the axis of symmetry, the differences in flange reflections can indicate the bearing of the SONAR relative to the AID tag. In this manner, the presence of the flange return can be exploited as it is essentially an energetic return without any additional impedance-mismatch based losses, with a predictable time-of-arrival. The combined (tag + flange return) based template can therefore greatly enhance the detection of a tag even when the backing plate used is not a rigid material as will be shown in a section 6.4.

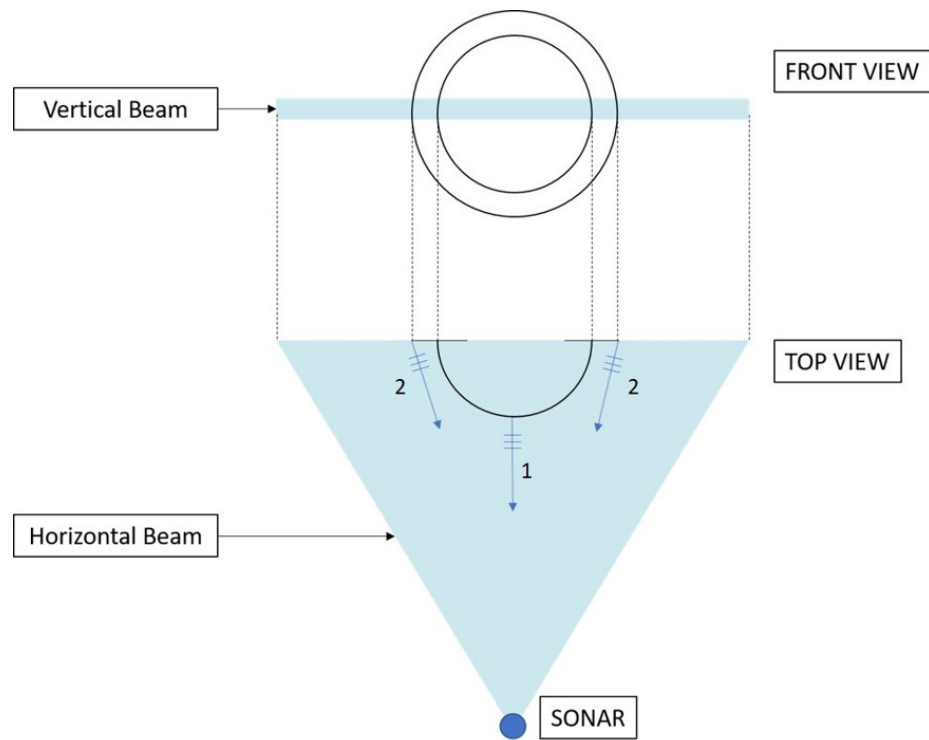


Figure 6.5: Schematic of experimental setup. The tag is placed in the within the beamwidth (shaded area in top view) of the SONAR. Two types of signals (marked by 1, and 2 in figure) are reflected by the tag and correspond to the layer signature of the tag and the diffracted rays from the flange, respectively.



As an example data acquisition, the backscattered signature from the two water layer AID tag shown in Figure 6.4(a, b) was measured. Prior to match filtering, the raw waveform received is as shown in Figure 6.6.

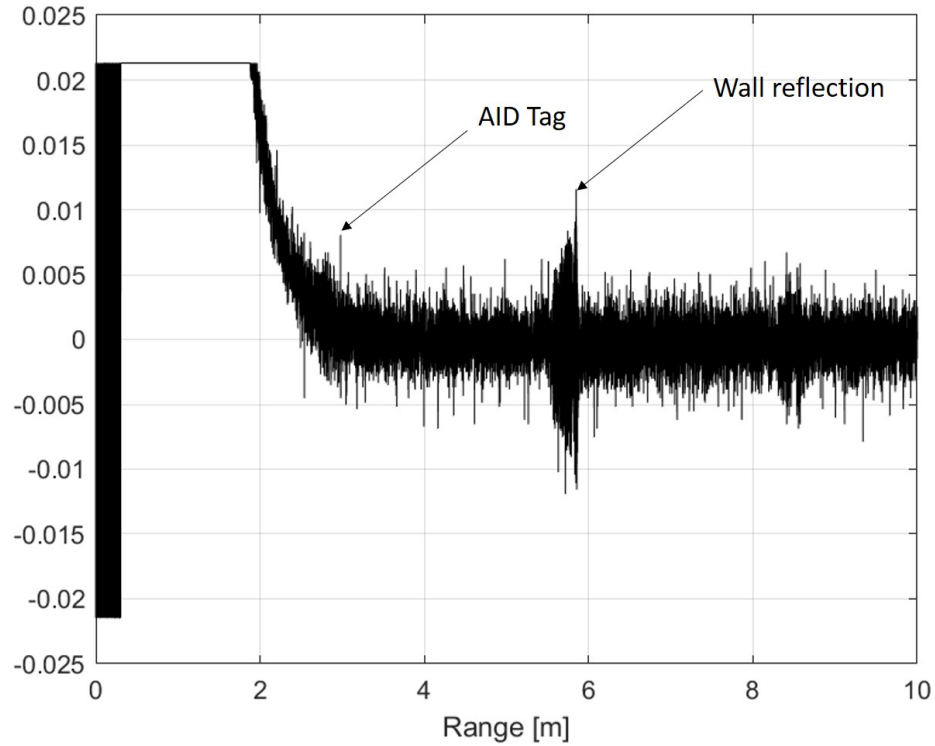


Figure 6.6: Raw data received by the SONAR, prior to match filtering, for the two water layer tag shown in Figure 6.4.

Using the LFM template extracted from the baseline reading (see Figure 6.2 and Figure 6.3a), the raw data is pulse compressed. The envelope of the output of the pulse compression shows peaks where the LFM template correlate highly with the raw data, as shown in Figure 6.7a. The AID tag signature is present at approximately 2.5 m from the SONAR, consistent with the experimental setup, and a strong wall reflection is observed at approximately 5.5 m distance. The OSIR of this data is found to be -21.53 dB. Using a 20% thresholded AID tag template extracted from Figure 6.7a between the [2.5, 2.9] m range marks, the pulse compressed signal in Figure 6.7a is match filtered to obtain Figure 6.7b. Here, the 'self-experiment' AID tag template (i.e. a template extracted from the reading to be match filtered) is used to demonstrate the SIR gain possible for an AID tag if the AID

tag template is selected appropriately. Specifically, the MFSIR of Figure 6.7b is found to be -13.27 dB, corresponding to an SIR gain of +8.26 dB, consistent with the SIR gains expected from a two fluid layer tag with no rigid backing plate (as indicated in Figure 5.2). It is to be noted that this experiment was an early trial of AID tag testing underwater, and the transmit signal power settings of the SONAR have since been increased to get stronger returns from an AID tag, as will be shown in section 6.4.

Furthermore, by zooming in on the AID tag signature portion of Figure 6.7a between the [2.3, 3.2] m range marks, it is possible to identify the reflections from the different layers of the AID tag, and flange(or backing plate) as marked in Figure 6.8. The arrivals from the different shells of the AID tag are clearly demarcated, and the distance between each shell return is within 5% of the theoretical value computed from the difference in adjacent shell diameters.

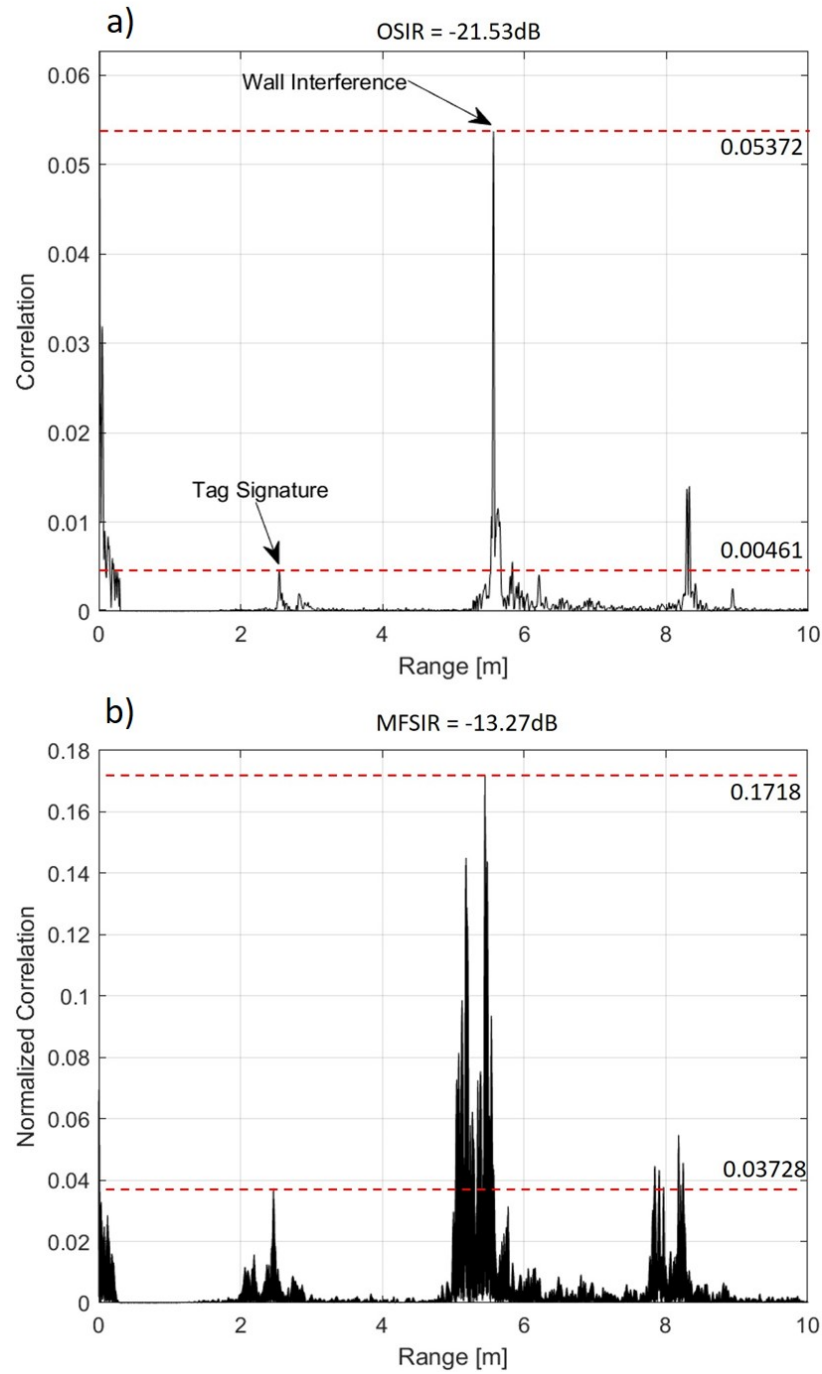


Figure 6.7: a) The pulse compressed output of the raw data shown in Figure 6.6, using the hamming windowed template estimate of the transmit signal. The AID tag signature for the two water layer tag shown in Figure 6.4, and a strong wall reflection is marked. The OSIR of this data is found to be -21.53 dB. b) The match filtered output of (a) using a 20% thresholded copy of the two water layer template extracted from the same measurement. The MFSIR is found to be -13.27 dB.

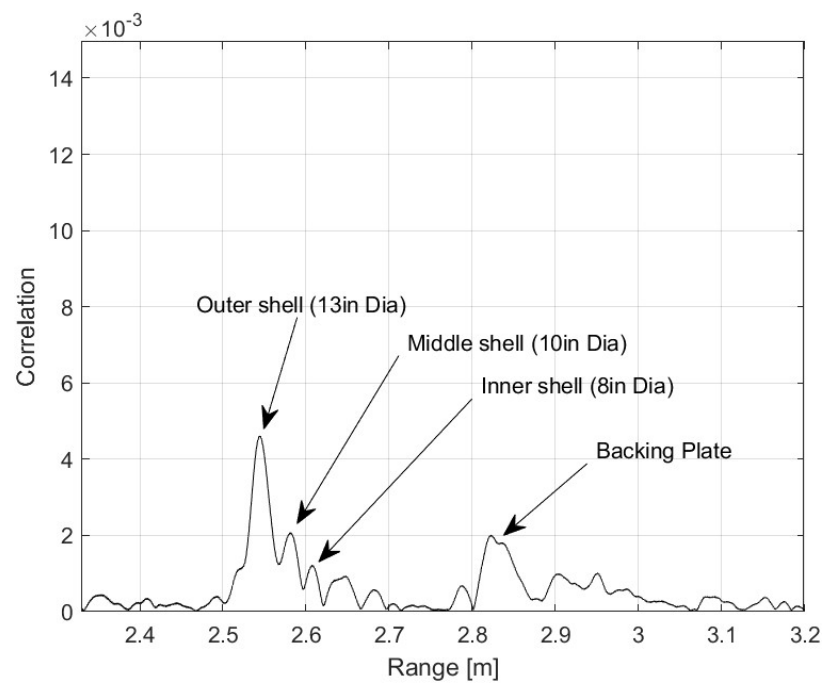


Figure 6.8: The AID tag signature structure of the two water layer tag, where the returns from the shell layers and backing plate comprising the tag are marked.

The experiment is repeated for the remaining tag configurations, and the four possible tag signatures obtainable using three hemispherical shells is shown in Figure 6.9. Again, there is less than 5% error in the relative position of the peaks in each of these tag signatures when compared to the theoretical peak distances obtained from the differences in the shell radii.

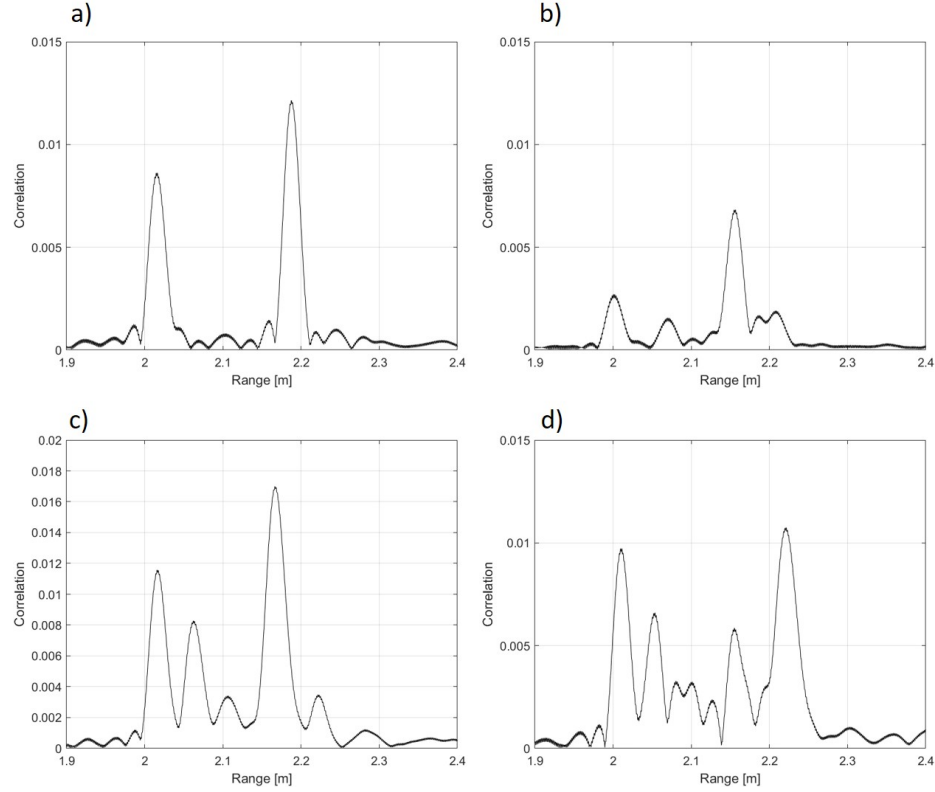


Figure 6.9: a) AID tag consisting of a single 13in Diameter shell b) AID tag consisting of a 13in and 8in Diameter shell c) AID tag consisting of a 13in and 10in Diameter shell d) AID tag consisting of a 13in, 10in and 8in Diameter shell.

#### 6.4 Cross trial performance of AID tag templates and observations

Finally, to demonstrate the use of an AID tag template across different data acquisitions, the two layer fluid tag was interrogated multiple times by the LFM pulse using the SONAR-tag configuration described previously, and each trial was pulse compressed using the windowed source signal estimate. Figure 6.10a shows an example experimental trial after pulse

compression. The signal marked in the rectangular box is the tag response, and the strong later arrivals (after the 6 ms mark) correspond to wall reflections from the tank. It is to be noted that the tag signature comprises of two components - the AID tag response from the layers of the tag (between 3.5 ms and 3.75 ms), and an additional reflection from the flanged backing plate at approximately 4 ms.

The boxed signal in Figure 6.10a containing the (tag + flange) response is extracted and stored as an AID tag template and is shown in Figure 6.10b. The template is thresholded to 20% of its maximum amplitude and cross-correlated with the 'self-experiment' signal shown in Figure 6.10a to obtain the match filtered output shown in Figure 6.10c. Here, the threshold value is selected based on the trend observed in Figure 5.2c for a two-layer tag. While the ideal thresholding value is suggested to be 10% the peak template amplitude, a margin of 10% is provided so that the template is robust across different experimental trials and not as sensitive to measurement noise artefacts (which also get amplified by the thresholding operation). Using the extracted template, an SIR gain of +10.46 dB is observed, boosting the original SIR of -11.77 dB to an MFSIR of -1.31 dB such that after matched-filtering the tag signal is nearly as strong as that of the wall signal. The +10.46 dB gain observed in the experiment is an excellent compression gain, and comes close to suppressing signals close to 5 times the AID tag's peak amplitude.

To quantitatively demonstrate the advantage of the thresholded (tag + flange) template over unthresholded templates, or templates containing only the tag response, the SIR gains for different cases of templates with and without the flange return, and varying threshold values are shown in Table 6.1. Clearly, the match filtered gains of a 10% thresholded template including the flange return offers the best SIR gains relative to all other cases. Furthermore, as demonstrated in Figure 5.2c, a template with 50% threshold performs worse than the 10% for both the flanged and unflanged templates. Additionally, an unthresholded tag template with the flange outperforms all templates which exclude the flange return (thus providing the option to reduce the complexity of the tag's template signature if desired).

The extracted template is now used to match-filter a different trial of the experiment (see Figure 6.10d). With all other experimental conditions the same, it is intuitive that the stored template would offer similar compression gains. The match filtered output of the 'cross-experiment' signal with the template (also thresholded to 20% its peak amplitude) is shown in Figure 6.10e and indicates an SIR of -1.39 dB corresponding to an SIR gain of +10.34 dB which shows the consistency of the template over different trials. This result can be considered as representative of an upper bound on the inherent experimental variability associated with any field deployment. Additional testing of AID tag template robustness is left as future work.

Table 6.1: SIR gains for an experimentally collected two-layer AID tag template iterated through thresholding values and the use of the flange reflection. The OSIR of the data before match filtering is -11.77 dB (see Figure 6.10a)

Template Type	Match Filtered SIR (dB)	SIR Gain (dB)
Flange + 10% Thresholding	-1.24	10.53
Flange + 20% Thresholding	-1.31	10.46
Flange + 50% Thresholding	-1.79	9.98
Flange + Unthresholded	-3.41	8.36
No Flange + 10% Thresholding	-4.21	7.56
No Flange + 20% Thresholding	-4.16	7.61
No Flange + 50% Thresholding	-4.12	7.65
No Flange + Unthresholded	-5.01	6.76

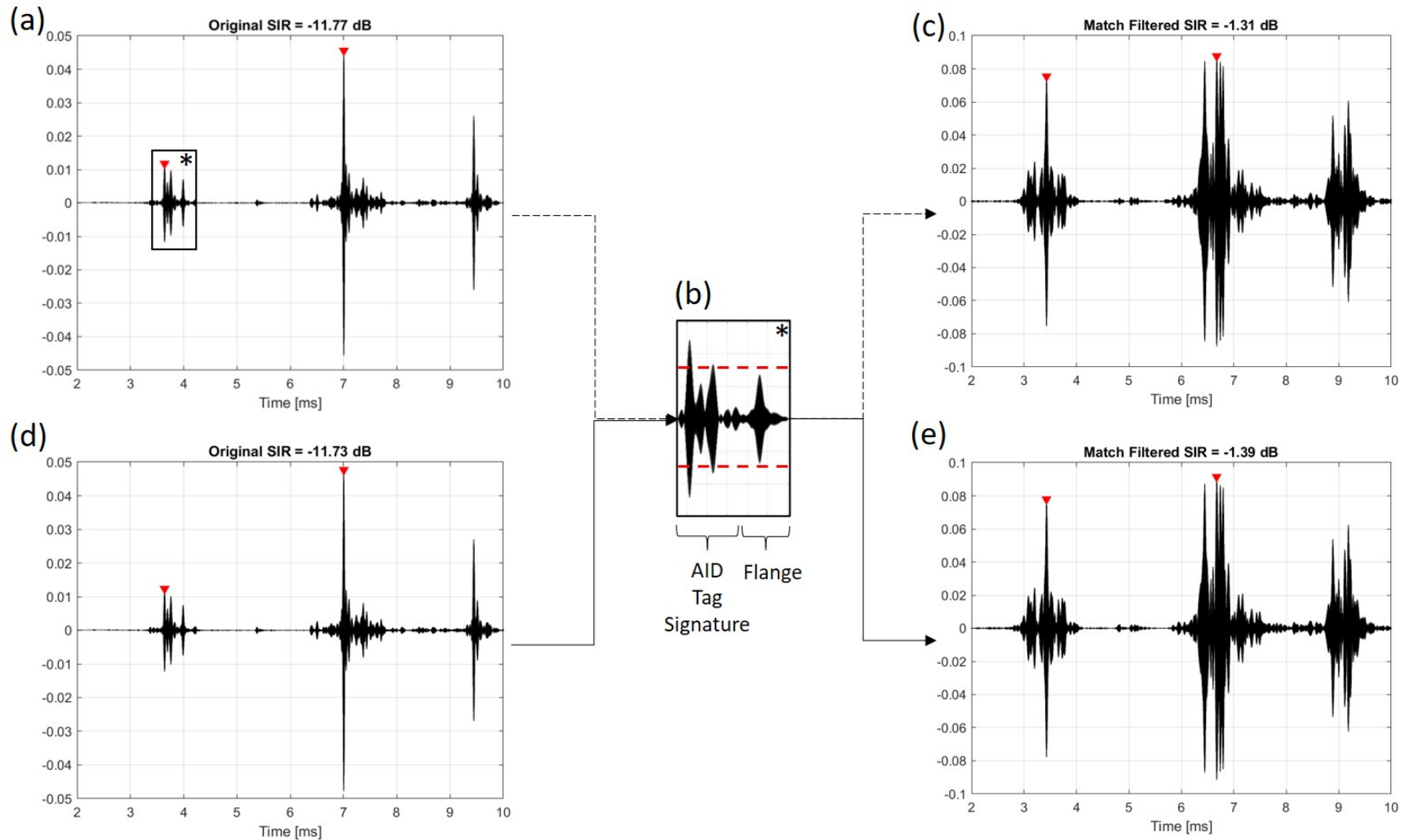


Figure 6.10: a) Measured reflections obtained from interrogating the two-layer tag shown in Figure 6.4b placed near a hard wall, using the Starfish 452F SONAR maintained at a range of 6 ft from the tag, at the same depth of 5 ft. The AID tag template shown in the box in (a) is extracted from the response and includes the tag signature as well as the flange reflection (respectively marked as echo 1 and 2 in Figure 6.1). The SIR is computed using the peak amplitudes of the signal and interferer (triangle markers). b) Zoomed in version of the template extracted from (a), optionally thresholded to a 20% saturation level(dotted line) before match filtering. The \* indicates the portion of the template corresponding to the flange return. c) Using a template thresholded to 20% of the maximum amplitude of the template, the “self-experiment” match filtered response has a final SIR of -1.31 dB (SIR Gain = 10.46 dB). d) Another scattered response realization using the same SONAR-Tag configuration as in a. e) Using the template shown in (b) thresholded to 20% of the maximum amplitude of the template, the “cross-experiment” match filtered response has a final SIR of -1.39 dB (SIR Gain = 10.34 dB) thus showing good repeatability of the measurement procedure.



## **6.5 Chapter Summary**

This chapter discussed the results of AID tag experiments conducted in the Acoustic Water Tank facility at The Georgia Institute of Technology. A method of SONAR calibration (i.e. extracting a transmit signal template for pulse compression) using wall reflections from a reverberant water tank was discussed. The response of hemispherical AID tags with one or two water layers were measured to demonstrate AID tag signature uniqueness. Furthermore, the robustness of an extracted AID tag template was examined using cross-experimental trials.

## **CHAPTER 7**

### **FUTURE WORK AND CONCLUSIONS**

#### **7.1 Summary**

This work provided the design and experimental validation of passive underwater Acoustic IDentification (AID) tags that have unique, detectable acoustic backscattering signatures, which may be used as navigational aids for AUVs.

Specifically, Chapter 2 provided simulation and experiment based validation of using stratified layers of acoustic materials of varying thickness (akin to an optical barcode or SAW RFID tag) to generate a uniquely detectable AID tag signature.

Chapter 3 extended the analysis of Chapter 2 to the design of AID tags with spherical symmetry so that the AID tag signature is omnidirectional, and demonstrated through simulations and experiment that the scattered AID tag signature from a hemispherically stratified tag can simply be approximated in the high-frequency regime by the signature generated by an equivalent horizontally stratified tag.

Chapter 4 introduced an energy based tag design optimization strategy and provided design recommendations and analyses for AID tags operating in specific frequency regimes.

Chapter 5 recommended a method of match filtering using thresholded AID tag templates, and demonstrated the detectability of an AID tag signature from arbitrary interfering signals, other AID tags, and from hard sediment or clutter that may be in the tag's proximity during deployment.

Chapter 6 provided experimental results of an AID tag manufactured for high frequency SONAR, and demonstrated tag detectability in the presence of strong interference from a hard wall (a proxy for the seafloor for example).

## 7.2 Contributions to the Literature

The specific contributions of this work to the Literature are repeated from chapter 1 below for completeness:

1. The acoustic signatures of AID tags made of horizontally stratified layers of acoustically dissimilar layers were simulated and experimentally verified using a subscale ultrasound setup.
2. The compressional acoustic velocity and attenuation of common viscoelastic materials were experimentally obtained and reported.
3. High frequency specular scattering from AID tags with multiple spherically and hemispherically stratified layers were shown through numerical simulations to be equivalent to the response from a horizontally stratified AID tag. The simulations also indicated the azimuthal invariance of the backscattered response. Furthermore, the backscattered response of an AID tag assembled using two SLA manufactured, concentrically placed, calibrated hemispherical shells, was experimentally obtained using a sub-scale ultrasound setup and validated to be azimuthally invariant, and consistent with numerical simulation.
4. An energy based AID tag design optimization scheme was introduced, and an optimal AID tag layering scheme has been specified.
5. A detectability analysis of AID tag signatures in the presence of interference was conducted, and tag template thresholding strategies to boost the signal-to-interference ratio of the AID tag have been recommended. Additionally, a back-of-the-envelope detectability range has been provided using the active SONAR equation.
6. AID tags designed for high frequency SONAR were experimentally tested and it was shown that tag signatures could be detected in highly reverberant conditions using extracted AID tag templates.

The contributions listed have been published (or are in preparation) as the journal papers listed below:

1. "Passive underwater acoustic tags using layered media", *The Journal of the Acoustical Society of America*, 2019[45].
2. "Omnidirectional passive acoustic identification tags for underwater navigation", *The Journal of the Acoustical Society of America*, 2020[54].
3. "Passive underwater Acoustic IDentification tags using multi-layered shells" (*in preparation*)

### **7.3 Future Work**

The AID tags so developed in this work represent a class of passive underwater acoustic markers that may be used by AUVs as navigational tools. While this thesis presents a fairly thorough analysis and proof of concept of the operation of AID tags, there is certainly scope for additional testing and new research directions based on this work.

With regard to the current design iteration of AID tags, more extensive testing of the tags manufactured in chapter 6 in a lake or other body of water using high frequency, rotary SONAR would provide data from real-time deployment. While AID tags near an interferer or clutter have already been simulated and experimentally tested in a laboratory setting with conclusive insights on tag detection, these additional data points can be used to develop tag templates that are more descriptive of the AID tag's scattering profile in the real world. As an extension to this idea, a completely data-driven approach to template generation and AID tag detection can be taken, rather than relying on simulated template waveforms.

The work presented here constitutes one possible realization of a passive AID tag design, inspired by the design of SAW RFID tags. With the same basic design constraints used for AID tag design in this work, i.e. the tag's detectability underwater, uniqueness of the AID tag's acoustic signature, and ease of deployment and maintenance, newer designs

can be explored. For example, spherical AID tags with circumferentially graded acoustic properties may be used to generate azimuthally dependent acoustic signatures which could provide bearing information to the interrogating SONAR. Other forms and arrangements of underwater reflectors may also be designed, specific to the type of SONAR instrumentation onboard an AUV and mission objective.

# **Appendices**

# APPENDIX A

## ANALYTICAL FORMULATION FOR THE SCATTERED ACOUSTIC FIELD FROM A SPHERICAL SHELL

An analytic solution is derived for the scattering from concentric spherical elastic shells subject to time-harmonic plane wave insonification. The derivation closely follows the presentation given by Schmidt, and expands on the boundary conditions, and construction of the transfer matrix for an 'L' layered spherical system.

### A.1 Conventions used:

The derivation assumes the following:

- Time dependence  $e^{-i\omega t}$
- The spherical shells are numbered such that the innermost layer is layer number 1, and the outermost layer is layer L.
- The solution is obtained in the spherical coordinate system  $(r, \theta, \phi)$ , and the Laplace operator used in Helmholtz equation is suitably selected as

$$\nabla^2(r, \theta) := \frac{1}{r^2} \frac{\partial}{\partial r} r^2 \frac{\partial}{\partial r} + \frac{1}{r^2} \left( \frac{1}{\sin \theta} \frac{\partial}{\partial \theta} \sin \theta \frac{\partial}{\partial \theta} \right) \quad (\text{A.1})$$

Here, we ignore the azimuthal ( $\phi$ ) variation due to the symmetry of the problem.

- The selection of time convention suggests that the spherical functions used to represent incoming and outgoing waves are respectively the spherical Bessel function ( $j_n$ ), and the spherical Hankel function of the first kind ( $h_n^{(1)}$ ).

- The compressional wave number for layer  $l$  is denoted by  $h_l = \omega/c_L$  and the shear wave number by  $k_l = \omega/c_S$ .

## A.2 Preliminaries

In a spherical coordinate system  $(r, \theta, \phi)$  with the azimuthal axis  $\theta = 180^\circ$  passing through the source, the field in an isotropic, elastic layer number  $l$  containing the source at radius  $r_0$  is governed by the Helmholtz equations:

$$\nabla^2 \phi(r, \theta) + h_l^2 \phi(r, \theta) = -\frac{\delta(r - r_0)\delta(\theta)}{2\pi r^2 \sin \theta} \quad (\text{A.2})$$

$$\nabla^2 \psi(r, \theta) + k_l^2 \psi(r, \theta) = 0 \quad (\text{A.3})$$

where  $\phi, \psi$  are the compressional and shear displacement potentials which are decompositions of the total displacement field. The total field can therefore be expressed as a superposition of the *homogenous solutions*  $\tilde{\phi}, \tilde{\psi}$  of (Equation A.2) and the particular solution  $\hat{\phi}$  to the *inhomogenous* form of the compressional equation (Equation A.2) where

$$\phi = \tilde{\phi} + \hat{\phi}$$

$$\psi = \tilde{\psi}$$

Under no external forcing conditions, the homogenous Helmholtz equation can be solved to obtain the frequency response of the shell. The Helmholtz equations are further decomposed using a Legendre transform pair to spatially decouple the radial and polar terms. The analysis and synthesis functions for the transform are defined as



$$\Phi(r, n) = \int_0^\pi \phi(r, \theta) P_n(\cos \theta) \sin \theta d\theta \quad (\text{A.4})$$

$$\phi(r, \theta) = \sum_{n=0}^{\infty} \left( n + \frac{1}{2} \right) \Phi(r, n) P_n(\cos \theta) \quad (\text{A.5})$$

Where  $n$  is the mode order, and  $P_n$  is the 0th order associated Legendre polynomial of degree  $n$ .  $\Phi(r, n)$  is the displacement potential in the transformed domain, dependent on the radius of evaluation, and degree  $n$ .

The homogeneous Helmholtz equations are therefore transformed into equations of the synthesis function as

$$\left( \frac{\partial^2}{\partial r^2} + \frac{2}{r} \frac{\partial}{\partial r} - \frac{1}{r^2} [n(n+1) - h_l^2 r^2] \right) \tilde{\Phi}(r, n) = 0 \quad (\text{A.6})$$

$$\left( \frac{\partial^2}{\partial r^2} + \frac{2}{r} \frac{\partial}{\partial r} - \frac{1}{r^2} [n(n+1) - k_l^2 r^2] \right) \tilde{\Psi}(r, n) = 0 \quad (\text{A.7})$$

and the solution to the displacement potentials in the coupled domain are the spherical Bessel functions, weighted by arbitrary coefficients  $A_l^j(n)$ ,  $A_l^h(n)$ ,  $B_l^j(n)$ ,  $B_l^h(n)$  on the boundary conditions of the problem.

$$\tilde{\phi}(r, \theta) = \sum_{n=0}^{\infty} \left( n + \frac{1}{2} \right) [A_l^j(n) j_n(h_l r) + A_l^h(n) h_n^{(1)}(h_l r)] P_n(\cos \theta) \quad (\text{A.8})$$

$$\tilde{\psi}(r, \theta) = \sum_{n=0}^{\infty} \left( n + \frac{1}{2} \right) [B_l^j(n) j_n(k_l r) + B_l^h(n) h_n^{(1)}(k_l r)] P_n^1(\cos \theta) \quad (\text{A.9})$$

**NOTE:**  $j_n$  and  $h_n^{(1)}$  are selected as two independent solutions to the problem to guarantee non-singularity at the origin, and to satisfy Sommerfeld's radiation condition at  $r \rightarrow \infty$ . In addition to selecting these solutions, we specify  $A_L^j = B_L^j = A_1^h = B_1^h = 0$ .

### A.3 Boundary Conditions

Four boundary conditions are necessary to determine the four arbitrary weights that scale the spherical Bessel functions. These must be specified at every interface separating two spherical shells, and are:

- Radial displacement continuity ( $u_r$ )
- Angular displacement continuity ( $u_\theta$ )
- Normal stress continuity ( $\sigma_{rr}$ )
- Shear stress continuity ( $\sigma_{r\theta}$ )

where there field variables can be expressed in terms of displacement potentials as

$$u_r = \frac{\partial \phi}{\partial r} + \frac{1}{r \sin \theta} \frac{\partial}{\partial \theta} \sin \theta \frac{\partial \psi}{\partial \theta} \quad (\text{A.10})$$

$$u_\theta = \frac{1}{r} \frac{\partial \phi}{\partial \theta} - \frac{1}{r} \frac{\partial}{\partial r} r \frac{\partial \psi}{\partial \theta} \quad (\text{A.11})$$

$$\sigma_{rr} = \lambda \nabla^2 \phi + 2\mu \frac{\partial u_r}{\partial r} \quad (\text{A.12})$$

$$\sigma_{r\theta} = \mu \left[ \frac{1}{r} \frac{\partial u_r}{\partial \theta} + \left( \frac{\partial}{\partial r} - \frac{1}{r} \right) u_\theta \right] \quad (\text{A.13})$$

Before proceeding with the derivation, some relations for Legendre polynomials and spherical Bessel function simplification are presented below:

#### Legendre Polynomial Identities:

$$\begin{aligned} P_{n,\theta}(\cos \theta) &= P_n^1(\cos \theta) \\ \frac{1}{\sin \theta} \frac{d}{d\theta} \left[ \sin \theta \frac{dP_n(\cos \theta)}{d\theta} \right] &= -n(n+1)P_n(\cos \theta) \\ P_n^m(x) &= (-1)^m (1-x^2)^{m/2} \frac{d^m P_n(x)}{dx^m} \end{aligned}$$

### Spherical Bessel function identities:

$$j'_n(kr) = k j'_n(kr)$$

$$r^2 j''_n(kr) + 2r j'_n(kr) + [k^2 r^2 - n(n+1)] j_n(kr) = 0$$

Substituting the expansion terms into the boundary conditions, and using relations for the Legendre polynomials and spherical Bessel functions to simplify,

#### A.3.1 Derivation of $u_r$

From (Equation A.10) we have

$$u_r = \frac{\partial \phi}{\partial r} + \frac{1}{r \sin \theta} \frac{\partial}{\partial \theta} \sin \theta \frac{\partial \psi}{\partial \theta}$$

and upon substitution of the displacement potentials (Equation A.9) and (Equation A.8)

$$u_r = \sum_{n=0}^{\infty} \left( n + \frac{1}{2} \right) \left\{ A_l^j(n) h_l j'_n(h_l r) + A_l^h(n) h_l h_n^{(1)'}(h_l r) - \dots \right. \\ \left. \frac{n(n+1)}{r} [B_l^j(n) j_n(k_l r) + B_l^h(n) h_n^{(1)}(k_l r)] \right\} P_n(\cos \theta) \quad (\text{A.14})$$

#### A.3.2 Derivation of $u_\theta$

From (Equation A.11) we have

$$u_\theta = \frac{1}{r} \frac{\partial \phi}{\partial \theta} - \frac{1}{r} \frac{\partial}{\partial r} r \frac{\partial \psi}{\partial \theta} \quad (\text{A.15})$$

and upon substitution of the displacement potentials (Equation A.9) and (Equation A.8)

$$u_\theta = \sum_{n=0}^{\infty} \left( n + \frac{1}{2} \right) \left\{ A_l^j(n) \frac{j_n(h_l r)}{r} + A_l^h(n) \frac{h_n^{(1)}(h_l r)}{r} - \dots \right. \\ \left. B_l^j(n) \left( \frac{j_n(k_l r)}{r} + k_l j_n'(k_l r) \right) - B_l^h(n) \left( \frac{h_n^{(1)}(k_l r)}{r} + k_l h_n^{(1)'}(k_l r) \right) \right\} P_n^1(\cos \theta) \quad (\text{A.16})$$

### A.3.3 Derivation of $\sigma_{rr}$

From (Equation A.12) we have

$$\sigma_{rr} = \lambda \nabla^2 \phi + 2\mu \frac{\partial u_r}{\partial r} \quad (\text{A.17})$$

Here,

$$\nabla^2 := \underbrace{\frac{1}{r^2} \frac{\partial}{\partial r} r^2 \frac{\partial}{\partial r}}_{(a)} + \underbrace{\frac{1}{r^2} \left( \frac{1}{\sin \theta} \frac{\partial}{\partial \theta} \sin \theta \frac{\partial}{\partial \theta} \right)}_{(b)}$$

Evaluating the Laplacian components (a) and (b) individually:

$$(a) := \frac{1}{r^2} \frac{\partial}{\partial r} r^2 \frac{\partial \phi}{\partial r} = \frac{1}{r^2} \left[ 2r \frac{\partial \phi}{\partial r} + r^2 \frac{\partial^2 \phi}{\partial r^2} \right] = \frac{2}{r} \frac{\partial \phi}{\partial r} + \frac{\partial^2 \phi}{\partial r^2}$$

substituting  $\phi$  provides

$$(a) := \sum_{n=0}^{\infty} \left( n + \frac{1}{2} \right) \left\{ \frac{2}{r} [A_l^j(n) h_l j_n'(h_l r) + A_l^h(n) h_l h_n^{(1)'}(h_l r)] + \dots \right. \\ \left. [A_l^j(n) h_l^2 j_n''(h_l r) + A_l^h(n) h_l^2 h_n^{(1)''}(h_l r)] \right\} P_n(\cos \theta)$$

and similarly

$$(b) := - \sum_{n=0}^{\infty} \left( n + \frac{1}{2} \right) \frac{n(n+1)}{r^2} [A_l^j(n) j_n(h_l r) + A_l^h(n) h_n^{(1)}(h_l r)] P_n(\cos \theta)$$

now collecting (a) and (b) we have

$$\begin{aligned} \lambda \nabla^2 \phi = \lambda \sum_{n=0}^{\infty} \left( n + \frac{1}{2} \right) \left\{ A_l^j(n) \left[ \frac{2h_l}{r} j_n'(h_l r) + h_l^2 j_n''(h_l r) - \frac{n(n+1)}{r^2} j_n(h_l r) \right] + \dots \right. \\ \left. A_l^h(n) \underbrace{\left[ \frac{2h_l}{r} h_n^{(1)'}(h_l r) + h_l^2 h_n^{(1)''}(h_l r) - \frac{n(n+1)}{r^2} h_n^{(1)}(h_l r) \right]}_{(c)} \right\} P_n(\cos \theta) \end{aligned}$$

Notice that the term (c), and the similar coefficient for  $A_l^j(n)$  can be simplified using Bessel's differential equation previously listed i.e. consider

$$\begin{aligned} & \frac{2h_l}{r} h_n^{(1)'}(h_l r) + h_l^2 h_n^{(1)''}(h_l r) - \frac{n(n+1)}{r^2} h_n^{(1)}(h_l r) \\ &= \frac{2h_l r}{r^2} h_n^{(1)'}(h_l r) + \frac{h_l^2 r^2}{r^2} h_n^{(1)''}(h_l r) - \frac{n(n+1)}{r^2} h_n^{(1)}(h_l r) \\ &= \frac{1}{r^2} \left[ 2h_l r h_n^{(1)'}(h_l r) + h_l^2 r^2 h_n^{(1)''}(h_l r) - n(n+1) h_n^{(1)}(h_l r) \right] \\ &= -h_l^2 h_n^{(1)}(h_l r) \end{aligned}$$

Therefore, the entire Laplacian term is finally rewritten as

$$\lambda \nabla^2 \phi = -h_l^2 \lambda \sum_{n=0}^{\infty} \left( n + \frac{1}{2} \right) [A_l^j(n) j_n(h_l r) + A_l^h(n) h_n^{(1)}(h_l r)] P_n(\cos \theta)$$

we now proceed to evaluate the radial derivative of the radial displacement i.e.

$$2\mu \frac{\partial u_r}{\partial r} = 2\mu \frac{\partial}{\partial r} \left[ \sum_{n=0}^{\infty} \left( n + \frac{1}{2} \right) \left\{ A_l^j(n) h_l j_n'(h_l r) + A_l^h(n) h_l h_n^{(1)'}(h_l r) - \dots \right. \right. \\ \left. \left. \frac{n(n+1)}{r} [B_l^j(n) j_n(k_l r) + B_l^h(n) h_n^{(1)}(k_l r)] \right\} P_n(\cos \theta) \right]$$

proceeding carefully with the evaluation, we have

$$2\mu \frac{\partial u_r}{\partial r} = 2\mu \sum_{n=0}^{\infty} \left( n + \frac{1}{2} \right) \left\{ A_l^j(n) h_l^2 j_n''(h_l r) + A_l^h(n) h_l^2 h_n^{(1)''}(h_l r) - \dots \right. \\ \frac{n(n+1)}{r} [B_l^j(n) k_l j_n'(k_l r) + B_l^h(n) k_l h_n^{(1)'}(k_l r)] + \dots \\ \left. \frac{n(n+1)}{r^2} [B_l^j(n) j_n(k_l r) + B_l^h(n) h_n^{(1)}(k_l r)] \right\} P_n(\cos \theta)$$

and finally assembling the normal stress equation

$$\sigma_{rr} = \sum_{n=0}^{\infty} \left( n + \frac{1}{2} \right) \left\{ A_l^j(n) h_l^2 [2\mu j_n''(h_l r) - \lambda j_n(h_l r)] + \dots \right. \\ A_l^h(n) h_l^2 [2\mu h_n^{(1)''}(h_l r) - \lambda h_n^{(1)}(h_l r)] - \dots \\ B_l^j(n) \left[ 2\mu \frac{n(n+1)}{r} \left( k_l j_n'(k_l r) - \frac{j_n(k_l r)}{r} \right) \right] - \dots \\ \left. B_l^h(n) \left[ 2\mu \frac{n(n+1)}{r} \left( k_l h_n^{(1)'}(k_l r) - \frac{h_n^{(1)}(k_l r)}{r} \right) \right] \right\} P_n(\cos \theta) \quad (\text{A.18})$$

#### A.3.4 Derivation of $u_{r\theta}$

From (Equation A.13) we have

$$\sigma_{r\theta} = \mu \left[ \underbrace{\frac{1}{r} \frac{\partial u_r}{\partial \theta}}_{(a)} + \underbrace{\left( \frac{\partial}{\partial r} - \frac{1}{r} \right) u_{\theta}}_{(b)} \right]$$

which is again evaluated in parts (a) and (b), and then finally assembled similar to the computation of the normal stress equation.

$$(a) := \frac{1}{r} \frac{\partial u_r}{\partial \theta} = \frac{1}{r} \sum_{n=0}^{\infty} \left( n + \frac{1}{2} \right) \left\{ A_l^j(n) h_l j_n'(h_l r) + A_l^h(n) h_l h_n^{(1)'}(h_l r) - \dots \right. \\ \left. \frac{n(n+1)}{r} [B_l^j(n) j_n(k_l r) + B_l^h(n) h_n^{(1)}(k_l r)] \right\} P_n^1(\cos \theta)$$

and

$$(b) := \sum_{n=0}^{\infty} \left( n + \frac{1}{2} \right) \left\{ A_l^j(n) \left[ h_l \frac{j_n'(h_l r)}{r} - \frac{2}{r^2} j_n(h_l r) \right] + \dots \right. \\ A_l^h(n) \left[ h_l \frac{h_n^{(1)'}(h_l r)}{r} - \frac{2}{r^2} h_n^{(1)}(h_l r) \right] - \dots \\ B_l^j(n) \left[ k_l^2 j_n''(k_l r) - \frac{2}{r^2} j_n(k_l r) \right] - \dots \\ \left. B_l^h(n) \left[ k_l^2 h_n^{(1)''}(k_l r) - \frac{2}{r^2} h_n^{(1)}(k_l r) \right] \right\} P_n^1(\cos \theta)$$

and finally adding (a) and (b) provides

$$\sigma_{r\theta} = \mu \sum_{n=0}^{\infty} \left( n + \frac{1}{2} \right) \left\{ A_l^j(n) \left[ 2 \frac{h_l}{r} j_n'(h_l r) - \frac{2}{r^2} j_n(h_l r) \right] + \dots \right. \\ A_l^h(n) \left[ 2 \frac{h_l}{r} h_n^{(1)'}(h_l r) - \frac{2}{r^2} h_n^{(1)}(h_l r) \right] - \dots \\ B_l^j(n) \left[ k_l^2 j_n''(k_l r) - \frac{2}{r^2} j_n(k_l r) + \frac{n(n+1)}{r^2} j_n(k_l r) \right] - \dots \\ \left. B_l^h(n) \left[ k_l^2 h_n^{(1)''}(k_l r) - \frac{2}{r^2} h_n^{(1)}(k_l r) + \frac{n(n+1)}{r^2} h_n^{(1)}(k_l r) \right] \right\} P_n^1(\cos \theta) \quad (\text{A.19})$$

The expressions for displacement and stress continuity at each layer interface can now be written in a form similar to the global matrix method (see Equation 2.21) and inverted

to solve for the amplitudes  $A_l^h(n)$ ,  $A_l^j(n)$ ,  $B_l^h(n)$ , and  $B_l^j(n)$  for each layer in the layered shell structure.



**APPENDIX B**  
**TABLE OF MATERIAL PROPERTIES**

Table B.1: Acoustic properties of common fluids, plastics, and metals

Material Name <sup>c</sup>	Longitudinal Velocity ( $c_L$ ) (m/s)	Density ( $\rho$ ) (kg/m <sup>3</sup> )	Characteristic Impedance ( $z = \rho c_L$ ) (Mrayl)	Attenuation (nepers/ $\lambda$ )
Water	1480	1000	1.48	$3.6995 \times 10^{-4}$ (6 MHz) <sup>a</sup>
glycerine	1920	1260	2.42	$3.7034 \times 10^{-6}$ (500 kHz) <sup>a</sup>
Air	331	1.29	$0.426 \times 10^{-3}$	$10.54 \times 10^{-2}$ (6MHz)
Acrylic <sup>b</sup>	2766	1190	3.27	N/A
PVC <sup>b</sup>	2227	1380	3.07	$5.16 \times 10^{-2}$
Polycarbonate <sup>b</sup>	2250	1200	2.76	$7.68 \times 10^{-2}$
PETG <sup>b</sup>	2210	1270	2.81	$11.23 \times 10^{-2}$
HDPE <sup>b</sup>	2512	941	2.36	$12.95 \times 10^{-2}$
Nylon 6/6	2600	1120	2.91	$8.43 \times 10^{-2}$
Aluminium	6380	2730	17.42	N/A
Steel (304 Stainless)	5675	7570	42.95	$6.24 \times 10^{-2}$
				N/A

<sup>a</sup>from [52, 51]

<sup>b</sup>Experimentally determined acoustic velocity and attenuation at 6MHz

<sup>c</sup>Properties of unmarked materials obtained from [84]

## REFERENCES

- [1] J. C. Kinsey, R. M. Eustice, and L. L. Whitcomb, "A survey of underwater vehicle navigation : Recent advances and new challenges," 2006.
- [2] W. Senke, "Applications of autonomous underwater vehicles (AUVs) in ocean mining exploration," in *2013 OCEANS - San Diego*, Sep. 2013, pp. 1–3.
- [3] R. B. Wynn, V. A. I. Huvenne, T. P. Le Bas, B. J. Murton, D. P. Connelly, B. J. Bett, H. A. Ruhl, K. J. Morris, J. Peakall, D. R. Parsons, E. J. Sumner, S. E. Darby, R. M. Dorrell, and J. E. Hunt, "Autonomous Underwater Vehicles (AUVs): Their past, present and future contributions to the advancement of marine geoscience," *Marine Geology*, 50th Anniversary Special Issue, vol. 352, pp. 451–468, Jun. 2014.
- [4] R. Stokey, T. Austin, B. Allen, N. Forrester, E. Gifford, R. Goldsborough, G. Packard, M. Purcell, and C. von Alt, "Very shallow water mine countermeasures using the REMUS AUV: A practical approach yielding accurate results," in *MTS/IEEE Oceans 2001. An Ocean Odyssey. Conference Proceedings (IEEE Cat. No.01CH37295)*, vol. 1, Nov. 2001, 149–156 vol.1.
- [5] L. Paull, S. Saeedi, M. Seto, and H. Li, "AUV Navigation and Localization: A Review," *IEEE Journal of Oceanic Engineering*, vol. 39, no. 1, pp. 131–149, Jan. 2014.
- [6] B. Allen, T. Austin, N. Forrester, R. Goldsborough, A. Kukulya, G. Packard, M. Purcell, and R. Stokey, "Autonomous docking demonstrations with enhanced remus technology," in *OCEANS 2006*, IEEE, 2006, pp. 1–6.
- [7] J. J. and M. D., *AUV-based structural integrity management for deepwater fields - driving down costs; improving safety and performance*.
- [8] NOAA, Office of Ocean Exploration and Research, *What is an ROV?*
- [9] O. J. Woodman, "An introduction to inertial navigation," University of Cambridge, Computer Laboratory, Tech. Rep., 2007.
- [10] A. Asada, M. Mochizuki, T. Ura, H. Zheng, T. Tanaka, O. Colombo, T. Ensign, and K. Nagahashi, "Evaluation result of new seafloor mirror transponder and AUV observation system in seafloor geodetic observation," in *OCEANS 2007 - Europe*, Jun. 2007, pp. 1–4.
- [11] M. Mochizuki, A. Asada, T. Ura, Z. Yoshida, K. Asakawa, T. Yokobiki, R. Iwase, T. Goto, M. Fujita, M. Sato, O. L. Colombo, T. Tanaka, H. Zheng, and K. Nagahashi, "Development of seafloor geodetic observation system based on AUV and submarine cable technologies," in *OCEANS'10 IEEE SYDNEY*, May 2010, pp. 1–4.

- [12] J. Čejka, F. Bruno, D. Skarlatos, and F. Liarokapis, “Detecting Square Markers in Underwater Environments,” *Remote Sensing*, vol. 11, no. 4, p. 459, Jan. 2019.
- [13] Y. Wang, Y. Ji, D. Liu, Y. Tamura, H. Tsuchiya, A. Yamashita, and H. Asama, “Ac-marker: Acoustic camera-based fiducial marker system in underwater environment,” *IEEE Robotics and Automation Letters*, vol. 5, no. 4, pp. 5018–5025, 2020.
- [14] P. H. Milne, *Underwater Acoustic Positioning Systems*, illustrated edition edition. Houston: Gulf Pub Co, Dec. 1983, ISBN: 978-0-87201-012-3.
- [15] I. Masmitja, S. Gomariz, J. Del Rio, B. Kieft, and T. O’Reilly, “Range-only underwater target localization: Path characterization,” in *OCEANS 2016 MTS/IEEE Monterey*, IEEE, 2016, pp. 1–7.
- [16] J. González-García, A. Gómez-Espinosa, E. Cuan-Urquizo, L. G. García-Valdovinos, T. Salgado-Jiménez, and J. A. E. Cabello, “Autonomous underwater vehicles: Localization, navigation, and communication for collaborative missions,” *Applied Sciences*, vol. 10, no. 4, p. 1256, 2020.
- [17] J. P. Fula, B. M. Ferreira, and A. J. Oliveira, “Auv self-localization in structured environments using a scanning sonar and an extended kalman filter,” in *OCEANS 2018 MTS/IEEE Charleston*, IEEE, 2018, pp. 1–6.
- [18] V. P. Plessky, “Review on SAW RFID tags,” in *2009 IEEE International Frequency Control Symposium Joint with the 22nd European Frequency and Time forum*, Apr. 2009, pp. 14–23.
- [19] R. White and F. Voltmer, “Direct piezoelectric coupling to surface elastic waves,” *Applied physics letters*, vol. 7, no. 12, pp. 314–316, 1965.
- [20] V. Plessky and M. Lamothe, “Ultra-wide-band SAW RFID/sensors,” in *2014 European Frequency and Time Forum (EFTF)*, Jun. 2014, pp. 16–23.
- [21] D. R. Gallagher, M. W. Gallagher, N. Saldanha, J. M. Pavlina, and D. C. Malocha, “Spread spectrum orthogonal frequency coded SAW Tags and sensors using harmonic operation,” in *2009 IEEE MTT-S International Microwave Symposium Digest*, ISSN: 0149-645X, Jun. 2009, pp. 105–108.
- [22] R. Gold, “Optimal binary sequences for spread spectrum multiplexing (Corresp.),” *IEEE Transactions on Information Theory*, vol. 13, no. 4, pp. 619–621, Oct. 1967.
- [23] D. Malocha, D. Puccio, and D. Gallagher, “Orthogonal frequency coding for SAW device applications,” in *IEEE Ultrasonics Symposium, 2004*, ISSN: 1051-0117, vol. 2, Aug. 2004, 1082–1085 Vol.2.

- [24] T. M. Grothues, A. E. Newhall, J. F. Lynch, K. S. Vogel, and G. G. Gawarkiewicz, "High-frequency side-scan sonar fish reconnaissance by autonomous underwater vehicles," *Canadian Journal of Fisheries and Aquatic Sciences*, vol. 74, no. 2, pp. 240–255, Jul. 2016.
- [25] P. M. Woodward, *Probability and Information Theory, with Applications to Radar: International Series of Monographs on Electronics and Instrumentation*. Elsevier, 2014, vol. 3.
- [26] J. Sattar, E. Bourque, P. Giguere, and G. Dudek, "Fourier tags: Smoothly degradable fiducial markers for use in human-robot interaction," in *Fourth Canadian Conference on Computer and Robot Vision, 2007. CRV '07*, May 2007, pp. 165–174.
- [27] US Department of Commerce, National Oceanic and Atmospheric Administration, *How far does light travel in the ocean?*
- [28] M. F. Fallon, J. Folkesson, H. McClelland, and J. J. Leonard, "Relocating Underwater Features Autonomously Using Sonar-Based SLAM," *IEEE Journal of Oceanic Engineering*, vol. 38, no. 3, pp. 500–513, Jul. 2013.
- [29] C. I. Malme, "Development of a high target strength passive acoustic reflector for low-frequency sonar applications," *IEEE Journal of Oceanic Engineering*, vol. 19, no. 3, pp. 438–448, Jul. 1994.
- [30] D. L. Folds and C. D. Loggins, "Target strength of liquid-filled spheres," *The Journal of the Acoustical Society of America*, vol. 73, no. 4, pp. 1147–1151, Apr. 1983.
- [31] A. Islas-Cital, P. Atkins, S. Gardner, and C. Tiltman, "Performance of an enhanced passive sonar reflector SonarBell: A practical technology for underwater positioning," *Underwater Technology*, vol. 31, no. 3, pp. 113–122, Jul. 2013.
- [32] J. D. Smith and D. P. Williams, "A focused multi-layered spherical shell with guided wave enhancements," *The Journal of the Acoustical Society of America*, vol. 117, no. 4, pp. 2456–2456, Apr. 2005, Publisher: Acoustical Society of America.
- [33] P. Srivastava, B. Nichols, and K. G. Sabra, "Passive underwater acoustic markers using Bragg backscattering," *The Journal of the Acoustical Society of America*, vol. 142, no. 6, EL573–EL578, Dec. 2017.
- [34] *Springer handbook of ocean engineering*, 1. edition. New York, NY: Springer Berlin Heidelberg, 2016, ISBN: 978-3-319-16648-3.
- [35] P. Lee, B. Jeon, S. Kim, H. Choi, C. Lee, T. Aoki, and T. Hyakudome, "An integrated navigation system for autonomous underwater vehicles with two range sonars, iner-

- tial sensors and Doppler velocity log,” in *Oceans '04 MTS/IEEE Techno-Ocean '04 (IEEE Cat. No.04CH37600)*, vol. 3, Nov. 2004, 1586–1593 Vol.3.
- [36] Z. Yan, S. Peng, J. Zhou, J. Xu, and H. Jia, “Research on an improved dead reckoning for AUV navigation,” in *2010 Chinese Control and Decision Conference*, ISSN: 1948-9447, May 2010, pp. 1793–1797.
  - [37] M. J. S. Lowe, “Matrix techniques for modeling ultrasonic waves in multilayered media,” *IEEE Transactions on Ultrasonics, Ferroelectrics, and Frequency Control*, vol. 42, no. 4, pp. 525–542, Jul. 1995.
  - [38] H. Schmidt and G. Tango, “Efficient global matrix approach to the computation of synthetic seismograms,” *Geophysical Journal of the Royal Astronomical Society*, vol. 84, no. 2, pp. 331–359, Feb. 1986.
  - [39] L. Knopoff, “A matrix method for elastic wave problems,” *Bulletin of the Seismological Society of America*, vol. 54, no. 1, pp. 431–438, Feb. 1964.
  - [40] L. M. Brekhovskikh, *Waves in Layered Media*. Academic Press, Dec. 2012, ISBN: 978-0-12-405405-9.
  - [41] J. Achenbach, *Wave propagation in elastic solids*. Elsevier, 2012.
  - [42] T. Pialucha and P. Cawley, “The reflection of ultrasound from interface layers in adhesive joints,” in *Review of Progress in Quantitative Nondestructive Evaluation*, Springer, 1991, pp. 1303–1309.
  - [43] N. A. Haskell, “The dispersion of surface waves on multilayered media,” *Bulletin of the Seismological Society of America*, vol. 43, no. 1, pp. 17–34, Jan. 1953.
  - [44] W. T. Thomson, “Transmission of elastic waves through a stratified solid medium,” *Journal of applied Physics*, vol. 21, no. 2, pp. 89–93, 1950.
  - [45] A. Satish, B. Nichols, D. Trivett, and K. G. Sabra, “Passive underwater acoustic tags using layered media,” *The Journal of the Acoustical Society of America*, vol. 145, no. 1, EL84–EL89, Jan. 2019, Publisher: Acoustical Society of America.
  - [46] T. L. Szabo and J. Wu, “A model for longitudinal and shear wave propagation in viscoelastic media,” *The Journal of the Acoustical Society of America*, vol. 107, no. 5, pp. 2437–2446, Apr. 2000, Publisher: Acoustical Society of America.
  - [47] B. E. Treeby, J. Jaros, D. Rohrbach, and B. T. Cox, “Modelling elastic wave propagation using the k-Wave MATLAB Toolbox,” in *2014 IEEE International Ultrasonics Symposium*, Sep. 2014, pp. 146–149.

- [48] T. L. Szabo, “Time domain wave equations for lossy media obeying a frequency power law,” *The Journal of the Acoustical Society of America*, vol. 96, no. 1, pp. 491–500, Jul. 1994, Publisher: Acoustical Society of America.
- [49] L. E. Kinsler, A. R. Frey, A. B. Coppens, and J. V. Sanders, *Fundamentals of Acoustics*, 3 edition. New York: Wiley, Jan. 1982, ISBN: 978-0-471-02933-5.
- [50] Analogic Corporation, *Ultrasonix L14-5/38 User Manual*.
- [51] M. A. Ainslie and J. G. McColm, “A simplified formula for viscous and chemical absorption in sea water,” *The Journal of the Acoustical Society of America*, vol. 103, no. 3, pp. 1671–1672, Mar. 1998, Publisher: Acoustical Society of America.
- [52] National Physical Laboratory, UK, *Absorption of sound in seawater*.
- [53] Olympus IMS, *Ultrasonic Couplants*.
- [54] A. Satish, D. Trivett, and K. G. Sabra, “Omnidirectional passive acoustic identification tags for underwater navigation,” *The Journal of the Acoustical Society of America*, vol. 147, no. 6, EL517–EL522, Jun. 2020, Publisher: Acoustical Society of America.
- [55] S. D. Anderson, K. G. Sabra, M. E. Zakharia, and J.-P. Sessarego, “Time-frequency analysis of the bistatic acoustic scattering from a spherical elastic shell,” *The Journal of the Acoustical Society of America*, vol. 131, no. 1, pp. 164–173, Jan. 2012, Publisher: Acoustical Society of America.
- [56] M. Zakharia and J. Sessarego, “Sonar target classification using a coherent echo processing,” in *ICASSP ’82. IEEE International Conference on Acoustics, Speech, and Signal Processing*, vol. 7, May 1982, pp. 331–334.
- [57] M. A. Adegboye, W.-K. Fung, and A. Karnik, “Recent Advances in Pipeline Monitoring and Oil Leakage Detection Technologies: Principles and Approaches,” *Sensors (Basel, Switzerland)*, vol. 19, no. 11, Jun. 2019.
- [58] R. R. Goodman and R. Stern, “Reflection and Transmission of Sound by Elastic Spherical Shells,” *The Journal of the Acoustical Society of America*, vol. 34, no. 3, pp. 338–344, Mar. 1962, Publisher: Acoustical Society of America.
- [59] W. F. Fender, “Scattering from an elastic spherical shell,” NAVAL UNDERSEA CENTER SAN DIEGO CA, Tech. Rep., 1972.
- [60] H. Schmidt, “Numerically stable global matrix approach to radiation and scattering from spherically stratified shells,” *The Journal of the Acoustical Society of America*, vol. 94, no. 4, pp. 2420–2430, Oct. 1993.

- [61] G. Kaduchak and C. Loeffler, "Relationship between material parameters and target strength of fluid-filled spherical shells in water: Calculations and observations," *IEEE Journal of Oceanic Engineering*, vol. 23, no. 1, pp. 26–30, Jan. 1998.
- [62] G. C. Gaunaurd and M. F. Werby, "Lamb and creeping waves around submerged spherical shells resonantly excited by sound scattering," *The Journal of the Acoustical Society of America*, vol. 82, no. 6, pp. 2021–2033, Dec. 1987, Publisher: Acoustical Society of America.
- [63] L. G. Zhang, N. H. Sun, and P. L. Marston, "Midfrequency enhancement of the backscattering of tone bursts by thin spherical shells," *The Journal of the Acoustical Society of America*, vol. 91, no. 4, pp. 1862–1874, Apr. 1992.
- [64] P. L. Marston and N. H. Sun, "Resonance and interference scattering near the coincidence frequency of a thin spherical shell: An approximate ray synthesis," *The Journal of the Acoustical Society of America*, vol. 92, no. 6, pp. 3315–3319, Dec. 1992, Publisher: Acoustical Society of America.
- [65] G. S. Sammelmann, D. H. Trivett, and R. H. Hackman, "The acoustic scattering by a submerged, spherical shell. I: The bifurcation of the dispersion curve for the spherical antisymmetric Lamb wave," *The Journal of the Acoustical Society of America*, vol. 85, no. 1, pp. 114–124, Jan. 1989, Publisher: Acoustical Society of America.
- [66] P. M. Morse and K. U. Ingard, *Theoretical Acoustics*. Princeton, N.J: Princeton University Press, Jan. 1987, ISBN: 978-0-691-02401-1.
- [67] F. Jensen, "On the number of modes in spherical wave expansions," p. 6,
- [68] L. Bjørnø, "Chapter 5 - Scattering of Sound," in *Applied Underwater Acoustics*, T. H. Neighbors and D. Bradley, Eds., Elsevier, Jan. 2017, pp. 297–362, ISBN: 978-0-12-811240-3.
- [69] B. E. Treeby and B. T. Cox, "K-Wave: MATLAB toolbox for the simulation and reconstruction of photoacoustic wave fields," *Journal of Biomedical Optics*, vol. 15, no. 2, p. 021 314, Apr. 2010.
- [70] B. E. Treeby, J. Jaros, A. P. Rendell, and B. Cox, "Modeling nonlinear ultrasound propagation in heterogeneous media with power law absorption using ak-space pseudospectral method," *The Journal of the Acoustical Society of America*, vol. 131, no. 6, pp. 4324–4336, 2012.
- [71] A. Taflove and S. C. Hagness, *Computational Electrodynamics: The Finite-Difference Time-Domain Method, Third Edition*, 3rd Edition. Boston: Artech House, May 2005, ISBN: 978-1-58053-832-9.



- [72] US Department of Commerce, National Oceanic and Atmospheric Administration, *Invention studio, georgia institute of technology*.
- [73] H. L. Van Trees, *Detection, estimation, and modulation theory, part I: detection, estimation, and linear modulation theory*. John Wiley & Sons, 2004.
- [74] E. Larose, A. Derode, M. Campillo, and M. Fink, “Imaging from one-bit correlations of wideband diffuse wave fields,” *Journal of Applied Physics*, vol. 95, no. 12, pp. 8393–8399, Jun. 2004, Publisher: American Institute of Physics.
- [75] A. Duroux, K. G. Sabra, J. Ayers, and M. Ruzzene, “Extracting guided waves from cross-correlations of elastic diffuse fields: Applications to remote structural health monitoring,” *The Journal of the Acoustical Society of America*, vol. 127, no. 1, pp. 204–215, Jan. 2010, Publisher: Acoustical Society of America.
- [76] A. Derode, A. Tourin, and M. Fink, “Ultrasonic pulse compression with one-bit time reversal through multiple scattering,” *Journal of Applied Physics*, vol. 85, no. 9, pp. 6343–6352, Apr. 1999, Publisher: American Institute of Physics.
- [77] M. Fink, “Time-reversal acoustics in complex environments,” *geophysics*, vol. 71, no. 4, SI151–SI164, 2006.
- [78] H.-C. Song, “An overview of underwater time-reversal communication,” *IEEE Journal of Oceanic Engineering*, vol. 41, no. 3, pp. 644–655, 2015.
- [79] F. B. Jensen, W. A. Kuperman, M. B. Porter, and H. Schmidt, *Computational ocean acoustics*. Springer Science & Business Media, 2011.
- [80] Tritech, *StarFish 452F Datasheet*.
- [81] M. Ainslie, *Principles of Sonar Performance Modelling*. Berlin, Heidelberg: Springer Berlin Heidelberg, 2010, ISBN: 978-3-540-87661-8 978-3-540-87662-5.
- [82] P. Swerling, “Probability of detection for fluctuating targets,” *IRE Transactions on Information Theory*, vol. 6, no. 2, pp. 269–308, 1960.
- [83] *Acoustic Water Tank, The Georgia Institute of Technology*.
- [84] A. R. Selfridge, “Approximate material properties in isotropic materials,” *IEEE Transactions on Sonics and Ultrasonics*, vol. 32, no. 3, pp. 381–394, 1985.